Loma Linda University Electronic Theses, Dissertations & Projects

12-2016

Cyclically-Forced Hyperpycnites of the Ancient Colorado River Proximal Prodelta

Sandra R. Waresak

Recommended Citation

LOMA LINDA UNIVERSITY
School of Medicine
in conjunction with the
Faculty of Graduate Studies

———————————————

Cyclically-Forced Hyperpycnites of the Ancient Colorado River Proximal Prodelta

by

Sandra R. Waresak

———————————————

A Thesis submitted in partial satisfaction of
the requirements for the degree
Master of Science in Geology

———————————————

December 2016

Each person whose signature appears below certifies that this thesis in his/her opinion is adequate, in scope and quality, as a thesis for the degree Master of Science.

_____, Chairperson
Ronald Nalin, Adjunct Assistant Professor of Geology

_____
Kevin Nick, Associate Professor of Geology

_____
Suzanne Phillips, Assistant Professor of Biology

ACKNOWLEDGEMENTS

CONTENT

FIGURES

APPENDIX FIGURES

TABLES

ABBREVIATIONS

~	Approximately
º	Degrees
%	Percent
AR(1)	Autoregressive process (first order)
Cg	Coarse-grained
cm	Centimeters
F	Figure
FC	Fish Creek Wash
FCV	Fish Creek-Vallecito
FFT	Fast Fourier Transform
Fg	Fine-grained
Fm	Formation
fs	Fine sand
g	grams
INEGI	Instituto Nacional de Estadística Geografíca e Informática
IPA	Isopropyl alcohol
km	Kilometers
k.y.	Thousand years
L	Liter
m	Meters
Ma	Million years ago
mg	Medium-grained

MHM	Mud Hills Member
mm	Millimeter
ms	Medium sand
NAM	North American monsoon
NW	Northwest
P	P-value
PC	Principal component
SE	Southeast
SW	Southwest
μ	Microns
μm	Micrometers
USA	United States of America
vfg	Very fine-grained
vfs	Very fine sand
wt.	Weight
XRD	X-ray diffraction

ABSTRACT OF THE THESIS

Cyclically-Forced Hyperpycnites of the Ancient Colorado River Proximal Prodelta

by

Sandra R. Waresak

Master of Science, Graduate Program in Geology
Loma Linda University, December 2016
Dr. Ronald Nalin, Chairperson

Prodeltaic deposits record a distal, minimally reworked archive of dominant

processes active at the fluvial-marine interface. The Fish Creek-Vallecito Basin (CA,

US) preserves an ~3 km-thick, lower Pliocene, progradational deltaic succession formed

when the ancestral Colorado River infiltrated the early Gulf of California. The

interpreted prodeltaic unit in this succession (Mud Hills Member of the Deguynos

Formation) contains an ~40 m-thick interval of rhythmic bedding with consistently

alternating silt- to fine sand-dominated and clay-dominated beds forming couplets with

an average thickness of 12 cm. Sedimentological analysis of the rhythmites reveals the

couplets are laterally persistent with gradational to sharp, flat contacts, parallel, wavy,

and ripple cross-lamination, and localized internal scours. Notably, grain size analysis

performed with laser diffraction techniques shows a consistent pattern of inverse grading

transitioning to normal grading. The cumulative sedimentological evidence indicates that

deposition of the rhythmites was accomplished via hyperpycnal flows, each couplet likely

representing one event in a setting characterized by high overall depositional rates. Time

series analysis performed on bed thickness of 265 measured couplets obtained a

prominent spectral peak above the 99% confidence level corresponding to a periodicity of

~18 couplets. Interpretations are tentative, but potential controls on cyclicity include

seasonal climatic events or the lunar nodal cycle. Finally, a review of previous studies of the progression of the lower Colorado River to the Gulf of California, via the fill and overspill of a series of lakes, places deposition of the Mud Hills Member hyperpycnites immediately after the fourth, and last, lake drains, commencing unimpeded Colorado River flow and formation of a fluvial-dominated proximal prodelta.

This study contributes to the recently established record of fine-grained hyperpycnites in the ancient rock record and to previous work substantiating the theory that ancient prodeltaic mudrocks may have been primarily deposited rapidly via hyperpycnal flow rather than slowly via suspension settling. Also, this study complements previous work on the initiation and progradation of the Pliocene Colorado River delta and adds to the growing evidence for the lake-spillover model of the advancement of the lower Colorado River to the Gulf of California.

CHAPTER ONE

INTRODUCTION

Problem and Goals

Sedimentary successions consisting of coarse and fine beds in close alternation have long attracted the interest of sedimentologists by posing intriguing questions concerning mode of deposition and controls on the underlying rhythmic bedding. Pursuit of the answers has led to notable advancements, including the "turbidity current" paradigm revolution and the development of cyclostratigraphy (e.g., Kuenen and Migliorini (1950) and Einsele et al. (1991)). Environments of deposition conducive to the accumulation of rhythmically bedded successions typically support flows with fluctuating energy levels or intermittent sediment gravity flows. Prodeltaic environments are a classic setting where rhythmic deposits occur and are important geologically since they record the interaction at the continental (fluvial) and marine interface.

The Fish Creek-Vallecito (FCV) basin (CA, US) infill contains an ~255 m-thick succession of rhythmically bedded muddy siltstones and sandstones, corresponding to the upper Mud Hills Member (MHM) of the Deguynos Formation and interpreted as a prodeltaic unit formed when the ancient (Pliocene) Colorado River infiltrated a marine rift basin (Dorsey et al., 2011; Winker, 1987). In his exhaustive study of the FCV basin, Winker (1987) observed, "Mode of deposition of the rhythmites and controls on cyclicity are problematic". Winker (1987) notes that the "striking lateral continuity" of the rhythmites, though "unusual" for traction-dominated deposits, is common to turbidites and suggests deposition via sediment gravity flows. Additionally, Winker (1987) suggests that the rhythmicity is episodic, not periodic, though Winker and Kidwell (1996)

advocate seasonal or annual controls on cyclicity, noting that "other interpretations are certainly possible". By performing a detailed sedimentological analysis of the MHM rhythmites and investigating periodicities in bed thickness, this study aimed to: 1. reconstruct the mode of deposition of this enigmatic prodeltaic succession, and, 2. explore the possibility that the rhythmites were deposited under the influence of periodic controls.

Prodeltas

Prodeltaic deposits represent a valuable archive for the characterization of deltaic depositional systems, offering a distal, minimally reworked record of dominant processes active at the fluvial-marine interface (Bhattacharya and MacEachern, 2009; Wilson and Schieber, 2014). Prodeltas are the distal portion of deltaic environments, typically located along gently sloping basin margins in depths generally beyond the continual influence of waves and tides (Jackson and Bates, 1997). Although interspersed coarser beds are not uncommon, prodeltaic facies are usually dominated by fine-grained deposits traditionally interpreted as having settled out of suspension. High sedimentation rates typify river-influenced prodeltas and may result in occasional soft-sediment deformation, the formation and preservation of flow structures, and the inhibition of bioturbation (Bhattacharya, 2006; MacEachern and Bann, 2008). Intense heterolithic lamination with asymmetrical or (less commonly) combined-flow ripples and moderate bioturbation is more indicative of a tide-influenced prodeltaic environment (Bhattacharya, 2006; Bohacs et al., 2014; MacEachern and Bann, 2008). Wave-influenced prodeltaic systems may display oscillatory structures such as hummocky cross-lamination or wave ripples, but,

due to lower sedimentation rates, increased bioturbation may obliterate primary structures (MacEachern and Bann, 2008).

Hyperpycnal Flow

Hyperpycnal flows, first documented by Forel (1885, 1892) in Lake Geneva (as cited by Mulder et al., 2003), are sustained, quasi-steady, sediment gravity flows that emanate from river mouths typically during flood events (Mulder and Alexander, 2001). In their classic work, Mulder and Syvitski (1995) described marine hyperpycnal flows as seafloor-hugging plumes that form near river mouths when the combined density of the fresh water plus its suspended sediment load exceeds the density of the sea water. Saline water is denser than fresh water, but when the sediment load of a river is large enough, the combined flow plunges to the seafloor and travels along the bottom, even on low gradients and sometimes for hundreds of kilometers (Mulder and Syvitski, 1995; Nakajima, 2006). As the current travels, sediment is deposited and the density of the flow wanes resulting in a 'lofting' upwards of the flow and the finest sediments, which subsequently settle (Sparks, 1993; Zavala, 2006). The resulting deposit was first termed a hyperpycnite by Mulder et al. (2002).

Hyperpycnal density currents are important agents of sediment transportation to the ocean basins and are known to occur in prodeltaic settings (Bhattacharya and MacEachern, 2009; Mulder et al., 2003; Nakajima, 2006; Plint, 2014; Wilson and Schieber, 2014). But, because of their fine-grained character, sparse sedimentary structures, and deep weathering, muddy hyperpycnites are difficult to distinguish in the field and consequently are poorly documented in ancient strata (Bhattacharya and

MacEachern, 2009; Soyinka and Slatt, 2008; Wilson and Schieber, 2014; Zavala et al., 2011). Though a hyperpycnite facies model is still evolving, characteristics include mudstone-siltstone couplets with gradational to sharp contacts, internal scours, planar-parallel to low-angle cross-lamination, wavy lamination, current ripples, the presence of mica and plant debris, and reduced intensity and diversity of bioturbation (Mulder et al., 2003; Plink-Björklund and Steel, 2004; Soyinka and Slatt, 2008; Wilson and Schieber, 2015; Zavala et al., 2011). Notably, hyperpycnites have a distinct grain-size variation: coarsening-up beds transition (sometimes abruptly) to fining-up beds (Bhattacharya and MacEachern, 2009; Mulder and Alexander, 2001; Plink-Björklund and Steel, 2004; Soyinka and Slatt, 2008; Zavala et al., 2011).

Cyclical Forcing

Sedimentary deposition in ancient deltaic environments can be cyclically forced by both tidal and climatic controls (Archer and Kvale, 1989; Grippo et al., 2004; Hinnov, 2013; Larkins, 2009; Meyers et al., 2001). Gravitational forces of the moon and sun combined with the earth's rotation produce oceanic tides on a diurnal or semi-diurnal basis. The magnitude of these tides can be modulated by a variety of forces, such as the relative alignment of the earth, moon, and sun producing the semi-monthly, neap-spring cycle and the lunar-nodal cycle (18.6 yrs.). Climatic variations are primarily governed by changes in insolation, which in turn is thought to be influenced by a host of low- to high-frequency controls including various solar cycles (11-1000 yrs.) and astronomical controls such as the precession of Earth's rotation axis (~21 k.y.), Earth's axial tilt

(obliquity; ~41 k.y.), and Earth's orbital eccentricity (~405 k.y.) (de Boer and Alexandre, 2012; Hinnov, 2013; Park and Chang, 2013).

Bed thickness and grain size have been shown to vary periodically in rhythmites, reflecting climatic and/or tidal patterns (Burgess, 2016; Larkins, 2009; Meyers et al., 2001; Miller and Eriksson, 1997). Since the MHM rhythmites visually display a cyclic pattern and excellent time control at the scale of the Member has previously been established (Dorsey et al., 2011; Winker, 1987), this unit was an ideal candidate to test for nonrandom variations in bed thickness and grain size. Identification of cyclical signals (preserved in grain-size and/or bed thickness variations) in the strata via time series analysis and comparison with previously established cycles (tidal, seasonal, etc.) may clarify the correlation between depositional characteristics and cyclical influences.

Significance

Recent studies of modern fluvio-deltaic systems reveal that sediment transport by hyperpycnal flow is prevalent, questioning the historical assumption that marine mudstones are chiefly deposited from suspension in quiet waters (Bhattacharya and MacEachern, 2009; Schieber et al., 2007). Recognizing hyperpycnites in ancient strata is vital to the study of basin development, the paleoenvironmental records preserved therein, and even the characterization of hydrocarbon reservoirs (Bhattacharya and MacEachern, 2009; Bonnecaze and Lakshminarasimhan, 2005; Diaz et al., 2011; Mulder et al., 2003; Nakajima, 2006; Soyinka and Slatt, 2008). This study may lend support to the growing body of literature substantiating the theory that ancient prodeltaic mudrocks may have been primarily deposited rapidly via hyperpycnal flow rather than slowly via

suspension settling. Additionally, this study may contribute to the methods of discerning hyperpycnites in ancient rocks. A refined hyperpycnite facies model could be applied to other ancient prodeltaic successions providing new insight on the timing of and sedimentary controls on infill.

Identification of quasi-periodic variation in the MHM rhythmites may have important implications regarding the paleoenvironmental mechanisms controlling deposition that could be applied to other ancient prodeltaic systems (de Boer and Alexandre, 2012; Larkins, 2009; Mulder et al., 2001). Since the frequency of hyperpycnal flows is directly related to the frequency of riverine floods, detection of cycles in the MHM unit could contribute to our knowledge of early Pliocene climatic events within the catchment region (southwestern US) (Mulder et al., 2001). Also, refining the connection between allocyclic forces and bed thickness may contribute to our understanding of how such forces are transmitted into depositional environments (de Boer and Alexandre, 2012; Grippo et al., 2004; Larkins, 2009). The MHM rhythmites may have preserved a record of the effects of climatic variations over the Colorado River catchment on the integration of the early, lower Colorado River with the proto-Gulf of California.

CHAPTER TWO

GEOLOGIC BACKGROUND

Regional Setting

The Salton Trough is a large continental depression in southern California that straddles the boundary zone between the North American and Pacific tectonic plates (F 1A, 1B). It is thought to have formed during the Miocene as a result of transtensional forces associated with the interplate boundary and mostly accommodated along the southern San Andreas Fault system to the east and a detachment fault system to the west (Axen and Fletcher, 1998; Dorsey et al., 2011; Winker, 1987). The trough is considered to be the northwestward terrestrial extension of the Gulf of California, from which it is now separated primarily by the deposits of the Pliocene-Pleistocene fluvio-deltaic plain of the ancestral Colorado River (Winker, 1987). Today, the most depressed part of the Salton Trough is occupied by a saline lake, the Salton Sea.

Basin analysis reconstructions suggest that during the Miocene, major tectonic adjustments associated with the West Salton detachment and the southern San Andreas fault systems initiated clockwise rotation of the Baja California crustal block away from North America (Axen and Fletcher, 1998; Dorsey, 2006). With continued rifting, possibly in conjunction with rising, late-Miocene global sea levels, the proto-Gulf of California and Salton Trough region were inundated by marine waters (Winker, 1987). Marine deposits extending for almost 400 km north of the modern Gulf of California, to San Gorgonio Pass, provide evidence of the ensuing sea, designated the Imperial Sea (Dorsey, 2006). However, the late Miocene Imperial Sea was only an estimated 50 km in
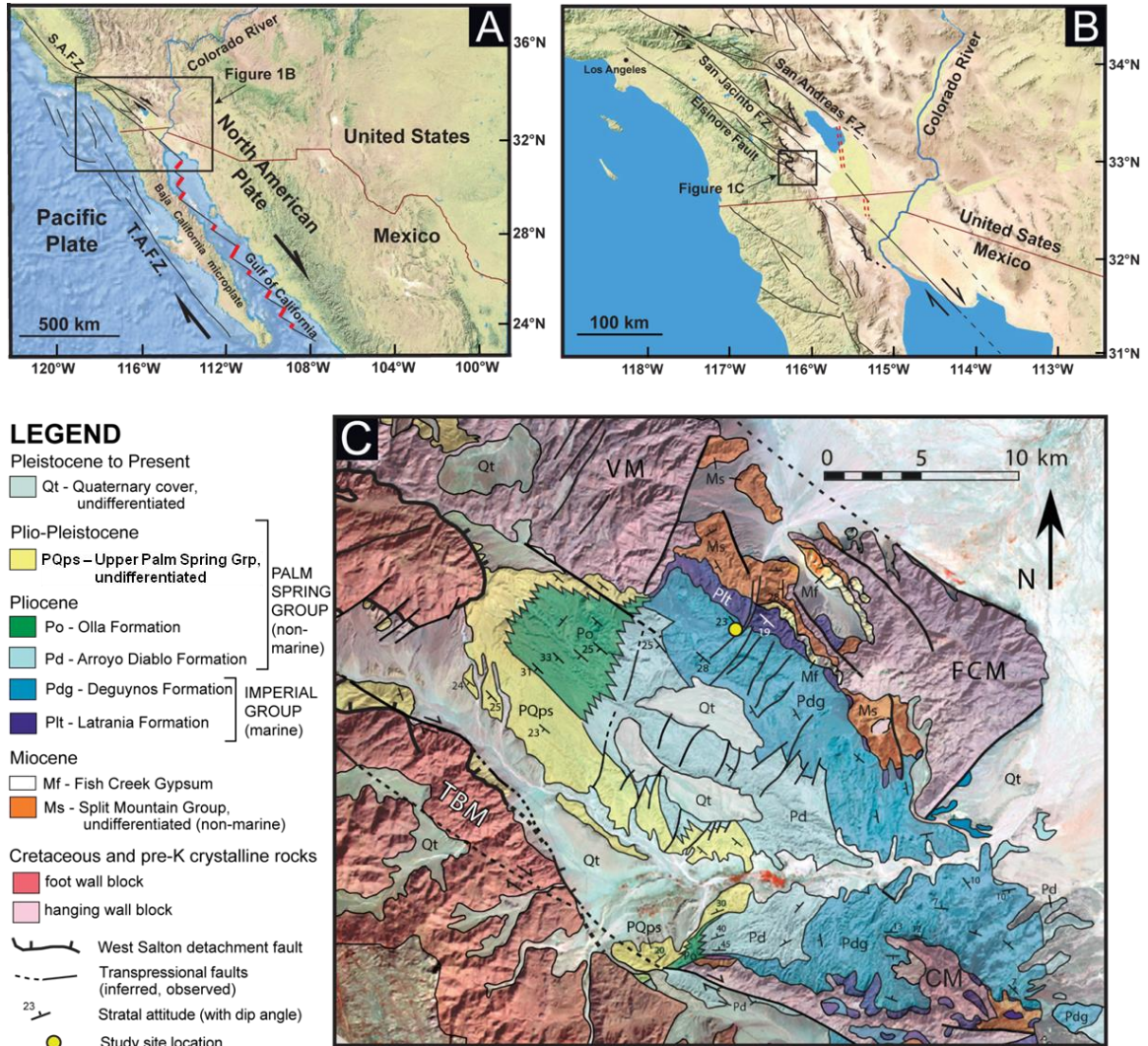
Figure 1. (A) Simplified regional tectonic map along the southwestern United States and northwestern Mexico boundary. Miocene transtensional rifting caused the Baja California microplate to rotate away from Mexico, opening up the early Gulf of California. S.A.F.Z. = San Andreas Fault Zone; T.A.F.Z. = Tosco-Abreojos Fault Zone. Lineaments after Dorsey and Umhoefer (2012). Basemap courtesy of ESRI and Google Earth. (B) Map of the Salton Trough region showing main tectonic lineaments. The Salton Trough is an elongate, transtensional basin spanning the boundary between the Pacific and North American plates and originated on the hanging wall of a detachment fault related to Miocene rifting of the early Gulf of California. Lineaments after Dorsey (2006). Basemap courtesy of ESRI. (C) Geologic map of the Fish Creek-Vallecito Basin. VM = Vallecito Mountains; FCM = Fish Creek Mountains; CM = Coyote Mountains; TBM = Tierra Blanca Mountains. The study site is marked with a yellow dot. Image modified from Dorsey et al. (2011).

8

width (compared to the modern Gulf of California average width of 150 km) and comprised a long, narrow marine embayment (Dorsey et al., 2006; Winker, 1987).

Pliocene deposits in the Salton Trough region and, significant to this study, the FCV sub-basin within, record the subsequent influx of the ancestral Colorado River from the north (F 2) (Winker, 1987). The Colorado River deposited an immense volume of sediment into the narrow, marine embayment, and a delta rapidly prograded, despite moderate to rapid subsidence of the basin (Dorsey et al., 2011).

The progression of the lower Colorado River from its catchment (Colorado Plateau) to the sea (Gulf of California) may be explained by the lake-spillover model, which was first proposed over a century ago by Newberry (1861) and has increasingly gained support in the last decade following stratigraphic, tectonic, microfaunal, detrital zircon, and stable isotope studies (Blackwelder, 1934; Bright et al., 2016; Cloos, 2014; Dorsey, 2010; Dorsey et al., 2007; House et al., 2005; House et al., 2008; Howard et al., 2014; Kimbrough et al., 2011; Meek and Douglass, 2001; Roskowski et al., 2010). Essentially, upon its exit from the Colorado Plateau, the Colorado River entered the Basin and Range Province, flooding and catastrophically breaching the paleodivides of a series of topographically confined basins (F 3). Repeated filling and breaching by the Colorado River may have resulted in numerous pulses of flow and sediment to the Salton Trough region, with potential important implications for depositional processes recorded downstream.

Since the late Miocene, slip along the San Andreas fault system translated the Pacific plate (and hence the western Salton Trough and FCV basin) an estimated 200 km to the northwest relative to the North American plate (and the apex of the Colorado
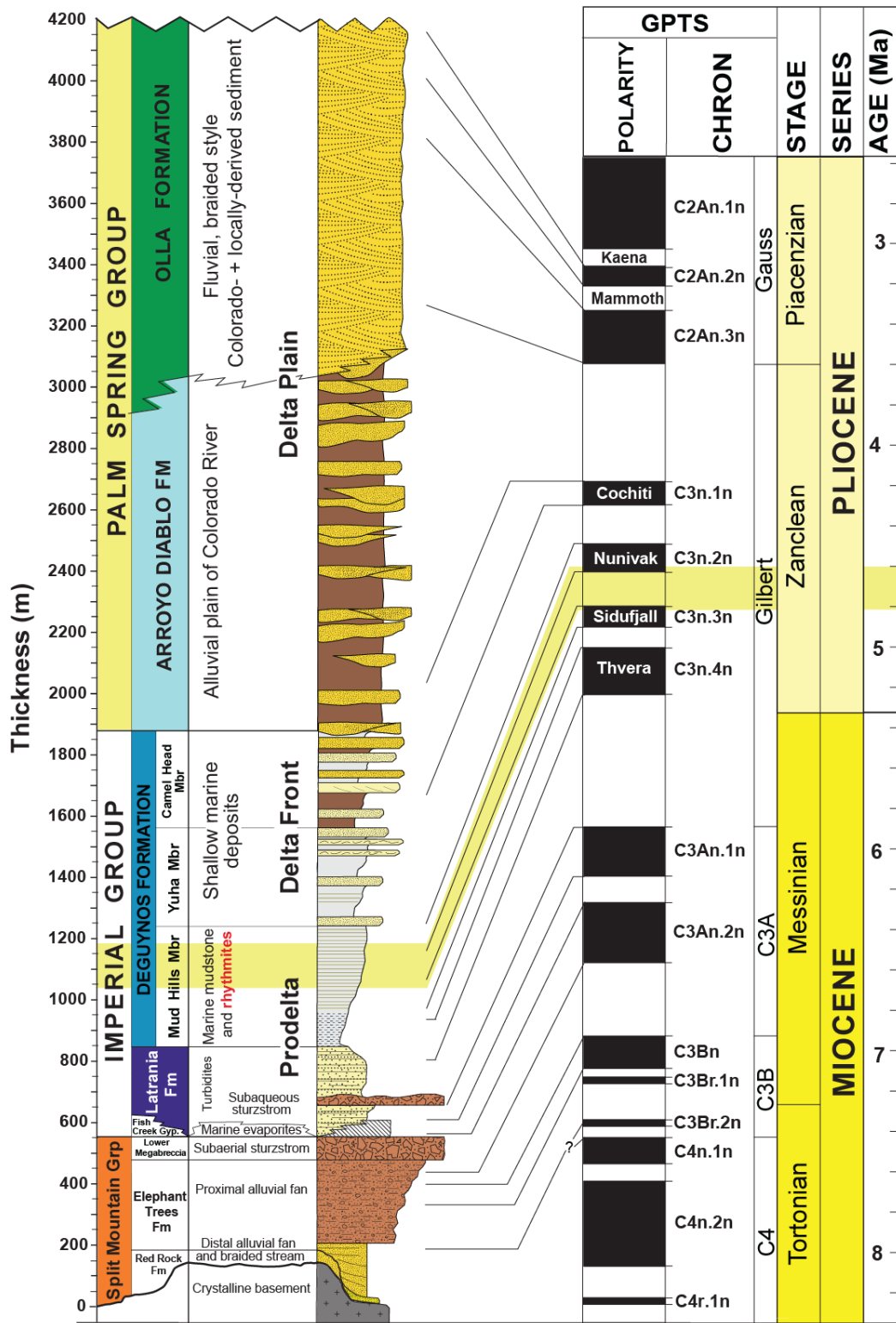
Figure 2. Composite lithostratigraphic column of the lower and middle part of the Fish Creek-Vallecito Basin sedimentary infill, showing thicknesses and correlation with the geomagnetic polarity time scale (GPTS). Colors of lithostratigraphic units are the same as in map of F 1C. The oldest sediments in the basin comprise the Miocene, non-marine, Split Mountain Group, which overlies igneous and metamorphic basement rocks (Dorsey, 2006). The earliest marine sediments mark the upper boundary of the Split Mountain Group (Dorsey, 2006). The earliest evidence of Colorado River-derived sediments occurs in the upper Latrania Formation (Winker and Kidwell, 1996). The overlying Deguynos Formation records the progradation of the Colorado River delta and transition to predominantly alluvial deposits of the Palm Spring Group (Winker and Kidwell, 1996). The studied succession (Mud Hills Member rhythmites), highlighted in yellow, spans a polarity reversal. Image modified from Dorsey et al. (2011).
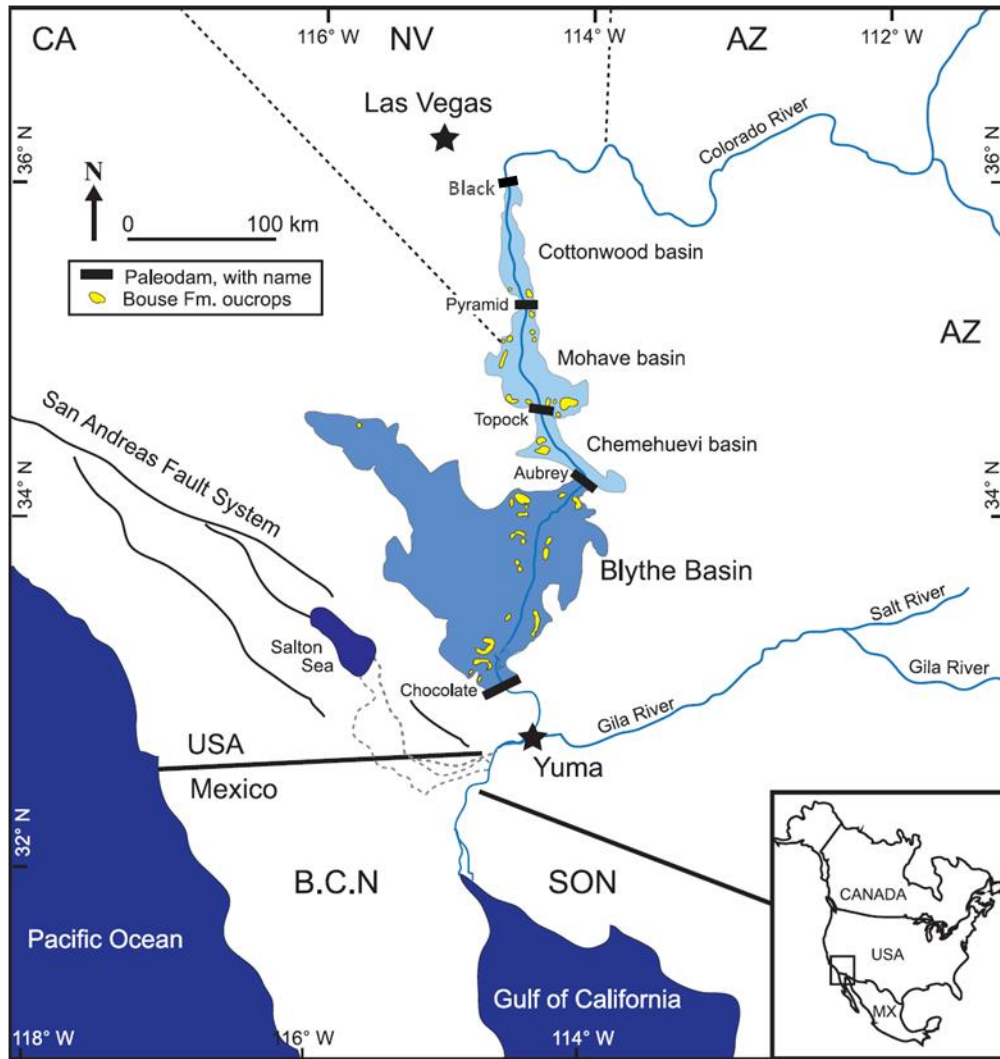
Figure 3. Diagram depicting the modern Colorado River in relation to several ancient lake basins and hypothesized paleodam locations. The Colorado River may have evolved from its catchment (Colorado Plateau) to sea level (Gulf of California) by sequentially infilling lakes and overtopping the natural barriers. Modified from Bright et al. (2016) and House et al. (2008).

River) (Dorsey, 2006). Initiation and propagation of the Elsinore, San Felipe, and San Jacinto strike-slip faults, which crosscut the West Salton detachment fault, eventually led to the termination of slip along the West Salton detachment fault (Dorsey et al., 2012). Subsequently the region was uplifted due to transpression and the FCV basin section was exhumed (Dorsey et al., 2012).

Fish Creek-Vallecito Basin

The FCV basin is located along the western margin of the Salton Trough (F 1C). The FCV basin is bounded to the north by the Vallecito Mountains, to the east by the Fish Creek Mountains, and to the south by the Coyote Mountains. Notably, the basin is bounded along the NW to SW margin by the curviplanar West Salton detachment fault and the Tierra Blanca Mountains (Peninsula Range) beyond (Axen and Fletcher, 1998; Winker, 1987). The basin covers an area of approximately 373 km^2, a large part of which is enclosed within the Anza-Borrego Desert State Park of southern California (Remeika, 1995).

Accommodation in the FCV basin was accomplished by Miocene low-angle rifting of the West Salton detachment fault (Axen and Fletcher, 1998; Dorsey et al., 2007). Approximately 5.5 km of Miocene to Pleistocene sediments of the FCV section fill the southwest-dipping hanging wall of the half-graben formed by the West Salton detachment fault (Gibson et al., 1984; Peryam, 2012). Ages of FCV basin deposits have been calibrated in detail from magnetostratigraphic studies (F 2) and by two radiometric ages acquired from tuffs high in the Palm Spring Group section (Dorsey et al., 2007; Dorsey et al., 2011; Johnson et al., 1983; Opdyke et al., 1977). The oldest sediments in

13

the basin comprise the Miocene, non-marine, Split Mountain Group, which overlies igneous and metamorphic basement rocks (F 1C, 2) (Dorsey, 2006). The earliest marine sediments are found at the base of the overlying Imperial Group (Fish Creek Gypsum, Latrania Formation; F 1C, 2) (Dorsey, 2006). The earliest evidence of Colorado River-derived sediments in the Imperial Group occurs in proximity to the Miocene-Pliocene boundary in the upper Latrania sandy turbidites (F 1C, 2) (Winker and Kidwell, 1996). The overlying Deguynos Formation records the progradation of the Colorado River delta and transitions into the fluvio-deltaic deposits of the predominantly non-marine Palm Spring Group (F 1C, 2) (Winker and Kidwell, 1996). The FCV basin is capped off with Plio-Pleistocene lacustrine and locally-derived stream sediments overlain by Quaternary deposits (Winker, 1987).

Mud Hills Member Rhythmites

The Latrania Formation turbidites (lower Imperial Group) are conformably overlain by the lower Mud Hills Member (informally known as "Coyote Clays") of the Deguynos Formation (F 2) (Hanna, 1926; Winker, 1987). Gradationally above the "Coyote Clays", the upper MHM contains an approximately 255 m-thick succession of rhythmically bedded muddy siltstones to fine sandstones, interpreted as a prodeltaic unit formed when the early Colorado River discharged sediment in the basin (Dorsey et al., 2011; Winker, 1987; Winker and Kidwell, 1996). The MHM rhythmites are impressively exposed in cliff walls along Fish Creek Wash, the location of this study (F 1C). Here the exposed strata trend NW-SE with average dips to the southwest of approximately 12 degrees.

CHAPTER THREE

METHODS

Field Work

Analysis focused on the midportion of the ~400 m-thick Mud Hills Member where clear rhythmic bedding is first exposed (F 4). Observations were made below and above the studied interval to provide context. Section designations were modified after Winker (1987): "FC" stands for Fish Creek Wash and "6" indicates the location of the Mud Hills Member rhythmite wall, the focus of this study. The stratigraphically lower, mid, and upper sections of the rhythmite wall are labeled FC6-1, FC6-2, and FC6-3, respectively (F 4).

The three sections were divided into segments (50 total, ranging from 33 to 194 cm thick) that were cleaned and measured along lines constructed normal to bedding. Due to the dip of strata (~12°), measurements of contiguous segments could be made by moving laterally along outcrop, continuing up-section without a break (F 5). Bed thickness was measured using an aluminum ruler with mm precision and measurements have an estimated margin of error of +/- 0.25 cm. Generally, contacts between alternating coarse-grained and fine-grained beds were visually distinguished by changes in color, grain size, and/or the presence of bedding. Contacts especially gradational in nature were measured in three to five locations adjacent to and including the segment line constructed normal to bedding, and the most frequent measurement was used.

Field work concentrated on section FC6-2 which is characterized by couplets consisting of a coarse-grained bed overlain by a fine-grained bed. Out of the total measured distance of FC6-2 (~33 m), detailed logging was performed on an ~22 m-thick
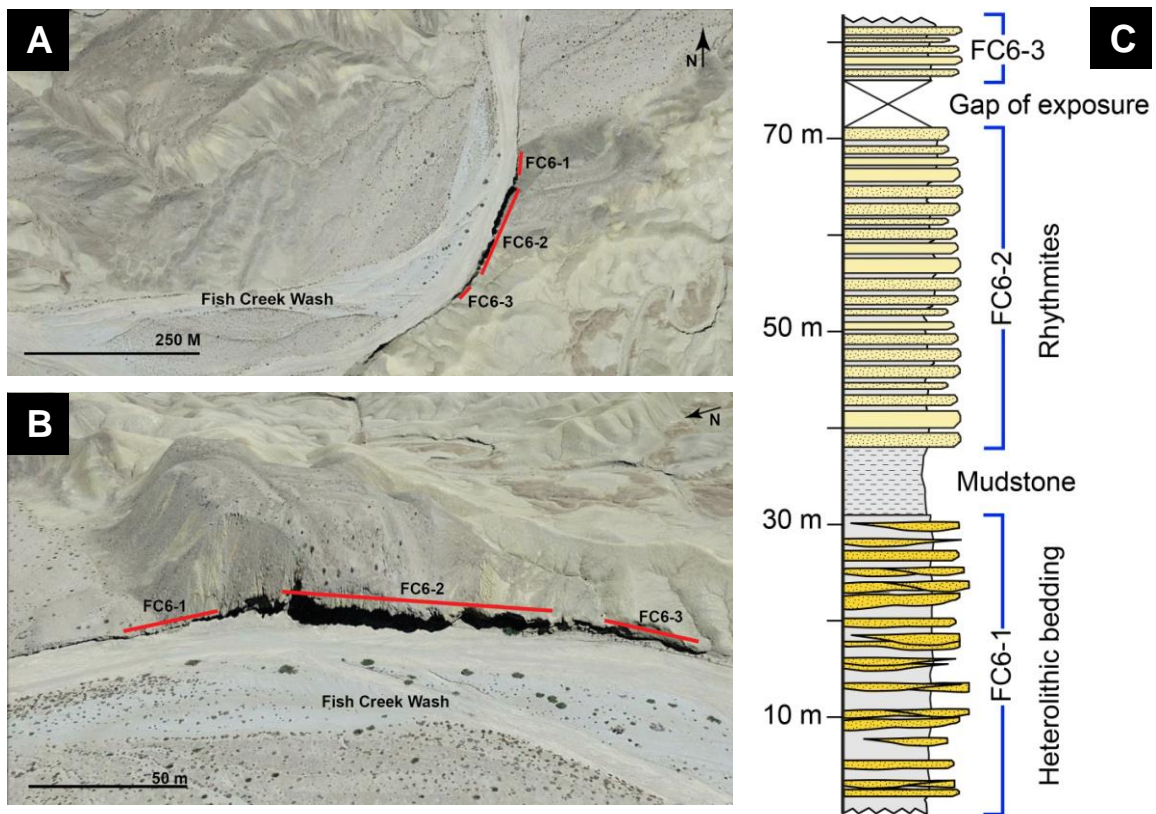
Figure 4. (A) Google Earth image of Mud Hills Member outcrop along Fish Creek Wash in plan view. Lower, mid, and upper studied sections are, respectively, FC6-1, FC6-2, and FC6-3. (B) Oblique view of outcrop. (C) Stratigraphic section of MHM outcrop. Google Earth V 7.1.5.1557. 2016. *Mud Hills Member rhythmites, Fish Creek Wash. 32° 59' 08.32"N, 116° 07' 38.29"W, Elevation 163 m.* INEGI 2016. <http://www.google.com/earth/index.html> [Viewed June 2, 2016].
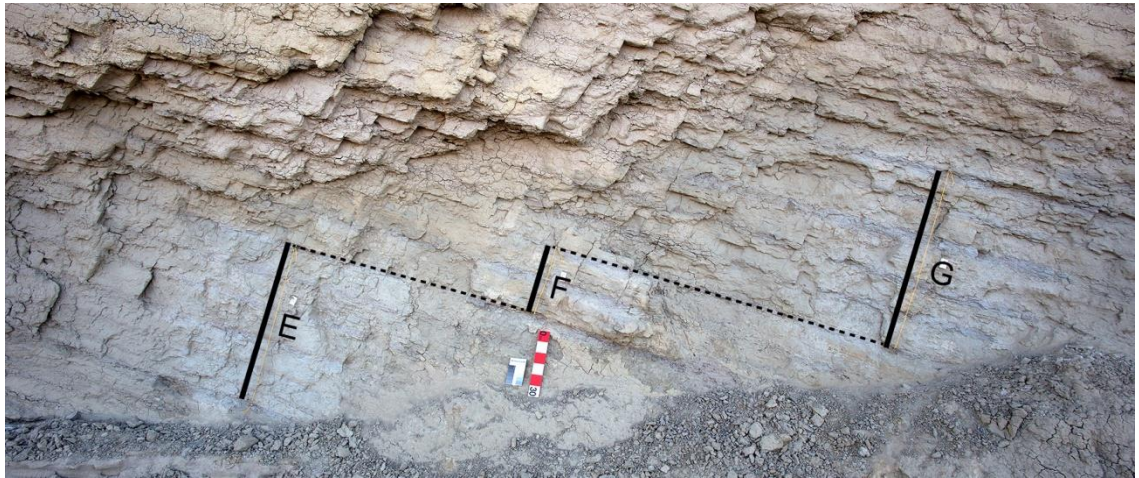
Figure 5. Representative outcrop image showing the method of measuring contiguous segments by moving laterally along outcrop (Segments E-G of Section FC6-2). Red and white scale is 30 cm long.

subset (segments A-U). The outcrop face of section FC6-2 is nearly aligned with average dip direction (~209°; F 4), therefore, bed thickness measurements give a very close approximation to true thickness. Logging included photography and description of sedimentary structures, the nature of bedding contacts, bioturbation and erosional features, and estimate of grain size. After consideration of the variability of lithological characteristics through the logged segments, a facies scheme was created and compared with analogous facies descriptions existing in the literature.

The lower section (FC6-1) was categorized into four facies based on visual estimate of % sand, and ~31 m were measured. A deeply weathered slump obscures an estimated 7 m of bedding between FC6-1 and FC6-2. Another break, between FC6-2 and FC6-3, is approximately 6 m thick and was excluded due to several faults hindering correlation. Approximately 6 m of the upper section (FC6-3) were measured.

Laboratory

Thin Sections

Samples for thin sections were collected from several couplets (S4-5; T2-5) in section FC6-2 and outsourced for preparation to Calgary Rock and Materials Services, Inc. Six thin sections (~5 x 7 cm each) were examined to better discern texture, small-scale sedimentary structures, evidence of bioturbation, presence of organic matter, and microfacies variations using a Leica DM2500P petrographic microscope. Microphotographs were taken with a mounted Motic 580 Digital Camera. Sedimentary features identified microscopically were compared to analogous prodeltaic features documented in the literature.

Grain Size Analysis

Grain size analysis was performed to better discern grain-size distributions of individual samples and vertical trends in grain size within the couplets (Soyinka and Slatt, 2008). High-resolution sampling for quantitative analysis of grain-size variability using the Beckman Coulter LS 13 320 laser diffraction particle size analyzer was performed. Samples were procured at three distinct levels on the main section (FC6-2: segments C, M, T), and three contiguous couplets (C2-4, M1-3, and T5-7) were sampled at each level, for a total of 9 sampled couplets (F 6). Eight evenly spaced samples were collected for each couplet, the first sample at the base and the last sample at the top. To explore the possibility of lateral variability in the couplets, the three couplets of segment M were sampled to the left (ML) and to the right (MR) along an ~8.5 m parallel transect (F 7). For each couplet in segments ML and MR two samples were obtained, one from the center of the coarse bed and one from the center of the fine bed. Specimens were disaggregated in a sodium hexametaphosphate solution (1g/L) using a sonic probe (Heat Systems-Ultrasonics Cell Disruptor) prior to processing with the particle size analyzer.

X-Ray Diffraction Analysis

In order to quantitatively evaluate variability in mineralogical composition, high-resolution sampling with the same strategy and using specimens from the same samples as for grain size analysis (F 6 and 7) was performed. An ~1.0 g specimen from each sample, previously crushed with a Plattner's mortar and pestle, was combined with ~0.25 g of alumina powder standard (1.0 μ, De-Agglomerated). The powder combination, steel grinding beads, and IPA alcohol were placed in a grinding jar and ground at 30 cycles
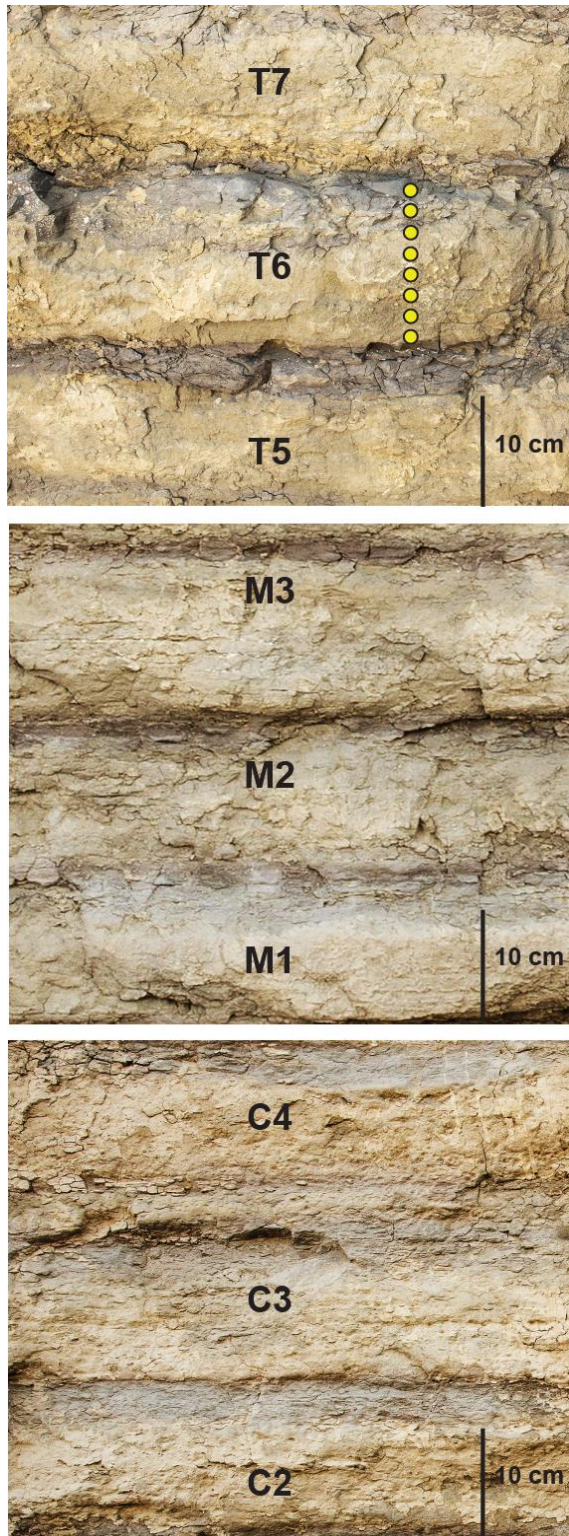
Figure 6. Photos of couplets from which samples were acquired for XRD and grain size analyses. Yellow dots on couplet T6 show spacing method used for sampling: 8 evenly spaced samples per couplet were acquired, starting at base of coarse-grained interval and ending at top of fine-grained interval.
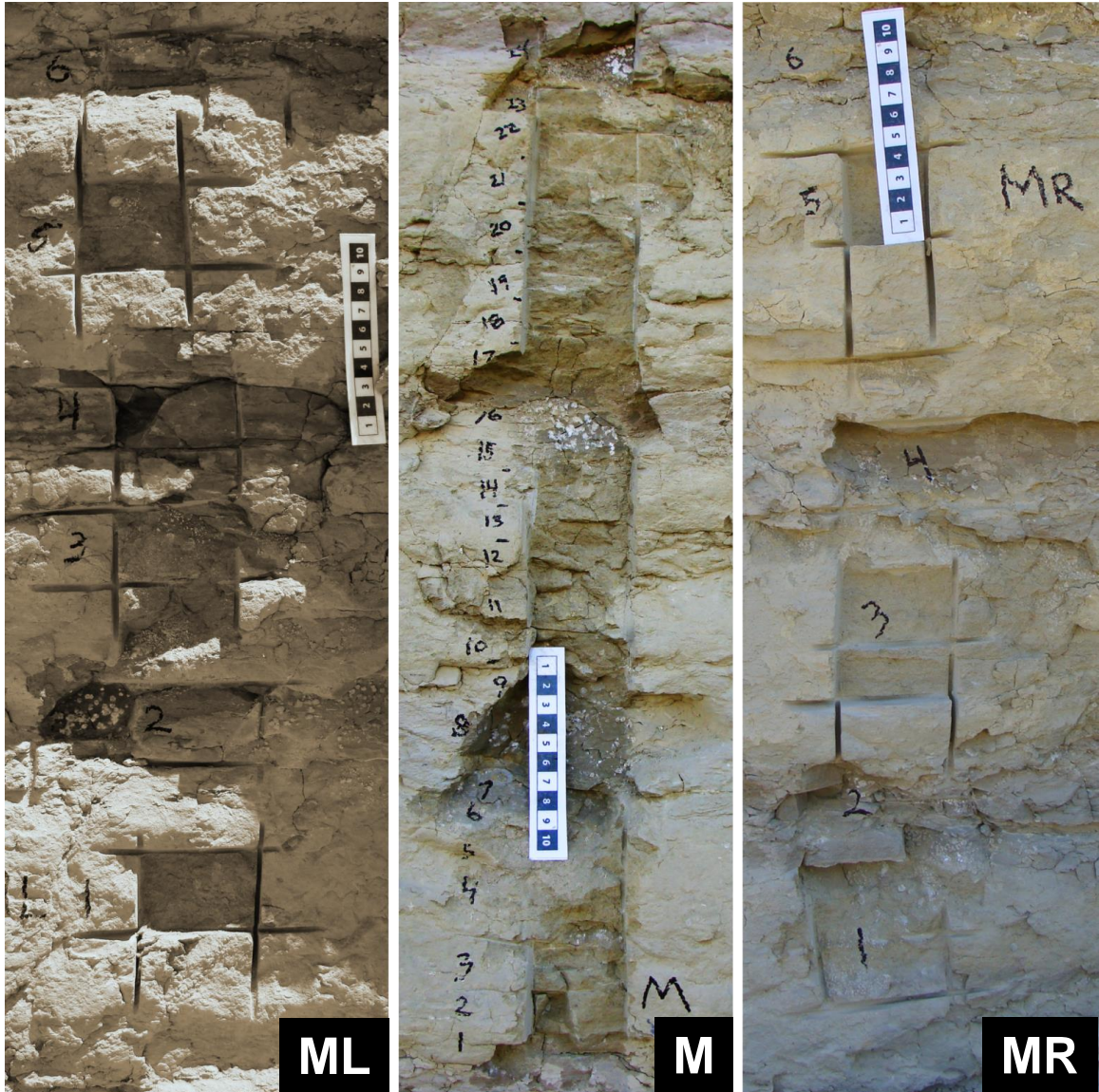
Figure 7. Photos of sample locations taken from segment M, couplets 1, 2, and 3 (center), segment ML (left; same couplets as M but located ~4 m to the left of segment M), and segment MR (right; same couplets as M but located ~4 m to the right of segment M). Total lateral distance from segment ML to segment MR is ~8.5 m.

per minute for 20 minutes with the Retsch MM 400 Grinder. The slurry was left to dry

for 24 hours before separating the beads from the specimen. The dried specimen was

lightly powdered with a mortar and pestle, backloaded into a specimen holder ring, and

analyzed with a Bruker D8 Advance X-ray Diffractometer. The results were evaluated

using Bruker DIFFRAC.EVA software.

Time Series Analysis

Bed Thickness

To test the hypothesis that the MHM rhythmites show a nonrandom variation in

thickness, time series analysis was performed by an outside source on field-measured bed

thickness of 265 consecutive couplets, for a total thickness of ~33 m in section FC6-2.

The thickness of the coarse-grained portion of each couplet was selected for analysis as

representative of the whole couplet. The fine-grained portion was excluded from analysis

since possible erosion subsequent to deposition may have altered the thickness of the

fine-grained beds.

Grayscale Intensity

Time series analysis was performed on image brightness values of a composite

photographic log converted to grayscale, covering the subset of 159 consecutive couplets

(~22 m) from section FC6-2 (segments A-U). High resolution digital images were taken

with particular attention given to minimizing differences in exposure, distance, and angle

of image acquisition. Photos were uniformly processed, cropping the outer ~30% of each

image to reduce lens distortion and applying corrections to maximize texture and

contrast. Images were stitched in Canon PhotoStitch or Adobe Photoshop, and a color photolog was produced. The log was then converted to grayscale using a grayscale comparator included in each photo during picture acquisition to normalize the gray values after conversion. The time series analysis of image brightness (grayscale) values was subsequently sourced out.

CHAPTER FOUR

RESULTS

Field Work

Lower Section: FC6-1

The lower section (FC6-1) underlies the primary rhythmite interval and is visually distinguished from it in outcrop by the predominance of heterolithic lamination at a fine (cm to mm) scale. In FC6-1, measurements of 459 beds totaled ~30.9 m (F 4C; Appendix A). Average bed thickness is 5.1 cm excluding two anomalously thick beds (280 cm and 471 cm) (Table 1). Fifty percent of the beds in section FC6-1 are sand-rich with average bed thickness of 6.6 cm. Mud-rich beds average 4.3 cm.

Table 1. Bed thickness statistics for section FC6-1.

FC6-1	All beds (cm)	Sand-rich (cm)	Mud-rich (cm)
Mean	5.1	6.6	4.3
Median	4.0	5.0	3.0
Mode	3.0	5.0	3.0
Total	30.9 m	15.4 m	15.4 m
Percent	100%	50%	50%

Deposits of FC6-1 are categorized into four facies: sand-dominated (Sd, ~>75% sand); sand-rich (Sm, ~50-75% sand); mud-rich (Ms, ~25-50% sand); and mud-dominated (Md, ~<25% sand) (F 8A, 8B). The sand-rich (Sd, Sm) facies often display a distinct heterolithic character (F 8B, 8C), and structures include discontinuous to continuous parallel lamination, wavy lamination, occasional troughs with cross-laminae,
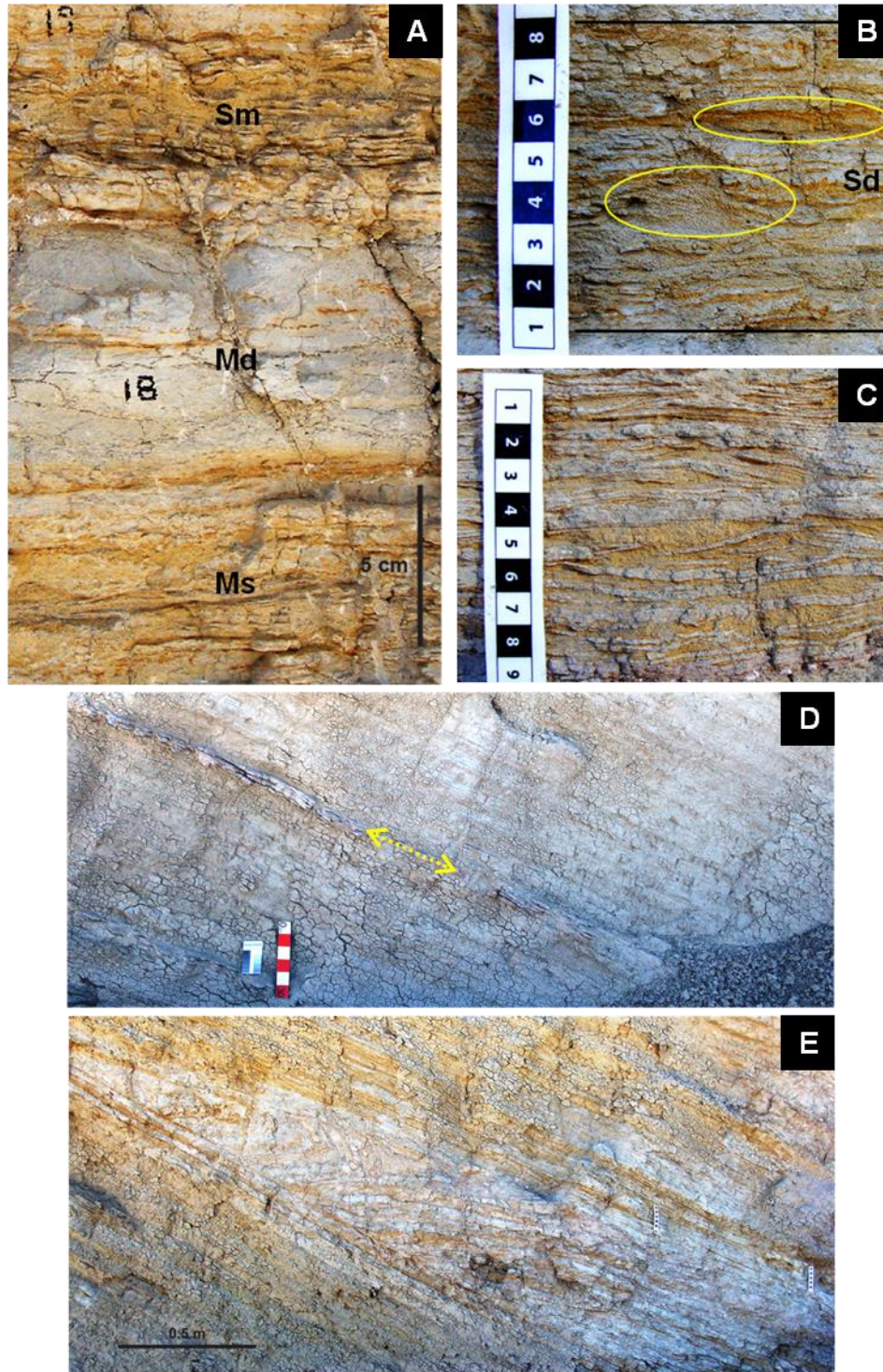
Figure 8. Sedimentological details from section FC6-1. (A) Representative facies Ms, Md, and Sm (see text for description). (B) Representative facies Sd with ripple cross-laminae encircled in yellow. (C) Heterolithic bedding with symmetric ripple cross-lamination. (D) Heavily cemented bed with ripple cross-lamination forms ridge (indicated by arrow). Scale bar is 30 cm. (E) Large slump sandwiched between undisturbed beds.

and symmetric ripple cross-lamination. Distinct beds with positive relief, mostly comprised of heavily cemented sand with ripple cross-lamination, occur occasionally (F 8D). The mud-rich facies (Ms) displays occasional parallel or wavy sandy laminae and rare low-angle sandy cross-laminae (F 8A). Bioturbation is common but does not obliterate primary structures. Several examples of slumping (F 8E) and low-relief scouring at the scale of tens of centimeters to meters are observed in this section. In general, apart from slumps, beds display good lateral continuity showing no significant changes in thickness for several meters. Stratigraphically above the heterolithic deposits, a massive, poorly exposed, dark gray mudstone, ~7 m thick, lies directly below the first rhythmite of section FC6-2 (F 4C).

Interpretation: Section FC6-1

Heterolithic lamination points to periods of flow alternating with slackwater suspension fallout of fines (Reineck and Singh, 1980). Higher energy, unidirectional flow is indicated by planar-parallel lamination, wavy lamination and occasional scours filled with sandy cross-laminae. Abundant mud and moderate bioturbation suggest periods of quiescence. Occasional symmetrical ripples indicate oscillatory bi-directional flow. Rare, large slumps could result from deformation of fluid-impregnated sediment due to gravity (rapid sediment loading), wave pounding, or dragging by unidirectional currents. This facies association fits well with the general interpretation of the Mud Hills Member as a prodeltaic unit (Bhattacharya, 2006; Bhattacharya and MacEachern, 2009; Gani and Bhattacharya, 2007; Li et al., 2015; Winker, 1987).

Primary Section: FC6-2

Within the primary studied interval, FC6-2, 265 couplets of alternating coarser

and finer beds measured ~33.2 m with an average thickness of ~12.5 cm (F 4C; Table 2;

Appendix B). The coarser-grained, sand-rich beds are 10.7 cm-thick on average and

comprise ~85% of the total section. The finer-grained, mud-rich beds are 1.8 cm-thick

on average, comprising ~15% of the section. The average couplet thickness gradually

increases from the base (~10 cm) to about mid-section (~17 cm) and then gradually

decreases to the top (~8 cm) of the section (F 9). A basic test of the degree of

dependence (Spearman's rho) revealed a statistically significant, positive correlation

between the thicknesses of the fine-grained and coarse-grained portions of the 265

couplets of section FC6-2 (Table 3).

Table 2. Bed thickness statistics for primary studied section, FC6-2, including total
couplet, the lower sand-rich beds ("Coarse beds"), and the upper, mud-rich beds ("Fine
beds").

FC6-2	Couplet (cm)	Coarse beds (cm)	Fine beds (cm)
Mean	12.5	10.7	1.8
Median	12.0	10.0	2.0
Mode	12.0	9.0	1.0
Total Measured	33.2 m	28.3 m	4.8 m
Percent	100%	85%	15%

The couplets have good lateral persistence of at least tens of meters and

gradational to sharp, flat contacts (F 10 and 11). Observed sedimentary structures are

concentrated on the coarser portion of the couplets and mostly consist of planar and
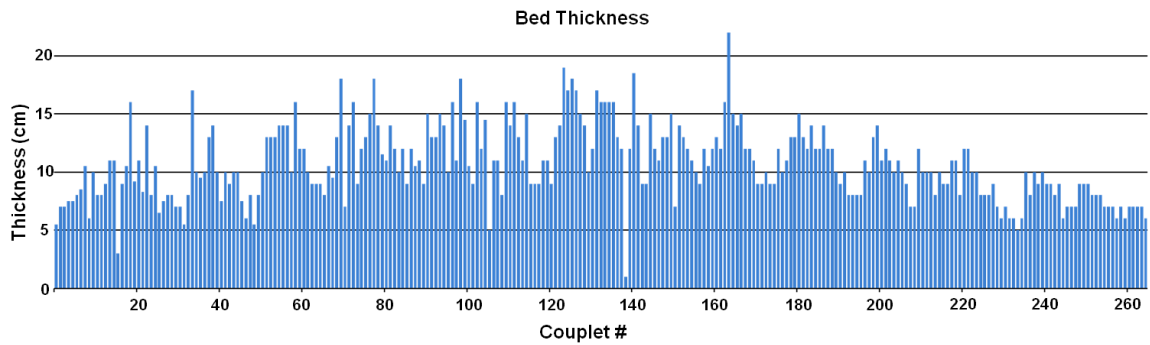
Figure 9. Plot of thickness (cm) of 265 coarse-grained beds from segments Aa-AA (section FC6-2) showing a general increase in bed thickness towards the center of the section followed by a decrease in thickness towards the top of the section. Up-section is to the right.

Table 3. Results of Spearman's rho statistic test on coarse-grained and fine-grained intervals of 265 couplets in FC6-2 (segments Aa-AA). (Top) Correlation between coarse and fine beds was positive and significant (Spearman's rho=.303, P < .001). (Bottom) After adjusting for the ratio between coarse and fine thicknesses, the positive correlation was stronger and significant (Spearman's rho = .908, P < .001).

| FC6-2 Unadjusted | | RANK | |
		Coarse Beds	Fine Beds
Rank Coarse Beds	Correlation Coefficient	1	0.303
	Significance (2-tailed)		0
	N	0	265
Rank Fine Beds	Correlation Coefficient	0.303	1
	Significance (2-tailed)	0	
	N	265	0

| FC6-2 Adjusted | | RANK | |
		Coarse Beds	Fine Beds
Rank Coarse Beds	Correlation Coefficient	1	0.908
	Significance (2-tailed)		0
	Degrees of Freedom	0	262
Rank Fine Beds	Correlation Coefficient	0.908	1
	Significance (2-tailed)	0	
	Degrees of Freedom	262	0

wavy lamination (F 11A,C,D,F;), with subordinate ripple cross-lamination (F 11B) and localized internal scours, mm- to cm-thick (F 11B,E) (see Appendix C for sedimentary log). An upward transition from massive to faintly laminated, to distinct continuous or discontinuous planar lamination, and then wavy- to cross-lamination is observed in several of the coarse beds (F 11A,C).

Interpretation: Section FC6-2

Rhythmic bedding, with good lateral continuity, composed of sand-rich layers with physical sedimentary structures overlain by mud-rich intervals is a common

Figure 10. Photomosaic of section FC6-2 (segments A-U) highlighting the good lateral persistence of rhythmic bedding. Ladder for scale is 2 m.
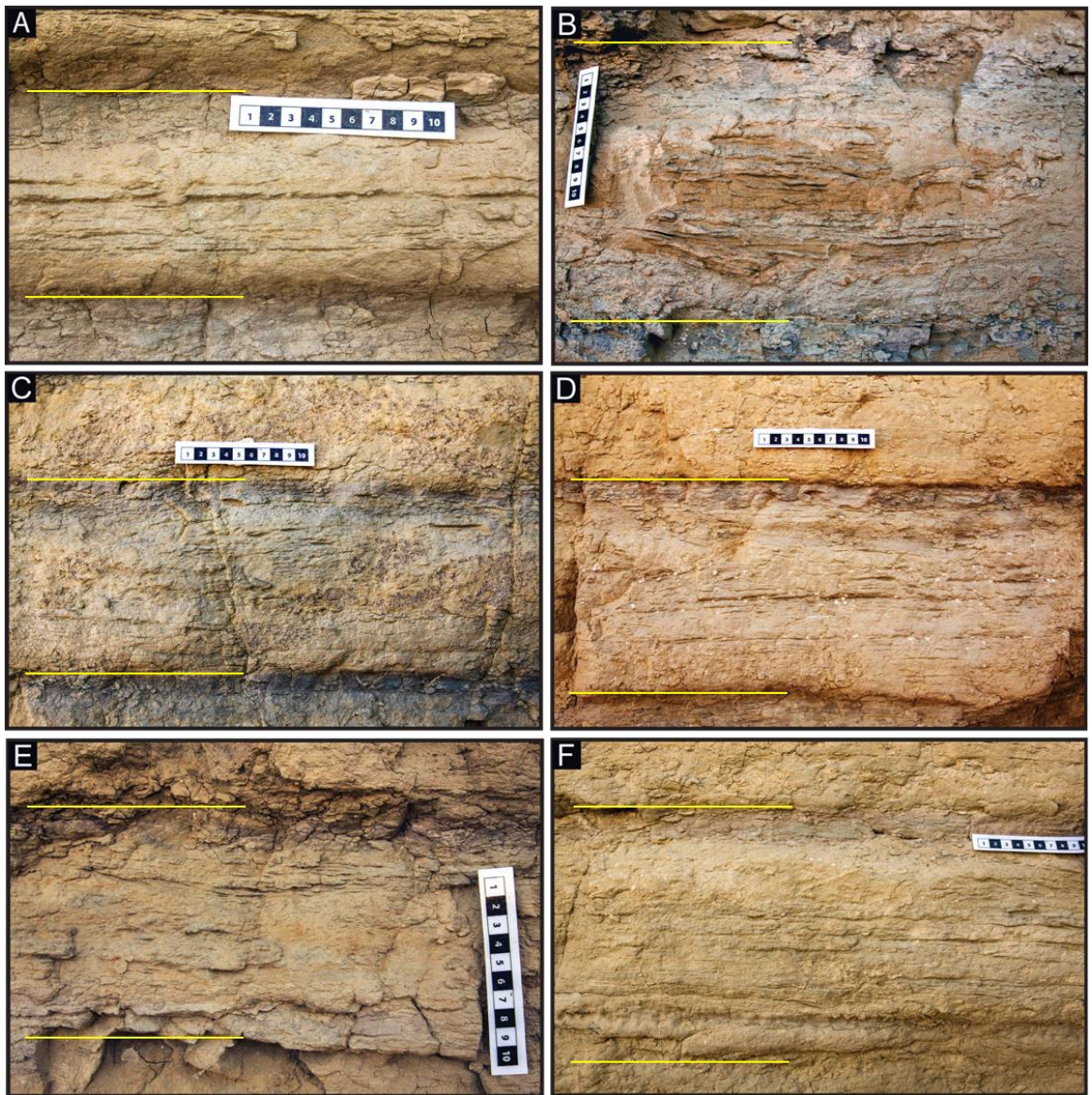
Figure 11. Representative photos documenting structures commonly found in the lower, coarser-grained beds of couplets in section FC6-2. Yellow lines show approximate base and top of couplets. (A) This couplet shows a sharp contact at the base and gradational contact at the top, as well as distinct planar lamination. (B) Gradational contacts at base and top; internal scour with ripple cross-laminae. (C) Transition from massive at base, to planar lamination followed by wavy lamination. (D) Planar lamination throughout, with some wavy lamination near the top. (E) Scour at top of coarse-grained layer. (F) Planar lamination within lower 2/3 of coarse-grained bed; ripple cross-laminae at top, below scale.

depositional product of sediment gravity flows such as turbidites and hyperpycnites (Mulder and Alexander, 2001; Mulder et al., 2003). The sedimentary structures (parallel lamination, ripple cross-lamination, scours, wavy bedding and ripples) within the sand-rich interval are indicative of turbulent, unidirectional flow with high, though fluctuating, energy. The mud-rich interval could be interpreted as having formed from background sedimentation or settling of the fine-grained portion of a sediment plume during the waning stage of a sediment gravity flow (Mulder and Alexander, 2001; Mutti, 2003). Positive correlation between thicknesses of the fine-grained and coarse-grained portions suggests the two represent different phases of the same depositional event. Additionally, the correlation suggests erosion of the upper, fine-grained portion of each couplet was minimal.

Upper Section: FC6-3

Stratigraphically above the primary rhythmite interval, section FC6-3 is distinct from it in that the average couplet thickness is significantly smaller, but sedimentary structures and the typical alternation of fine and coarse beds are the same as in FC6-2. Couplets in this section were not included in FC6-2 due to several vertical offsets between sections that prevented correlation. Approximately 6 m of section were measured (88 couplets) and the average couplet thickness is 6.9 cm (F 4C; Table 4; Appendix D). The lower, coarser-grained beds of the couplets make up ~82% of the total, with an average 5.7 cm thickness; finer-grained beds amount to ~18% and are 1.2 cm-thick on average (Table 4). Generally, average couplet thickness remains constant throughout the section.

Table 4. Bed thickness statistics for upper section FC6-3.

FC6-3	Couplet (cm)	Coarse beds (cm)	Fine beds (cm)
Mean	6.9	5.7	1.2
Median	7.0	5.0	1.0
Mode	7.0	5.0	1.0
Total Measured	6.06	4.99	1.07
Percent	100%	82%	18%

Laboratory

Thin Sections

Six large thin sections (~5x7 cm) were obtained from several couplets (S4-5; T2-4) in section FC6-2 (F 12). Photomicrographs reveal textural details of the coarse-grained and fine-grained portions of couplets (F 13). The coarse interval of each couplet consists of relatively poorly sorted, randomly oriented, silt- to fine sand-sized angular grains, with irregular subdomains rich in a fine intergranular matrix (F 13A). Clay-rich sub-domains locally form linear to irregular wisps (F 12A-F, 13H) and semi-circular to circular shapes infilled with coarser grains (F 12A-D,F, 13F). Fine-grained intervals are poorly sorted and contain abundant silt-sized grains dispersed in a finer matrix (F 13B), but clay matrix is locally predominant (F 12E, 13E). Both coarse and fine intervals contain elongate peloids (F 13C-D, G), often armored by silt-sized granules (F 13D) forming both lumps and discontinuous laminae. Though generally massive in appearance, some discontinuous faint lamination, marked by changes in mud content, is observed in some sections (F 12A,D,F). Transitions from coarse- to fine-grained beds (F 12E, F) or fine- to coarse-grained beds (F 12D) are generally gradational.

33
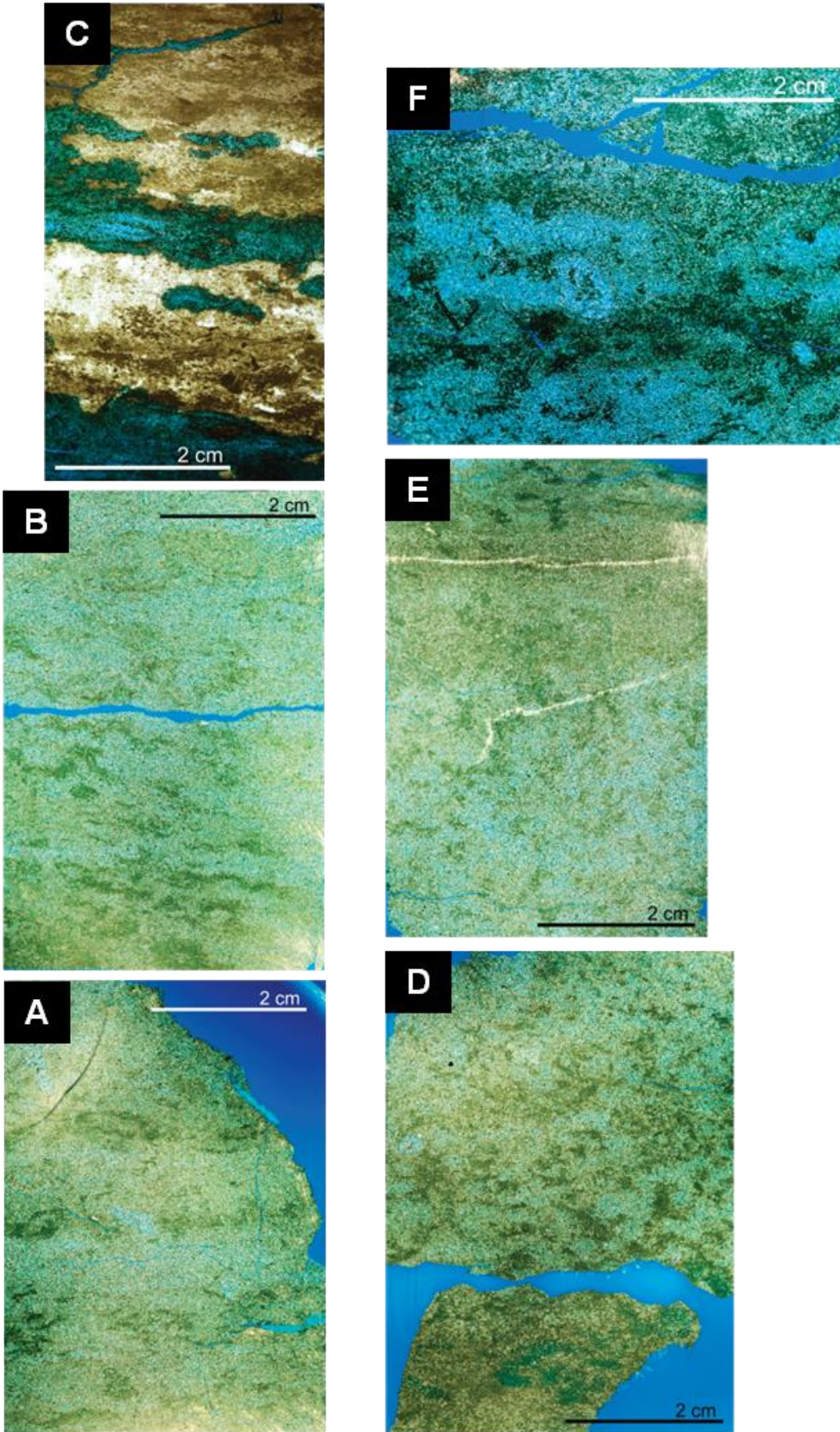
Figure 12. Photographs of thin sections in transmitted light (shown going 'up-section'). Blue color is epoxy resin used to impregnate the samples. (A) Coarse-grained (Cg) bed of couplet S4 showing irregular clay-rich sub-domains, semi-circular shapes infilled with coarser grains, and hint of discontinuous laminae. (B) Cg bed of couplet S5. (C) Fine-grained (Fg) bed of S5. (D) Transition from upper, Fg bed of T2 to lower, Cg bed of overlying T3. (E) Transition from Cg to Fg beds of couplet T3. (F) Transition from Cg to Fg beds of couplet T4.
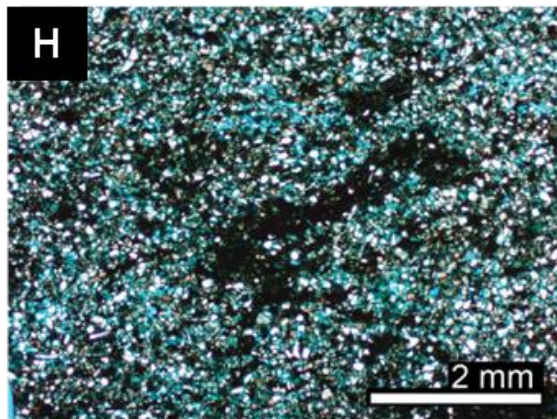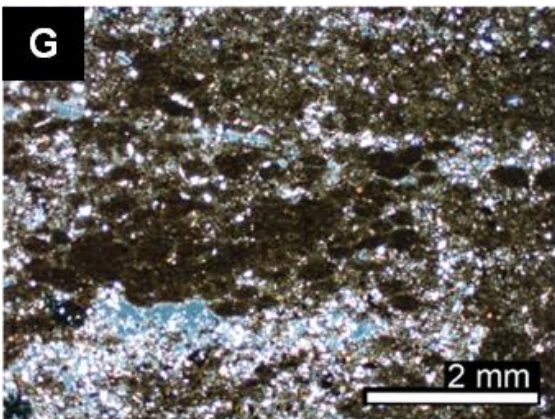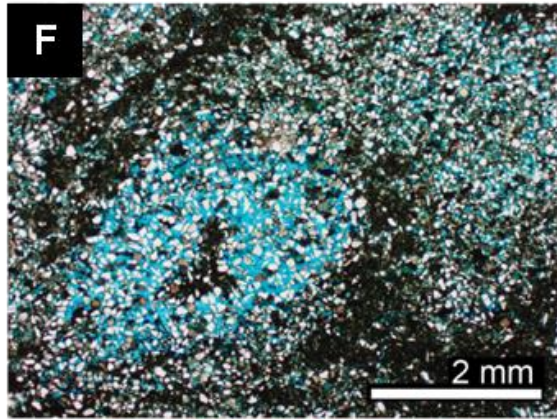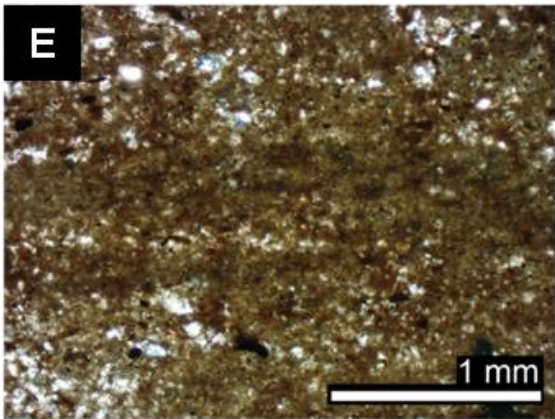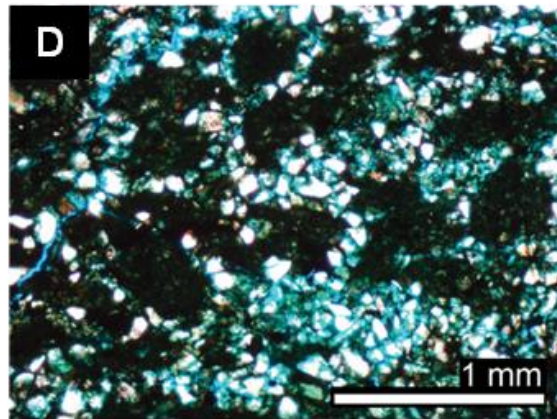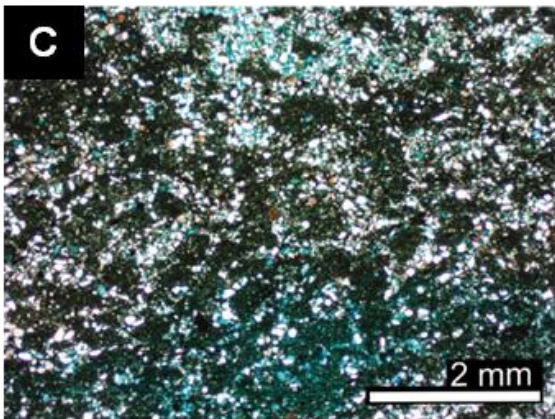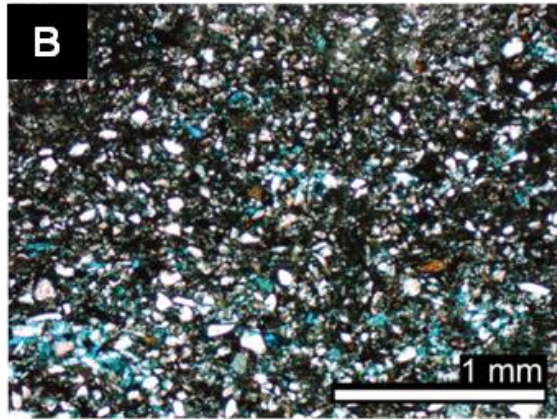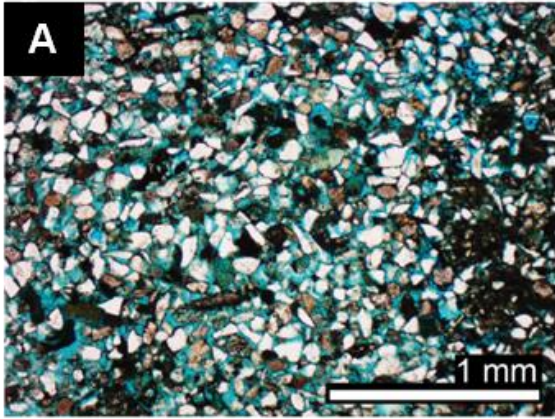
Figure 13. Photomicrographs in plane parallel light showing textural details from thin sections in F 12 (see text for details). (A) Representative coarse-grained (Cg) bed of couplet (T3; F 12D). (B) Representative fine-grained (Fg) bed of couplet (T3; F 12E). (C) Peloids in Fg bed of couplet T2 (F 12D). (D) Armored peloids in Fg bed of couplet T4 (F 12F). (E) Clay matrix of Fg bed of couplet S5 (F 12C). (F) Clay-rich, ~circular domain infilled with coarser grains in Cg bed of couplet T3 (F 12D). (G) Peloids in Fg bed of S5 (F 12C). (H) Clay-rich 'wisp' within Cg bed of couplet S4 (F 12A).

Interpretation: Thin Section Analysis

Textural immaturity (poor sorting, angular grains) is more likely a reflection of the fine grain size than degree of sediment transport (Prothero and Schwab, 1996). The clay-rich wisps and nearly circular shapes may possibly represent ghost traces of bioturbation, and the peloids could be interpreted as fecal pellets. If so, intermittent occurrences of bioturbation would suggest fluctuation of deposition rates or environmental stressors (e.g., salinity or temperature) (MacEachern and Bann, 2008). Alternatively, the peloids may be clay floccules. Aggregated clay particles are known to be transported and deposited at similar flow velocities as sand (Schieber et al., 2007). The peloids may, instead, represent intraclasts, suggesting velocities sufficient to erode the fine-grained portion of the underlying couplet. Alternation of clay-rich and sand-rich intervals, producing faint lamination, may be the result of oscillating energy or possibly the effects of bioturbation. Gradational contacts could have resulted from mixing via bioturbation or the result of gradually waxing and waning deposition.

Grain Size Analysis

Grain size analysis performed with laser diffraction techniques on several couplets shows a consistent pattern of inverse grading followed by normal grading (F 14; Appendix E). Grain size ranges from clay to fine-grained sand with rare medium sand, with average grain size of 43.4 µm (silt) (F 14; Table 5). The average grain-size distribution by volume is 69.0% mud (< 63 µm) and 31.0% sand (≥ 63 µm) (Table 5). The coarser-grained bed of each couplet has distinctly bimodal grain-size distribution, with peaks in the clay and sand ranges whereas the finer-grained bed of each couplet has
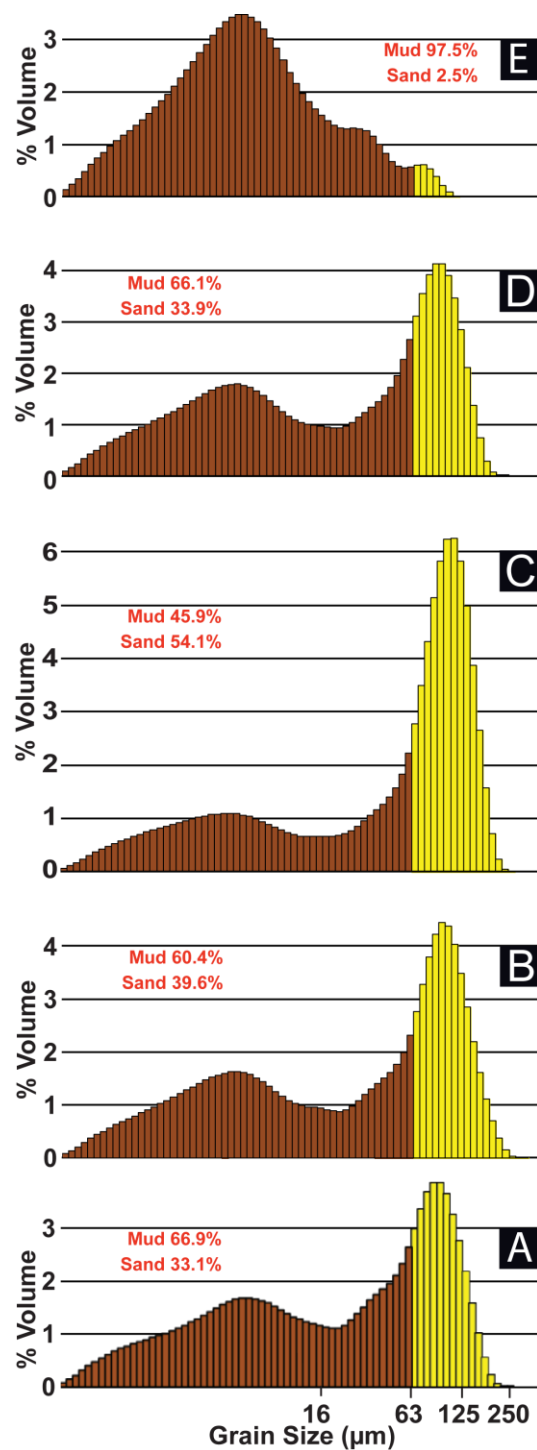
Figure 14. Representative grain-size distribution from the base (A) to the top (E) of one couplet (T6; photo shown in F 6). The coarse-grained bed (A-D) shows a distinct bimodal distribution; the fine-grained bed (E) is generally more unimodal. Grain size coarsens up from the base to ~midpoint of couplet and then fines up.

Table 5. Segment averages of grain size analysis for each contiguous segment (comprised of 3 couplets each), total for all 3 segments, and the segments to the left and right of M1-3. (µm is micrometers)

Segment Averages	Mud <63 µm	Sand >63µm	Mean (µm)
T5-7	66.6%	33.4%	46.8
M1-3	69.4%	30.6%	42.2
C2-4	70.8%	29.2%	41.3
ALL	**69.0%**	**31.0%**	**43.4**
ML1-3	73.5%	26.5%	35.9
MR1-3	74.9%	25.1%	36.0

roughly unimodal distribution with a peak in the clay range (F 14). A slight increase in the mean grain size up-section (from couplets C2-4 to T5-7) is apparent from Table 5.

To test for lateral variability in grain-size distribution within couplets, analysis was also conducted on samples ~4 m to the left (segment ML) and ~4 m to the right (segment MR) of contiguous couplets M1-3 (Table 5; Appendix E). Standard principal component analysis was applied to compare the variability of grain-size distribution of the samples from the lateral (ML and MR) and primary (M) locations using five grain sizes: clay, silt, very fine-, fine-, and medium-sand (F 15). The first two principal components (PCs) explain 99.4% of the variance (PC1 explains 96.3%). Samples within and bordering the fine-grained interval (e.g., M1-1,7,8 and ML-2,4,6; also see F 7) cluster in the negative quadrants of PC1; samples within the coarse-grained interval (e.g., M1-2,3,4,5 and ML-1,3,5) cluster in the positive quadrants of PC1. This distribution demonstrates that the vertical grain-size trend is not significantly different when moving laterally along a couplet.
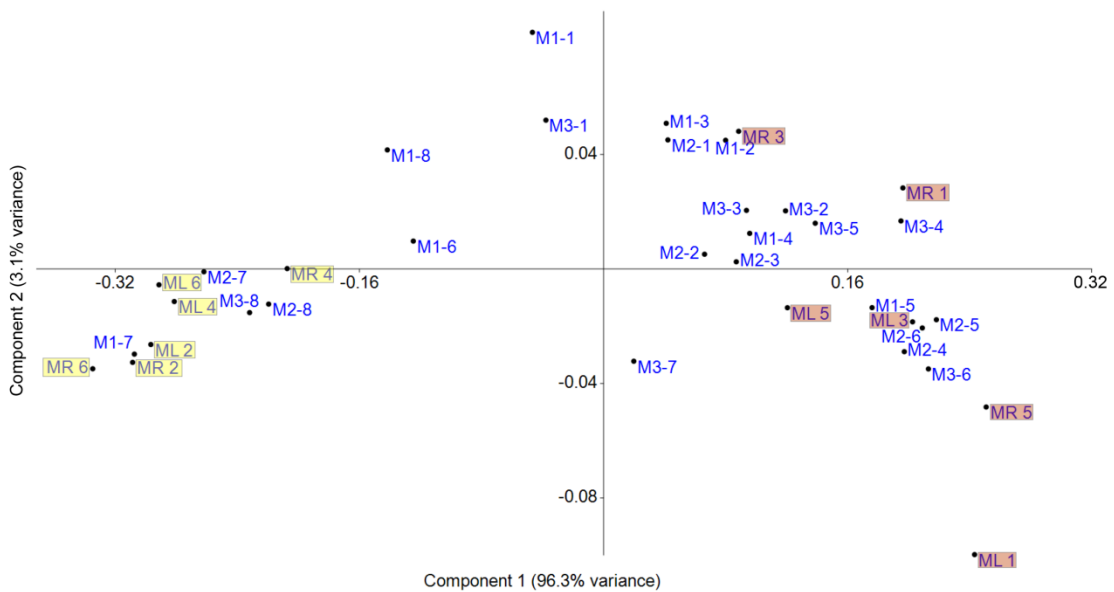
Figure 15. Principal component analysis plot of grain-size variability from lateral (ML and MR) and primary (M) samples of couplets M1,2, and 3. Samples plotting in the negative quadrants of PC1, including the lateral samples highlighted in yellow, are from within or adjacent to the fine-grained interval of each couplet. Samples plotting in the positive quadrants of PC1, including the lateral samples highlighted in red, are from the coarse-grained intervals.

X-ray Diffraction Analysis

X-ray diffraction analysis performed on specimens obtained from the same samples collected for grain size analysis helped identify vertical variations in proportions of key mineral phases within couplets (Appendix F). Average weight (wt.) proportions of key phases include: 49% quartz, 14% plagioclase, 13% potassium feldspar, 13% clay and micas, 7% calcite, 3% gypsum, and 2% dolomite (Table 6). Vertical variations within each couplet reveal first an increase in wt. % quartz, then a decrease, with the clay/mica group inversely related (F 16). Plagioclase and potassium feldspar phases maintain relatively uniform proportions throughout. Changes in calcite and the clay / mica group appear directly related.

Lateral variability in mineral phases was also tested using samples from segments to the left (ML1-3) and right (MR1-3) of couplets M1-3 (Table 6; Appendix F). Standard principal component analysis was applied to compare the variability of mineral composition of the samples from the lateral (ML and MR) and primary (M) locations using seven categories: quartz, potassium feldspar, plagioclase, clay /mica, calcite,

Table 6. Segment averages of XRD analysis for each contiguous segment (comprised of 3 couplets each), total for all 3 segments, and the segments to the left and right of M1-3.

Sample	Quartz (%)	Potassium Feldspar (%)	Plagioclase (%)	Clay & Micas (%)	Calcite (%)	Dolomite (%)	Gypsum (%)
T5-7	49.0	13.1	14.1	12.8	5.8	2.1	3.1
M1-3	49.2	13.0	13.4	13.0	6.8	2.0	2.7
C2-4	49.4	13.0	14.1	12.3	6.8	1.9	2.6
ALL	49.2	13.0	13.9	12.7	6.5	2.0	2.8
ML1-3	47.1	12.7	13.6	15.1	6.4	2.4	2.7
MR1-3	45.6	12.3	13.0	17.0	8.2	2.3	1.6
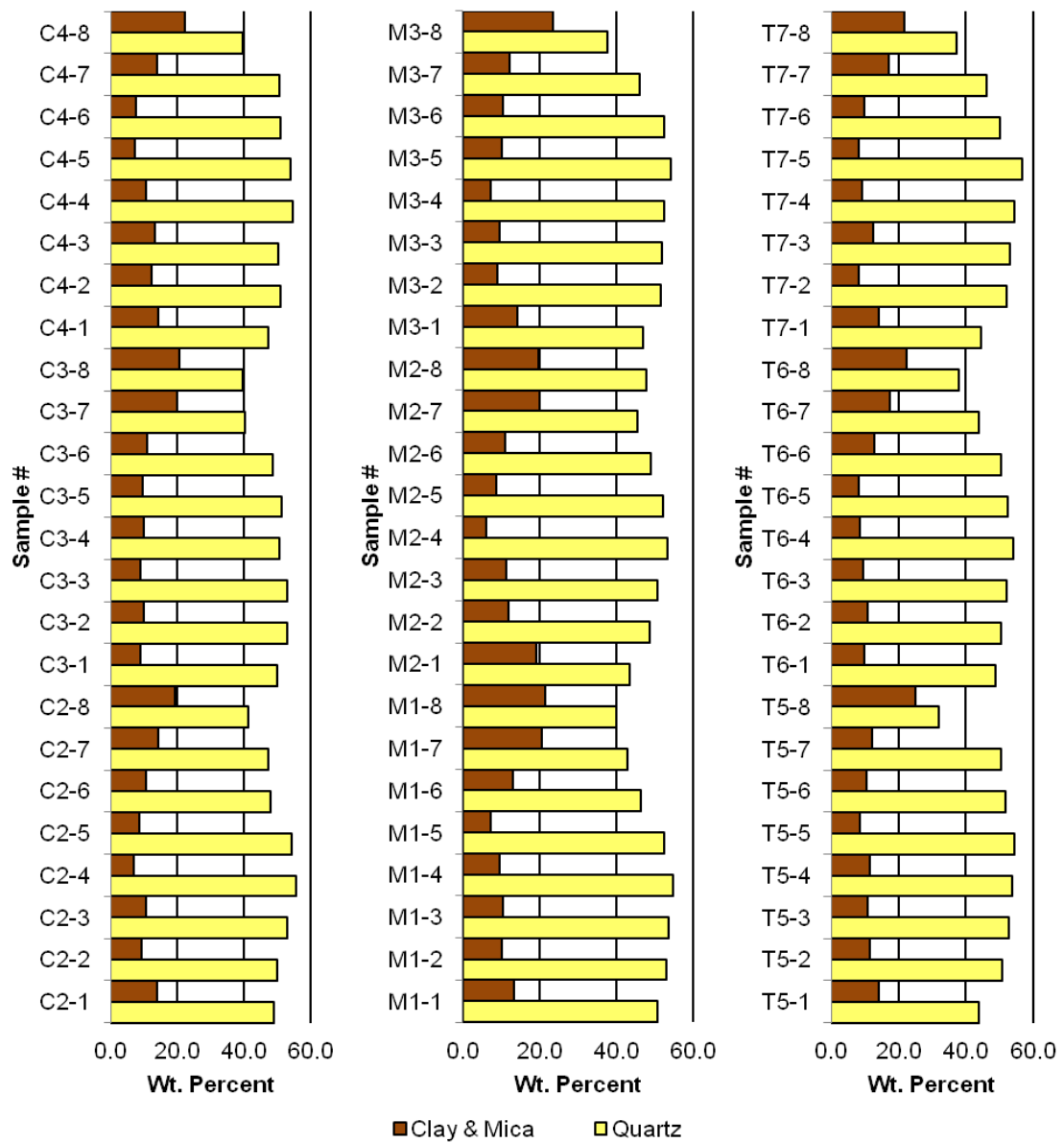
Figure 16. XRD analysis results of 3 sets of contiguous couplets (C2-4, M1-3, T5-7). Graphs reflect first the increase followed by the decrease in quartz content (yellow bars) within each couplet. For example, Couplet C2 is comprised of samples C2-1 to C2-8, and quartz increases from ~49% at the base of the couplet (sample C2-1), to ~56% at the midpoint (sample C2-4) and decreases to ~41% at the top of the couplet (sample C2-8). The clay and mica group (brown bars) shows an inverse trend to quartz.

43

dolomite, and gypsum (F 17). The first two principal components (PCs) explain 94.5%

of the variance (PC1 explains 88.3%). Samples from within and bordering the fine-

grained interval (e.g., M2-1,7,8 and ML-2,4,6; also see F 7) cluster in the negative

quadrants of PC1; samples within the coarse-grained interval (e.g., M2-2,3,4,5,6 and

ML-1,3,5) cluster in the positive quadrants of PC1. The negative quadrants are likely

explained by an abundance of clay/micas (and corresponding deficiency of quartz)

whereas the positive quadrants reflect an abundance of quartz (deficiency in clay/micas).

This distribution demonstrates that vertical variations in mineralogical composition are

not significantly different when moving laterally along a couplet.

Interpretation: Grain Size Linked to Mineral Phase

The vertical variation of quartz in each couplet (increase in wt. % quartz followed

by a decrease) mirrors the trend of % sand (F 18). The link between quartz content and

grain-size variation suggests the coarser fraction in the couplets is dominated by quartz

granules. Conversely, the similar vertical trend within couplet between % clay/mica and

% mud may indicate the mud fraction is comprised largely of clays and micas. Finally,

the silt fraction and feldspars (plagioclase and potassium feldspar combined) maintain

relatively uniform percentages throughout both portions of each couplet, possibly

indicating the silt fraction is dominated by the feldspar group.
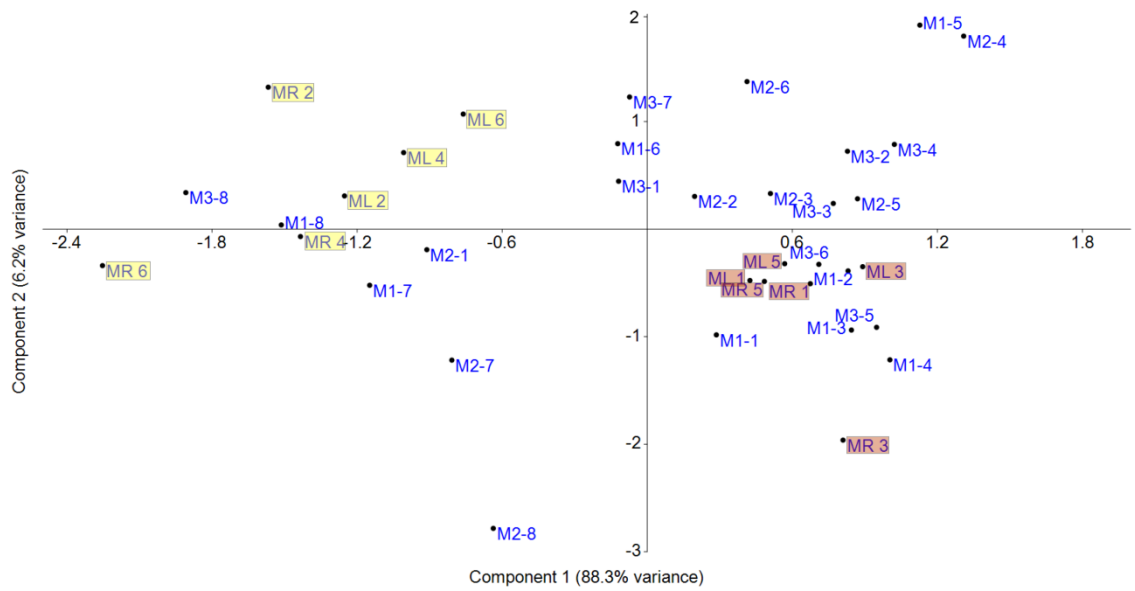
Figure 17. Principal component analysis of mineral phases of lateral (ML and MR) and primary (M) samples of couplets M1, 2, and 3. Samples plotting in the negative quadrants of PC1, including the lateral samples highlighted in yellow, are from within or adjacent to the fine-grained intervals of the couplet. Samples plotting in the positive quadrants of PC1, including the lateral samples highlighted in red, are from the coarse-grained intervals.
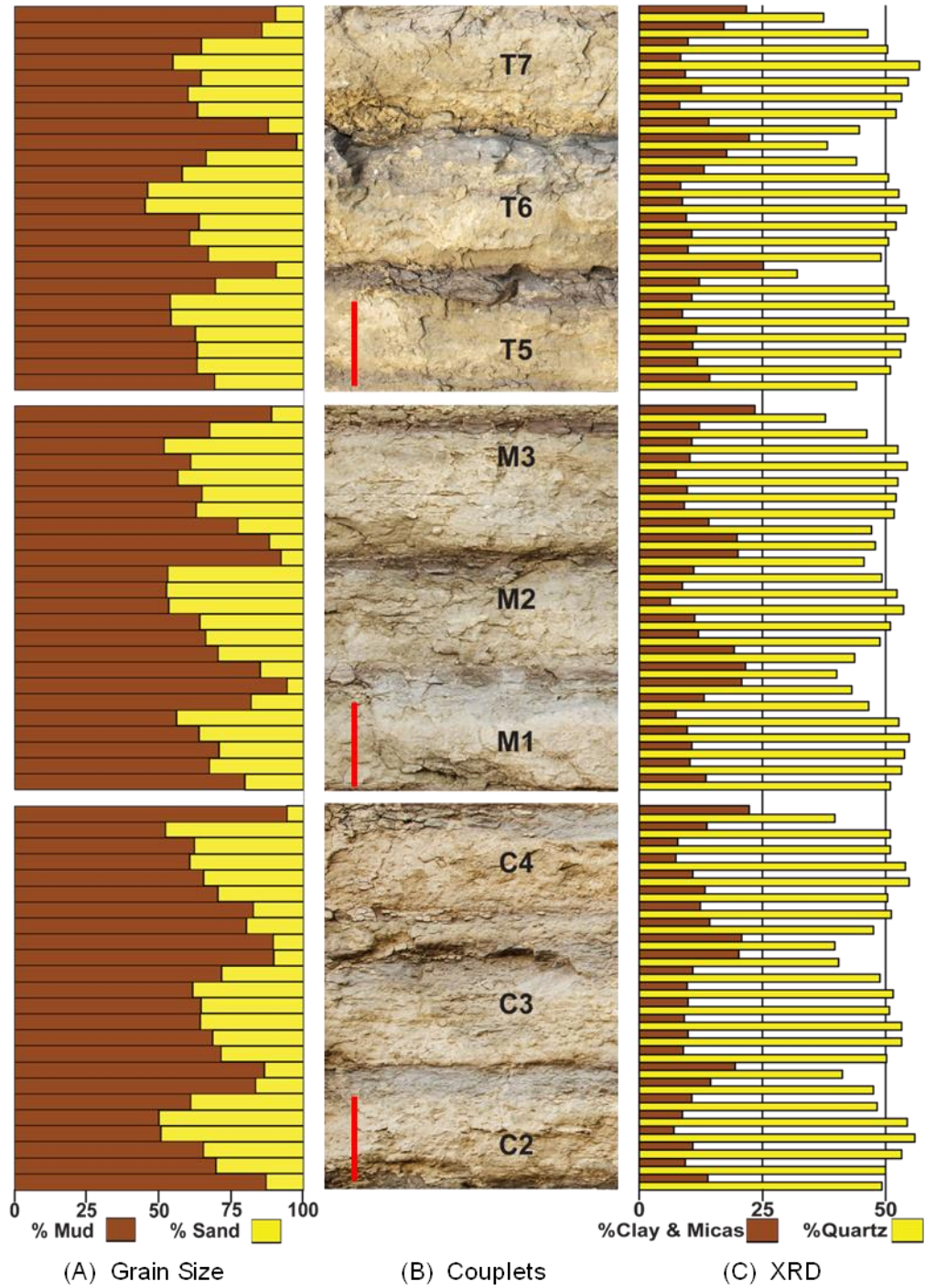
Figure 18. Visual linkage of grain size (A) and mineral phase (C) alongside image of sampled couplets (B). Note parallel trends in compositional and grain-size variations and the clear expression of inverse grading followed by a, sometimes abrupt, change to normal grading in each couplet (A). Red bars in (B) are 10 cm.

Time Series Analysis

Bed Thickness

Time series analysis of bed thickness of the coarse interval of 265 couplets (~33 m) within section FC6-2 consistently obtained a prominent spectral peak using different time series analysis methods (Fast Fourier Transform (FFT), Multitaper, and Redfit) at a frequency of ~ 0.054 cycles/couplet, corresponding to a periodicity of about 18 couplets (F 19). This result is strengthened, not only by its consistent appearance above 95% confidence levels using different algorithms, but also by the fact that time series analyses performed on thickness of coarse beds in FC6-3 and thickness of 445 consecutive beds (~22 m) in FC6-1 did not yield any significant spectral peak. Therefore, only section FC6-2 appears to be characterized by a distinct periodicity in bed thickness.

Grayscale Intensity

Time series analysis of image brightness values of a composite photographic log converted to grayscale covering a subset of 159 consecutive couplets (~22 m; Segments A-U) was performed using the FFT algorithm yielding a power spectrum (F 20; Appendix G). Prominent spectral peaks cluster at different frequencies. The first cluster, with frequencies between 11-16 cm, corresponds to the rhythmicity of the couplets, which in this portion of section FC6-2 have an average thickness of ~14 cm. A second cluster at lower frequencies (between 0.6 and 1.5 m) could represent periodicities involving multiple couplets or a spurious signal introduced by the stitching of different segments to create the composite photolog.
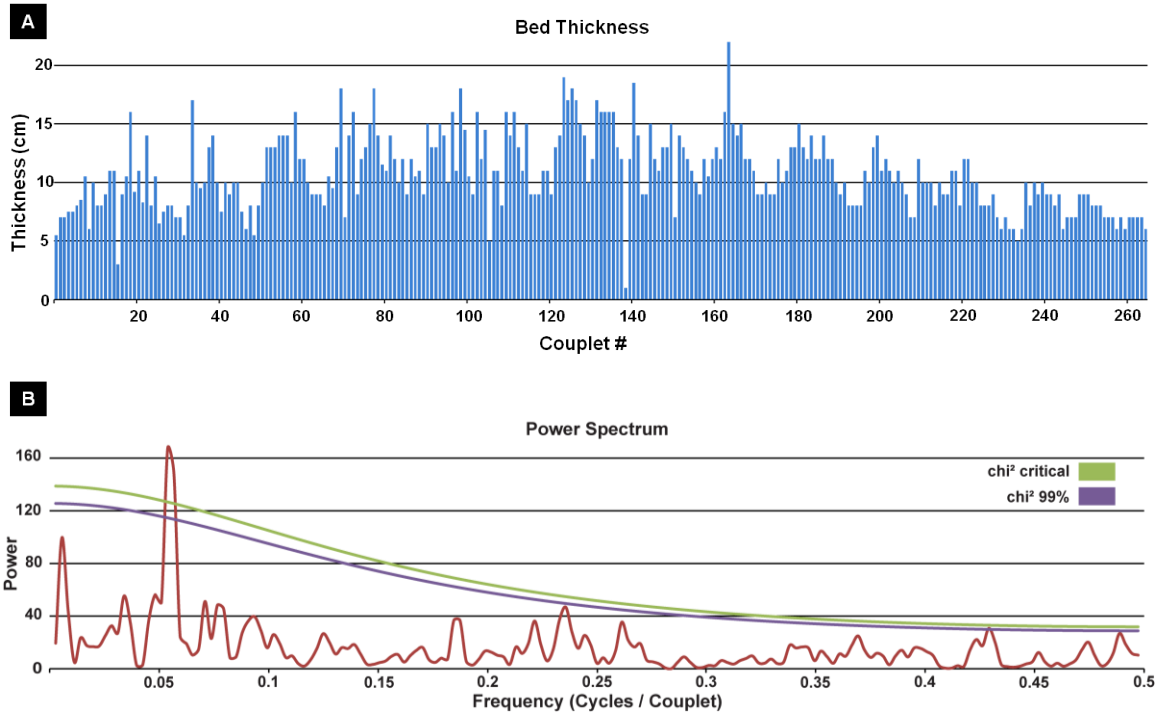
Figure 19. Time series analysis power spectrum compared to plot of bed thickness. (A) Plot of coarse-grained bed thickness per couplet number, used for the time series analysis. (B) Representative power spectrum of bed thickness series in (A), showing prominent peak above critical and 99% chi^2 confidence levels calculated fitting the series to an AR(1) red noise model.
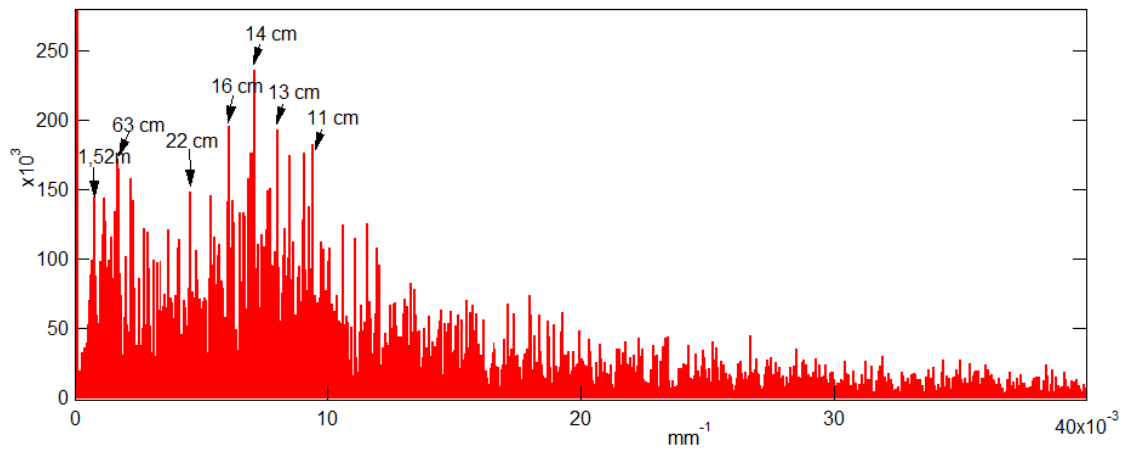
Figure 20. Time series analysis power spectrum of the composite grayscale intensity log of FC6-2 (segments A-U) obtained with a FFT analysis.

CHAPTER FIVE

DISCUSSION

Mode of Deposition of the Mud Hills Member Rhythmites

Cumulative sedimentological evidence of the rhythmite section (FC6-2), including laterally continuous mudstone-siltstone couplets with gradational to sharp contacts, internal scours, planar-parallel, wavy, and ripple cross-lamination, and the distinctive grain-size variation producing inverse to normal grading within each couplet, suggests deposition via hyperpycnal sediment gravity flow (Bhattacharya and MacEachern, 2009; Mulder et al., 2003; Mutti, 2003; Soyinka and Slatt, 2008; Wilson and Schieber, 2014). Frequent occurrence of a massive interval overlain by planar-parallel laminae within the coarse-grained portion of many couplets may reflect a transition from higher sediment concentrations (which suppress turbulence and the construction of laminae) to lower concentrations (Lamb et al., 2010; Middleton, 1967). Reductions in sediment concentration occur as a result of deposition or gradual entrainment of seawater as the hyperpycnal flow progresses (Mulder and Syvitski, 1995). The pattern of inverse grading followed by normal grading within each couplet reflects the waxing then waning energy and competence distinctive to the classical suspended-load-dominated hyperpycnites deposited by quasi-steady, river-flood-generated hyperpycnal flows *sensu* Mulder et al. (2003) and Mulder and Chapron (2011). Waxing flow can also generate the intra-couplet scours, which are commonly filled with cross-laminae (Nakajima, 2006).

Several lines of evidence seem to indicate that time between deposition of individual hyperpycnites was not too prolonged. There was sufficient time for moderate

to sometimes significant bioturbation to take place but not for complete homogenization of the couplets. Positive statistical correlation between the thicknesses of the coarse-grained and overlying fine-grained portion of each couplet and their consistent internal grain-size distribution strongly suggest the two portions correspond to distinct, but related, phases of a single hyperpycnal flow. This conclusion implies the lack of significant non-hyperpycnal background sedimentation in the measured interval, pointing to either non-deposition due to low sediment input or hindrance of sedimentation by tidal or wave effects, sediment bypass (Stevenson et al., 2015), or relatively little time between hyperpycnal flows.

Furthermore, erosion of the fine-grained layer by the next hyperpycnal flow appears to have been minimal, as demonstrated by the predominance of gradational bases and the statistical correlation in bed thickness between the coarse- and fine-grained portion of each couplet. This finding suggests that the abundant clay particles and larger peloids occurring in the silt- to very fine sand-dominated interval of the couplets most likely flocculated and were entrained from mud suspensions during the original flow (Bhattacharya and MacEachern, 2009; Plint, 2014).

Environment of Deposition of the Mud Hills Member

The prodeltaic nature of the Mud Hills Member has been well established based on the larger stratigraphic context of the FCV basin infill, which shows a progradational marine to continental succession culminating with alluvial deposits of the Arroyo Diablo Fm. (F 2) (Dorsey et al., 2011; Winker, 1987; Winker and Kidwell, 1996). However, as

demonstrated in the present study and already noted by Winker (1987), the Mud Hills Member shows significant internal lithological variability.

Directly beneath the rhythmites stratigraphically (F 4C), section FC6-1 seems indicative of a mixed-influenced, distal prodelta setting with interaction of river, tidal, and rare wave processes. Abundant planar-parallel lamination, ripple cross-lamination, and occasional soft-sediment deformation are typical of river-dominated deltaic environments (Bhattacharya and MacEachern, 2009; Bohacs et al., 2014; MacEachern and Bann, 2008). Prevalent in FC6-1, heterolithic lamination is most commonly described in tide-dominated deltas, occurring less frequently in river-dominated ones (Bhattacharya, 2006; Bohacs et al., 2014). Occasional wave ripples indicate an oscillatory component likely a result of wind-generated waves. The uppermost portion of section FC6-1, immediately below the first rhythmite of FC6-2 and comprised of ~7 m of homogeneous clay-rich mudstone, may represent a period of reduced or discontinued clastic input dominated by background sedimentation of wave- or tidal-redistributed fines (Schieber, 2016).

The first hyperpycnite of the primary rhythmite section, FC6-2, distinctly marks a transition to a renewed and sustained influx of clastics and a transition from the distal, mixed-influenced prodelta to a river-flood-dominated, proximal prodelta environment. Flood-related facies are prevalent and have excellent preservation potential in prodelta environments (Li et al., 2015; Mulder and Chapron, 2011; Mulder and Syvitski, 1995; Mutti et al., 1996). The confined nature of the Colorado River deltaic setting within the narrow, elongate embayment of Pliocene times would have minimized lateral dispersion of hyperpycnal flows, promoting longer runouts to prodelta depths with thicker deposits

and increasing the preservation potential of the flood hydrograph (Lamb et al., 2010; Mulder and Chapron, 2011).

Cyclical Forcing Mechanisms

Our time series results appear to confirm the existence of a cyclical mechanism affecting the expression of hyperpycnites recorded in the primary section (FC6-2) of the prodeltaic MHM rhythmites. Identification of the mechanism largely depends on assigning a time duration for the individual 18-couplet cycle revealed in bed thickness analysis. Magnetostratigraphic constraints (Dorsey et al., 2007; Dorsey et al., 2011) (F 2) based on data from our study site (samples 04PM71, 04PM32, 04PM72, and 04PM35[1]) indicate that the ~46 m-thick interval, comprising sections FC6-2 and FC6-3 of the MHM rhythmites, was deposited during magnetic polarity Subchron C3n.2r and records the transition between magnetic polarity Subchrons C3n.3n and C3n.2n in its lower and upper part, respectively. This results in an estimated interval of time for deposition of the rhythmites of ~200 k.y.

Among Milankovitch-type astronomical controls commonly recognized as causes for sedimentary cyclicity, the precessional cycle is the only one generating high enough frequencies (1 cycle per ~19-24 k.y.) (Hinnov, 2013) to be reliably detectable in an ~200 k.y.-long interval. However, invoking it to explain the 18-couplet cyclicity would result in the unrealistic scenario of ~200 k.y. of sustained prodeltaic depositional conditions characterized by ~1 hyperpycnal flood, and not much sedimentation, every 1 k.y. On the

---

[1] GSA Data Repository item 2010211, Table DR1 (GPS locations, thicknesses, polarity determinations, and data quality for all paleomagnetic samples), available online at www.geosociety .org/pubs/ft2010.htm, or on request from editing@ geosociety.org or Documents Secretary, GSA, P.O. Box 9140, Boulder, CO 80301, USA.

other hand, invoking daily or monthly tidal rhythms to explain the cyclicity would result in sedimentation rates orders of magnitude higher than the average calculated from magnetostratigraphy. The most likely mechanism, therefore, is probably a seasonal to decadal control, in the same frequency as monsoonal, El Niño, or the 18.6 year lunar nodal cycles.

Lunar Nodal Cycle

The moon's orbit is inclined about 5º from Earth's ecliptic resulting in an 18.6 year-precession of the lunar nodes (points where the moon's orbit intersects the ecliptic) (de Boer and Alexandre, 2012). During this cycle the inclination of the moon's orbit relative to Earth's equator varies from 18º to 28º, consequently modulating mid-latitude tidal amplitudes by ~5% and, subsequently, tidal velocity and sediment transport capacity (de Boer and Alexandre, 2012; Mazumder and Arima, 2005). Miller and Eriksson (1997) identified prodeltaic rhythmite bundles, comprised of 17-22 annual beds that thickened then thinned upward, and interpreted the pattern as an overprint of the lunar nodal cycle upon annual sets of tidal rhythmites. They theorized that the thickest beds correspond to the maximum tidal amplitude (sediment transport capacity) during the highest (28º) inclination (Miller and Eriksson, 1997).

Tidal amplitude variations due to ebb/flood and neap/spring tides are known to precipitate salinity changes in deltaic environments (Harris et al., 2004; MacEachern and Bann, 2008; McIlroy, 2006). Initiation of hyperpycnal flow hinges on a density contrast between the freshwater effluent and seawater, which is determined by the relative riverine suspended-sediment load and seawater salinity at the river mouth (Mulder et al.,

2003). Wang et al. (2010) documented the modulation of hyperpycnal flows by tides during the flood season in the Huanghe (Yellow River) mouth, China. During ebb tides, characterized by high sediment concentrations and reduced salinity, hyperpycnal flows were strongest, transporting ~10 times as much sediment to the sea as during the higher-salinity, flood tides (Wang et al., 2010).

The lower section, FC6-1, interpreted as a distal prodelta, appears to document a tidal influence which may have continued to the proximal prodelta environment of the primary rhythmite section. Though neither typical tidal beds nor structures are found in FC6-2, exceptional tidal amplitudes, such as documented during the maximum inclination of the lunar nodal cycle (de Boer and Alexandre, 2012; Mazumder and Arima, 2005), may have influenced the expression of the MHM hyperpycnites via changes in salinity. High-amplitude tides, generated by the lunar nodal cycle, may have increased water salinity near the river mouth, lowering the density contrast and resulting in a diminished hyperpycnal flow and thickness of subsequently deposited hyperpycnites. If the lunar nodal cycle modulated hyperpycnal flow in the early Colorado River delta, the record may be preserved in the MHM hyperpycnites, which show an upward thickening then thinning cycle over 18 couplets. This explanation for an 18-couplet cycle implies a depositional rate of ~1 couplet per year. Despite the appealing cyclic comparison, the lunar nodal cycle is noted as having a relatively weak effect on tidal elements and the signal is rarely preserved in ancient sedimentary environments (de Boer and Alexandre, 2012; Mazumder and Arima, 2005; Miller and Eriksson, 1997).

North American Monsoon

The North American monsoon (NAM) is an annual, warm-season reversal of atmospheric circulation due to land/sea temperature disparities that generates a pronounced increase in precipitation from mid-June through mid-October over northwestern Mexico and southwestern United States (SW USA), including the Colorado River watershed (Bordoni et al., 2004; Hereford et al., 2002). Late Miocene intensification of the NAM resulted from the tectonic opening of the Gulf of California, which established an ~1100 km fetch over very warm waters and greatly increased advection of water vapor (Chapin, 2008). Not only is the Gulf of California the dominant moisture source of NAM rains, with secondary eastern tropical Pacific and Gulf of Mexico contributions, but the warm-season, southerly gulf wind pattern, coincident with the NAM season, is the primary transport mechanism of moisture to the SW USA (Bordoni et al., 2004; Chapin, 2008; Hereford et al., 2002).

It is hypothesized that late Miocene NAM thunderstorms contributed significantly to erosion in the Southern Rocky Mountains and eventually to the integration of the Colorado River with the Gulf of California (Chapin, 2008). Tropical cyclones associated with the NAM season have reported frequencies of 15-17 occurrences per year in recent times, though only ~80% of them contribute significant rains to the Colorado Plateau region (Apostoli et al., 2016; Romero-Vadillo et al., 2007; Schultz, 2008). Additionally, during strong El Niño climate patterns (discussed below), the average number of tropical cyclones increases to 18.6 per year (Schultz, 2008). No cyclical mechanism modulating monsoonal storm intensity is known, however, precipitation frequency during seasonal monsoons on the Colorado Plateau has been studied using data from 1897 to 1986

(Hereford and Webb, 1992). It was found that precipitation gradually increases beginning in June, peaking for a few weeks at the end of July to beginning of August, and decreasing, at first sharply and then more gradually, to mid-October (Hereford and Webb, 1992). This variability of intraseasonal precipitation could potentially produce a series of flows with strengths that mimic the cycle and corresponding deposits that are thinner at the beginning and end of the season and thicker in the middle. Though Pliocene frequencies of the occurrence or intensity of NAM-associated tropical cyclones is unknown, it seems theoretically possible, based on the modern day occurrence of tropical storms and subsequent intraseasonal precipitation cycle, that the 18-couplet rhythm of the MHM hyperpycnites could have been controlled by the seasonal NAM.

El Niño

The El Niño/Southern Oscillation climate pattern produced by the interaction of variations in sea surface temperatures and atmospheric pressure alternates between warm (El Niño), cool (La Niña) and transient phases (Hereford et al., 2002). El Niño, in response to warming eastern tropical Pacific waters, is associated with a higher frequency of significant (category 3, 4, or 5) long-lived tropical cyclones, as well as widespread, cool-season precipitation in the SW USA (Chapin, 2008; D'Arrigo and Jacoby, 1991; Hereford et al., 2002; Peryam, 2012; Romero-Vadillo et al., 2007). The preponderance of studies show El Niño-like conditions were sustained, or "permanent", throughout the early to mid-Pliocene, producing abundant cool-season rains in the SW USA (Barreiro et al., 2006; Bonham et al., 2009; Fedorov et al., 2006; Molnar and Cane, 2002; Smith and Patterson, 1994; Wara et al., 2005).

During the early Pliocene, a sustained El Niño, periodically in phase with the annual NAM cycles, likely resulted in substantially increased frequency of tropical storms and subsequent warm-season precipitation in the SW USA (Chapin, 2008; Molnar and Cane, 2002; Peryam, 2012; Schultz, 2008). The combined effects of the persistent winter-season El Niño and the El Niño-enhanced summer-season NAM, resulting in more frequent, intense precipitation, flooding, and erosion in the Colorado River watershed, may have served as a primary control on subsequent sedimentation in the FCV basin. The inter- or intra-seasonal periodicity, if any, associated with this complex, climatically-intense time has yet to be studied. We can speculate that a series of "permanent" El Niño-enhanced NAM seasons, exhibiting modern frequencies of tropical cyclone occurrence (~18.6 per year; Schultz (2008)) and subsequent intraseasonal cyclicity of precipitation (rising then falling rates with mid-season peaks; Hereford and Webb (1992)), could have influenced the expression of the MHM hyperpycnites. At the very least, the wet, early Pliocene climate provided the means for generating hyperpycnal flows, which were then modulated by some other mechanism such as the lunar nodal cycle.

Advance of the Lower Colorado River Via Lake 'Fill and Spill' and Implications for the MHM Rhythmites

While it appears climate exerted some control on MHM deposition, it is possible that another mechanism, perhaps in combination with climatic events, contributed to the regular stratigraphic signal. In their spatial analysis of the MHM rhythmites, Lynch and Adams (2009) outline a theoretical aperiodic process for the formation of rhythmic

bedding involving the occasional over-spilling of a closed, ponded basin after heavy rains. Assuming a flow velocity that neither deposits nor erodes, the current diminishes after the basin waters fall below dam level, dropping its fixed load and producing beds of ~uniform thickness (Lynch and Adams, 2009). Though Lynch and Adams (2009) admit their study makes no inference regarding depositional time intervals of the MHM rhythmites, nor whether deposition was periodic or aperiodic, their model, based on over-spilling of an upstream closed basin, provides another element to interpret the cyclicity observed in this study.

The lake 'fill and spill' model for the extension of the lower Colorado River from Grand Canyon to the Gulf of California, first proposed by Newberry (1861), has increasingly gained support following stratigraphic, tectonic, microfaunal, detrital zircon, and stable isotope studies (Blackwelder, 1934; Bright et al., 2016; Cloos, 2014; Dorsey, 2010; Dorsey et al., 2007; House et al., 2005; House et al., 2008; Howard et al., 2014; Kimbrough et al., 2011; Meek and Douglass, 2001; Roskowski et al., 2010). It is hypothesized that in the late Miocene the Colorado River overtopped the first, in a series of five, paleodams flooding the basin beyond (the Black paleodam and Cottonwood basin; see F 3) and establishing an elongate, short-lived lake just south of the modern Hoover Dam area (House et al., 2008). This process repeated thrice more, overtopping the Pyramid, Topock and Aubrey paleodams and filling the Mohave, Chemehuevi and Blythe basins, respectively. The final natural barrier (Chocolate paleodam) between the Colorado River and the Gulf of California contained the large paleo-lake Blythe, which may have overspilled the dam repeatedly prior to its final disintegration (Homan, 2015; House et al., 2008). Citing a distinctive clay layer as evidence of re-deposited lake fines,

Bright et al. (2016) argue for an initial catastrophic dam breach, partial draining of paleo-lake Blythe, and the establishment of a through-going Colorado River. Homan (2015) described a previously unrecognized limestone unit that overlies Colorado River channel deposits and hypothesized that after an initial drawdown of the lake, a tectonically-controlled paleodam was re-established and the basin refilled.

After the initial breakthrough of the Chocolate dam, establishment of a through-going Colorado River, and a subsequent re-damming and refilling of the lake basin, many partial spillovers of the residual paleo-lake Blythe could have been triggered by seasonal rainfalls, similar to the model of Lynch and Adams (2009). However, instead of aperiodic deposition, as in their model (Lynch and Adams, 2009), the spillovers could have been periodically controlled by ongoing El Niño-enhanced NAM seasons, or the subsequent hyperpycnal flows could have been modulated by the lunar nodal cycle, either control producing the 18-couplet rhythmicity discerned in the MHM hyperpycnites. Alternatively, the final demise of the Chocolate paleodam and draining of paleo-lake Blythe could have preceded deposition of the MHM hyperpycnites, which instead reflect a record of through-going Colorado River flood events likely induced by El Niño-enhanced NAM seasons.

Timing of the initial and final, hypothesized Chocolate paleodam failures has implications for controls on deposition of the MHM rhythmites. The southern-most Blythe basin deposits (Bouse Fm.) record the initiation of the paleo-lake around 5.6-5.3 Ma, the arrival of Colorado River fines followed by channelized sandstones between 5.3-5.1 Ma, and the re-flooding of the basin between 5.1-4.8 Ma (Homan, 2015; House et al., 2008; Howard et al., 2014). Re-filling of Blythe basin coincides with the timing of an

hypothesized hiatus from Colorado River deposition in the Salton Trough (Dorsey et al., 2011). After ~4.8 Ma, paleo-lake Blythe deposition ceased (Homan, 2015; Spencer et al., 2013) and an unrestricted through-going Colorado River is re-established, coinciding with the paleomagnetically-dated first appearance of the MHM rhythmites (Dorsey et al., 2007; Dorsey et al., 2011).

Both the gradual overtopping of a dam and long-lived climatic events, such as seasonal monsoons, generate floods that favor suspended-load transport capable of producing hyperpycnal flows, lasting days to months, upon entering the marine delta environment (Mulder and Chapron, 2011; Mulder et al., 2003). The MHM hyperpycnites preserve a record of gradually waxing then waning flow of suspended-load-dominated flood events making a compelling argument for either numerous, gradual overflows of the Chocolate paleodam or repeated El Niño-enhanced NAM-induced flooding of the fully established Colorado River. Both scenarios can result in the deposition of a classical hyperpycnite (Mulder et al., 2003). However, the latter hypothesis seems more likely given that the current chronostratigraphic data from the Bouse Fm. indicate final drainage of paleo-lake Blythe likely preceded deposition of the MHM rhythmites.

Depositional Model of the Mud Hills Member Rhythmites

We here interpret the MHM rhythmites as deposited, episodically and rapidly, via hyperpycnal flows in the early Pliocene Colorado River prodelta, each couplet most likely representing sustained individual river-flood events with internal variations in flow intensity. The frequency of hyperpycnal flows of "dirty rivers" (high suspended-sediment loads) can range from annual to "semi-continuous", occurring during every

flood (Mulder and Syvitski, 1995; Nakajima, 2006; Parsons et al., 2001). It is well-documented that the early Pliocene Colorado River carried a voluminous sediment load from the Colorado Plateau region (Dorsey and Lazear, 2013; House et al., 2008; Howard et al., 2014; Johnson et al., 1983; Winker, 1987), and it likely qualified as a "dirty river" capable of frequent hyperpycnal flows. The Pliocene amalgamation of the NAM and El Niño climatic phenomena likely increased erosion and contributed to the high-suspended sediment load and discharge of the Colorado River.

The 18-couplet cyclicity discerned in the MHM hyperpycnites may have been controlled by the El Niño-enhanced NAM interseasonal (tropical storm frequency) and intraseasonal (periodicity of rainfall amounts) patterns. Alternatively, the strength of hyperpycnal flows may have been modulated by the effects of the lunar nodal cycle on tidal amplitudes and consequently salinity concentrations at the river mouth. Whether either of these mechanisms generated the 18-couplet cyclicity remains uncertain.

Based on prior studies of the timing and events surrounding the progression of the lower Colorado River to the Gulf of California (Bright et al., 2016; Dorsey et al., 2011; Homan, 2015; House et al., 2008; Howard et al., 2014) and the results of this study we surmise the following scenario:

1. During the interval of time (5.1-4.8 Ma) when the Blythe basin was re-flooding, the Colorado River was still through-going, but with discharge reduced and sediment load mostly trapped within the basin. This reduced-energy flow would have been easily influenced by tide and wave forces and may have resulted in the heterolithic deposits of the mixed influence, distal prodelta unit of section FC6-1, stratigraphically below the primary rhythmite section (F 4C).

2. The final draining of paleo-lake Blythe (~4.8Ma), the details of which are unknown, may have resulted in the deposition of the ~7 m-thick homogeneous clay-rich mudstone between the heterolithic deposits of section FC6-1 and the first rhythmite at the base of section FC6-2 (F 4C).

3. After the final demise of the paleo-lake, the fully established Colorado River, with high energy and suspended-sediment load, flowed directly into the Gulf of California. The voluminous sediment load triggered the flow to plunge forming a hyperpycnal flow and commencing deposition of the MHM hyperpycnites, effecting the transition from distal, mixed-influence to river-flood-dominated prodeltaic environment.

CHAPTER SIX

CONCLUSIONS AND FUTURE RESEARCH

This study combined high-resolution logging and grain-size, thin section, and XRD analyses to ascertain the mode and environment of deposition of the Pliocene Mud Hills Member rhythmites. Additionally, time series analyses of bed thickness and image grayscale intensity were performed to determine if deposition was modulated by cyclical forces. Finally, a review of previous literature on the progression of the lower Colorado River to the Gulf of California facilitated reconstruction of the timing and events surrounding deposition of the Mud Hills Member. The conclusions of this study are summarized below.

1) The cumulative sedimentological evidence of the rhythmites, including laterally continuous mudstone-siltstone couplets with gradational to sharp contacts, internal scours, planar-parallel, wavy, and ripple cross-lamination, and the distinctive grain-size variation producing inverse to normal grading within each couplet, coupled with the general stratigraphic context of a prodeltaic succession, indicates deposition via river-flood-generated, suspended-load-dominated hyperpycnal sediment gravity flows.

2) The positive statistical correlation between the thicknesses of the coarse-grained and overlying fine-grained portion of each couplet, the consistent internal grain-size distribution, and predominance of gradational contacts strongly suggest the two portions correspond to distinct, but related, phases of a single hyperpycnal flow with minimal erosion by the subsequent flow. This conclusion implies the lack of significant background sedimentation in the measured interval, pointing to either non-deposition, sediment bypass, or relatively little time between hyperpycnal flows.

3) Thin section analysis revealed intermittent to significant bioturbation, though not enough to homogenize the couplets, suggesting fluctuation of deposition rates or environmental stressors (e.g., salinity or temperature).

4) XRD analysis revealed vertical variations within each couplet characterized by first an increase in wt. % of quartz, then a decrease, with the clay/mica group inversely related. Vertical variation of quartz in each couplet mirrors the trend of % sand suggesting the coarser fraction in the couplets is dominated by quartz. A similar vertical trend within couplet between the clay/mica group and % mud indicates the mud fraction is comprised largely of clays and micas. Segregation of different mineral phases in distinct portions of a couplet is interpreted as the result of differences in hydraulic behavior, due to density and grain-size variation, during the waxing and waning of the flow.

5) Time series analysis of rhythmite bed thickness consistently obtained a prominent spectral peak corresponding to a periodicity of ~18 couplets. Among Milankovitch, lunar, climate, and tidal controls commonly recognized as causes for sedimentary cyclicity, the most plausible mechanism may have been either the early Pliocene, El Niño-enhanced NAM seasons or the lunar nodal cycle, but further investigation is needed.

6) Sedimentary analysis of the underlying stratigraphic unit revealed heterolithic bedding typical of tide-dominated deposition, oscillatory structures indicating wave influences, and lamination and ripples distinctive to current flow. This section was interpreted as a mixed-influence, distal prodelta with minimal riverine input.

7) Based on previous studies of the progression, via 'lake fill and spill', of the lower Colorado River to the Gulf of California and the results of this study, the timing and sequence of events leading to the deposition of the MHM hyperpycnites can be surmised. At ~5.1-4.8 Ma paleo-lake Blythe mitigated Colorado River discharge and sediment load likely resulting in the heterolithic deposits of the mixed influence, distal prodelta unit stratigraphically below the rhythmite section. Subsequent to the final draining of paleo-lake Blythe (~4.8 Ma), the Colorado River flowed unimpeded into the Gulf of California, commencing deposition of the MHM hyperpycnites and heralding the transition from a mixed-influence, distal prodelta to a fully fluvial-dominated proximal prodeltaic environment.

This study contributes to the documentation of fine-grained hyperpycnites in the ancient rock record, previous work on the initiation and progradation of the Pliocene Colorado River delta, and the growing evidence for the lake-spillover model of the advancement of the lower Colorado River to the Gulf of California. This study could be enriched with further research in several areas, including:

1) In-depth facies and microfacies analysis of the lower, heterolithic deposits of section FC6-1 to identify the mode of deposition and degree of tidal and wave influences,

2) Additional thin section analysis to better characterize the type and degree of bioturbation in the rhythmite section,

3.) Additional study of the character and bed thickness variability of the rhythmites by adding sections and samples from other MHM outcrops, and

4) Study of the transition of the MHM prodelta to the overlying Yuha Member distal delta front to improve our understanding of Pliocene Colorado River progradation.

REFERENCES

Apostoli, A., Gough, W., and Jien, J., 2016, Impact of El-Nino Southern-Oscillation and Sea Surface Temperature on Eastern North Pacific Tropical Cyclones: J Geogr Nat Disast, v. 6, no. 171, p. 2167-0587.1000171.

Archer, A. W., and Kvale, E. P., 1989, Seasonal and yearly cycles within tidally laminated sediments: an example from the Pennsylvanian of Indiana, USA, *in* Cobb, J. C., ed., Geology of the Lower Pennsylvanian in Kentucky, Indiana, and Illinois, Volume 1, Illinois Basin Studies, Illinois Basin Consortium (Kentucky Geological Survey, Indiana Geological Survey, and Illinois State Geological Survey), p. 45-56.

Axen, G. J., and Fletcher, J. M., 1998, Late Miocene-Pleistocene extensional faulting, northern Gulf of California, Mexico and Salton Trough, California: International Geology Review, v. 40, no. 3, p. 217-244.

Barreiro, M., Philander, G., Pacanowski, R., and Fedorov, A., 2006, Simulations of warm tropical conditions with application to middle Pliocene atmospheres: Climate Dynamics, v. 26, no. 4, p. 349-365.

Bhattacharya, J. P., 2006, Deltas, *in* Posamentier, H. W., and Walker, R. G., eds., Facies Models Revisited, Volume 84, SEPM Society for Sedimentary Geology, p. 237-292.

Bhattacharya, J. P., and MacEachern, J. A., 2009, Hyperpycnal rivers and prodeltaic shelves in the Cretaceous seaway of North America: Journal of Sedimentary Research, v. 79, no. 4, p. 184-209.

Blackwelder, E., 1934, Origin of the Colorado River: Geological Society of America Bulletin, v. 45, no. 3, p. 551-566.

Bohacs, K. M., Lazar, O. R., and Demko, T. M., 2014, Parasequence types in shelfal mudstone strata—Quantitative observations of lithofacies and stacking patterns, and conceptual link to modern depositional regimes: Geology, v. 42, no. 2, p. 131-134.

Bonham, S. G., Haywood, A. M., Lunt, D. J., Collins, M., and Salzmann, U., 2009, El Niño–Southern Oscillation, Pliocene climate and equifinality: Philosophical Transactions of the Royal Society of London A: Mathematical, Physical and Engineering Sciences, v. 367, no. 1886, p. 127-156.

Bonnecaze, R. T., and Lakshminarasimhan, S., 2005, Characterization of turbiditic oil reservoirs based on geophysical models of their formation: The University of Texas at Austin, DOE Award #: DE-FC26-01BC15352

Bordoni, S., Ciesielski, P. E., Johnson, R. H., McNoldy, B. D., and Stevens, B., 2004, The low-level circulation of the North American Monsoon as revealed by QuikSCAT: Geophysical Research Letters, v. 31, no. 10.

Bright, J., Cohen, A. S., Dettman, D. L., Pearthree, P. A., Dorsey, R. J., and Homan, M. B., 2016, Did a catastrophic lake spillover integrate the late Miocene early Pliocene Colorado River and the Gulf of California?: Microfaunal and stable isotope evidence from Blythe Basin, California-Arizona, USA: PALAIOS, v. 31, no. 3, p. 81-91.

Burgess, P. M., 2016, Identifying Ordered Strata: Evidence, Methods, and Meaning: Journal of Sedimentary Research, v. 86, no. 3, p. 148-167.

Chapin, C. E., 2008, Interplay of oceanographic and paleoclimate events with tectonism during middle to late Miocene sedimentation across the southwestern USA: Geosphere, v. 4, no. 6, p. 976-991.

Cloos, M. E., 2014, Detrital zircon U-Pb and (U-Th)/He geo-thermochronometry and submarine turbidite fan development in the Mio-Pliocene Gulf of California, Fish Creek-Vallecito Basin, southern California [M.S.]: The University of Texas at Austin.

D'Arrigo, R. D., and Jacoby, G. C., 1991, A 1000-year record of winter precipitation from northwestern New Mexico, USA: a reconstruction from tree-rings and its relation to El Niño and the Southern Oscillation: The Holocene, v. 1, no. 2, p. 95-101.

de Boer, P. L., and Alexandre, J. T., 2012, Orbitally forced sedimentary rhythms in the stratigraphic record: is there room for tidal forcing?: Sedimentology, v. 59, no. 2, p. 379-392.

Diaz, H. G., Contreras, C., Lewis, N., Welsh, R., and Zavala, C., 2011, Evidence of Shelfal Hyperpycnal Deposition of Pliocene Sandstones in the Oilbird Field, Southeast Coast, Trinidad: Impact on Reservoir Distribution, *in* Slatt, R. M., and Zavala, C., eds., Sediment transfer from shelf to deep water—Revisiting the delivery system: AAPG Studies in Geology 61, p. 193-214.

Dorsey, R. J., 2006, Stratigraphy, tectonics, and basin evolution in the Anza-Borrego Desert region, *in* Jefferson, G. T., and Lindsay, L., ed., Fossil treasures of the Anza-Borrego Desert: San Diego, California, Sunbelt Publications, p. 89-104.

-, 2010, Sedimentation and crustal recycling along an active oblique-rift margin: Salton Trough and northern Gulf of California: Geology, v. 38, no. 5, p. 443-446.

Dorsey, R. J., Axen, G. J., Peryam, T. C., and Kairouz, M. E., 2012, Initiation of the southern Elsinore fault at~ 1.2 Ma: evidence from the Fish Creek–Vallecito Basin, southern California: Tectonics, v. 31, no. 2.

Dorsey, R. J., Fluette, A., McDougall, K., Housen, B. A., Janecke, S. U., Axen, G. J., and Shirvell, C. R., 2007, Chronology of Miocene–Pliocene deposits at Split Mountain Gorge, southern California: A record of regional tectonics and Colorado River evolution: Geology, v. 35, no. 1, p. 57-60.

Dorsey, R. J., Fluette, A. L., Housen, B. A., McDougall, K. A., Janecke, S. U., Axen, G. J., and Shirvell, C., 2006, Chronology of Late Miocene to Early Pliocene Sedimentation at Split Mt. Gorge, Western Salton Trough: Implications for Development of the Pacific-North America Plate: Abstracts for NSF MARGINS program, Workshop on Rupturing of Continental Lithosphere: Ensenada Mexico, p. 9-13.

Dorsey, R. J., Housen, B. A., Janecke, S. U., Fanning, C. M., and Spears, A. L., 2011, Stratigraphic record of basin development within the San Andreas fault system: Late Cenozoic Fish Creek–Vallecito basin, southern California: Geological Society of America Bulletin, v. 123, no. 5-6, p. 771-793.

Dorsey, R. J., and Lazear, G., 2013, A post–6 Ma sediment budget for the Colorado River: Geosphere, v. 9, no. 4, p. 781-791.

Einsele, G., Ricken, W., and Seilacher, A., 1991, Cycles and events in stratigraphy, Newark, NJ (United States), Springer-Verlag New York, Inc., 955 p.

Fedorov, A., Dekens, P., McCarthy, M., Ravelo, A., Barreiro, M., Pacanowski, R., and Philander, S., 2006, The Pliocene paradox (mechanisms for a permanent El Niño): Science, v. 312, no. 5779, p. 1485-1489.

Forel, F. A., 1885, Les ravins sous-lacustres des fleuves glaciaires: Comptes Rendus de l'Academie des Sciences, Paris, v. 101, no. 16, p. 725-728.

-, 1892, Le Le´man: Monographie Limnologique 1, Lausanne: F. Rouge, p. 543.

Gani, M. R., and Bhattacharya, J. P., 2007, Basic building blocks and process variability of a Cretaceous delta: internal facies architecture reveals a more dynamic interaction of river, wave, and tidal processes than is indicated by external shape: Journal of Sedimentary Research, v. 77, no. 4, p. 284-302.

Gibson, L., Malinconico, L., Downs, T., and Johnson, N., 1984, Structural implications of gravity data from the Vallecito-Fish Creek basin, western Imperial Valley, California, in Rigsby, C. A., ed., The Imperial Basin - Tectonics, Sedimentation and Thermal Aspects: Pacific Section SEPM, Volume 40, p. 15-29.

Grippo, A., Fischer, A. G., Hinnov, L. A., Herbert, T. D., and Premoli Silva, I., 2004, Cyclostratigraphy and chronology of the Albian stage (Piobbico core, Italy), *in* D'Argenio, B., Fischer, A. G., Premoli Silva, I., Weissert, H., and Ferreri, V., eds., Cyclostratigraphy: Approaches and Case Histories: Society for Sedimentary Geology Special Publication, Volume 81, p. 57-81.

Hanna, G. D., 1926, Paleontology of Coyote Mountain, Imperial County, California, California Academy of Sciences, Proceedings, Ser. 4, v. 14, no. 18, p. 427-503.

Harris, P. T., Hughes, M. G., Baker, E. K., Dalrymple, R. W., and Keene, J. B., 2004, Sediment transport in distributary channels and its export to the pro-deltaic environment in a tidally dominated delta: Fly River, Papua New Guinea: Continental Shelf Research, v. 24, no. 19, p. 2431-2454.

Hereford, R., and Webb, R. H., 1992, Historic variation of warm-season rainfall, southern Colorado Plateau, southwestern USA: Climatic Change, v. 22, no. 3, p. 239-256.

Hereford, R., Webb, R. H., and Graham, S., 2002, Precipitation history of the Colorado Plateau region, 1900-2000, US Department of the Interior, US Geological Survey Fact Sheet 119-02, 4 p.

Hinnov, L. A., 2013, Cyclostratigraphy and its revolutionizing applications in the earth and planetary sciences: Geological Society of America Bulletin, v. 125, no. 11-12, p. 1703-1734.

Homan, M., 2015, Sedimentology and Stratigraphy of the Miocene-Pliocene Bouse Formation near Cibola, Arizona and Milpitas Wash, California: Implications for the Early Evolution of the Colorado River [M.S.]: University of Oregon, 128 p.

House, P. K., Pearthree, P. A., Howard, K. A., Bell, J. W., Perkins, M. E., Faulds, J. E., and Brock, A. L., 2005, Birth of the lower Colorado River—Stratigraphic and geomorphic evidence for its inception near the conjunction of Nevada, Arizona, and California: Field Guides, v. 6, p. 357-387.

House, P. K., Pearthree, P. A., and Perkins, M. E., 2008, Stratigraphic evidence for the role of lake spillover in the inception of the lower Colorado River in southern Nevada and western Arizona: Geological Society of America Special Papers, v. 439, p. 335-353.

Howard, K. A., House, P. K., Dorsey, R. J., and Pearthree, P. A., 2014, River-evolution and tectonic implications of a major Pliocene aggradation on the lower Colorado River: The Bullhead Alluvium: Geosphere, p. GES01059. 01051.

Jackson, J. A., and Bates, R. L., 1997, Glossary of Geology: American Geological Institute, Alexandria, Virginia, 769 p.

Johnson, N. M., Officer, C. B., Opdyke, N. D., Woodard, G. D., Zeitler, P. K., and Lindsay, E. H., 1983, Rates of late Cenozoic tectonism in the Vallecito–Fish Creek basin, western Imperial Valley, California: Geology, v. 11, no. 11, p. 664-667.

Kimbrough, D. L., Grove, M., Gehrels, G. E., Mahoney, J. B., Dorsey, R. J., Howard, K. A., House, P. K., Pearthree, P., and Flessa, K., 2011, Detrital zircon record of Colorado River integration into the Salton Trough, *in* Beard, L. S., Karlstrom, K. E., Young, R. A., and Billingsley, G. H., eds., CREvolution 2 - Origin and evolution of the Colorado River system, workshop abstracts: U.S. Geological Survey Open-File Report 2011-1210, p. 168-174.

Kuenen, P. H., and Migliorini, C., 1950, Turbidity currents as a cause of graded bedding: The Journal of Geology, p. 91-127.

Lamb, M. P., McElroy, B., Kopriva, B., Shaw, J., and Mohrig, D., 2010, Linking river-flood dynamics to hyperpycnal-plume deposits: Experiments, theory, and geological implications: Geological Society of America Bulletin, v. 122, no. 9-10, p. 1389-1400.

Larkins, K. H., 2009, Cyclic sedimentation in the Mississippian Pride Shale: Quantitative paleoenvironmental analysis of tidal rhythmites using X-ray flourescence scanning and advanced spectral methods [M.S.]: University of North Carolina, 77 p.

Li, Z., Bhattacharya, J., and Schieber, J., 2015, Evaluating along-strike variation using thin-bedded facies analysis, Upper Cretaceous Ferron Notom Delta, Utah: Sedimentology, v. 62, no. 7, p. 2060-2089.

Lynch, D. K., and Adams, P. M., 2009, Fish Creek rhythmites and aperiodic temporal sedimentation, *in* Reynolds, R. E., and Jessey, D. R., eds., Landscape Evolution at an Active Plate Margin. [The 2009 Desert Symposium Field Guide and Proceedings], Desert Studies Consortium, California State University, Fullerton, and LSA Associates, Inc., Riverside, California, p. 159-164.

MacEachern, J., and Bann, K., 2008, The role of ichnology in refining shallow marine facies models: Recent Advances in Models of Siliciclastic Shallow-Marine Stratigraphy: SEPM, Special Publication, v. 90, p. 73-116.

Mazumder, R., and Arima, M., 2005, Tidal rhythmites and their implications: Earth-Science Reviews, v. 69, no. 1, p. 79-95.

McIlroy, D., 2006, Ichnology of a macrotidal tide-dominated deltaic depositional system: Lajas Formation, Neuquén Province, Argentina: SEPM, Special Publication, v. 88, p. 195-211.

Meek, N., and Douglass, J., 2001, Lake overflow: An alternative hypothesis for Grand Canyon incision and development of the Colorado River: Colorado River: Origin and evolution: Grand Canyon, Arizona, Grand Canyon Association, p. 199-204.

Meyers, S. R., Sageman, B. B., and Hinnov, L. A., 2001, Integrated quantitative stratigraphy of the Cenomanian-Turonian Bridge Creek Limestone member using evolutive harmonic analysis and stratigraphic modeling: Journal of Sedimentary Research, v. 71, p. 628-644.

Middleton, G. V., 1967, Experiments on density and turbidity currents: III. Deposition of sediment: Canadian Journal of Earth Sciences, v. 4, no. 3, p. 475-505.

Miller, D. J., and Eriksson, K. A., 1997, Late Mississippian prodeltaic rhythmites in the Appalachian Basin: a hierarchical record of tidal and climatic periodicities: Journal of Sedimentary Research, v. 67, no. 4.

Molnar, P., and Cane, M. A., 2002, El Niño's tropical climate and teleconnections as a blueprint for pre-Ice Age climates: Paleoceanography, v. 17, no. 2.

Mulder, T., and Alexander, J., 2001, The physical character of subaqueous sedimentary density flows and their deposits: Sedimentology, v. 48, no. 2, p. 269-299.

Mulder, T., and Chapron, E., 2011, Flood deposits in continental and marine environments: character and significance, *in* Slatt, R. M., and Zavala, C., eds., Sediment transfer from shelf to deep water—Revisiting the delivery system, AAPG Studies in Geology 61, p. 1-30.

Mulder, T., Migeon, S., Savoye, B., and Faugères, J.-C., 2001, Inversely graded turbidite sequences in the deep Mediterranean: a record of deposits from flood-generated turbidity currents?: Geo-Marine Letters, v. 21, no. 2, p. 86-93.

-, 2002, Reply to discussion by Shanmugam on Mulder et al.(2001, Geo-Marine Letters 21: 86-93) Inversely graded turbidite sequences in the deep Mediterranean. A record of deposits from flood-generated turbidity currents?: Geo-Marine Letters, v. 22, no. 2, p. 112-120.

Mulder, T., and Syvitski, J. P., 1995, Turbidity currents generated at river mouths during exceptional discharges to the world oceans: The Journal of Geology, p. 285-299.

Mulder, T., Syvitski, J. P., Migeon, S., Faugeres, J.-C., and Savoye, B., 2003, Marine hyperpycnal flows: initiation, behavior and related deposits. A review: Marine and Petroleum Geology, v. 20, no. 6, p. 861-882.

Mutti, E., Davoli, G., Tinterri, R., and Zavala, C., 1996, The importance of ancient fluvio-deltaic systems dominated by catastrophic flooding in tectonically active basins: Memorie di Scienze Geologiche, v. 48, p. 233-291.

Mutti, E., Tinterri, Roberto, Benevelli, Giovanni, di Biase, Davide, and Cavanna, Giorgio, 2003, Deltaic, mixed and turbidite sedimentation of ancient foreland basins: Marine and Petroleum Geology, v. 20, no. 6, p. 733-755.

Nakajima, T., 2006, Hyperpycnites deposited 700 km away from river mouths in the central Japan Sea: Journal of Sedimentary Research, v. 76, no. 1, p. 60-73.

Newberry, J. S., 1861, Geological Report, *in* Ives, J. C., and Newberry, J. S., eds., Report upon the Colorado River of the West, explored in 1857 and 1858 by Lieutenant Joseph C. Ives, under the direction of the Office of Explorations and Surveys, A.A. Humphreys, Captain Topographical Engineers, in charge. By order of the Secretary of War: Washington, D.C., Govt. Print. Off., p. B001-B160.

Opdyke, N., Lindsay, E., Johnson, N. M., and Downs, T., 1977, The paleomagnetism and magnetic polarity stratigraphy of the mammal-bearing section of Anza Borrego State Park, California: Quaternary Research, v. 7, no. 3, p. 316-329.

Park, J.-H., and Chang, H.-Y., 2013, Drought over Seoul and its association with solar cycles: Journal of Astronomy and Space Sciences, v. 30, no. 4, p. 241-246.

Parsons, J. D., Bush, J. W., and Syvitski, J. P., 2001, Hyperpycnal plume formation from riverine outflows with small sediment concentrations: Sedimentology, v. 48, no. 2, p. 465-478.

Peryam, T. C., 2012, Sedimentation, climate change and tectonics: Dynamic stratigraphy of the Pliocene-Pleistocene Palm Spring Group, Fish Creek-Vallecito Basin, California [Ph.D.]: University of Oregon, 190 p.

Plink-Björklund, P., and Steel, R. J., 2004, Initiation of turbidity currents: outcrop evidence for Eocene hyperpycnal flow turbidites: Sedimentary Geology, v. 165, no. 1, p. 29-52.

Plint, A. G., 2014, Mud dispersal across a Cretaceous prodelta: storm-generated, wave-enhanced sediment gravity flows inferred from mudstone microtexture and microfacies: Sedimentology, v. 61, no. 3, p. 609-647.

Prothero, D. R., and Schwab, F., 1996, Sedimentary Geology, W.H. Freeman and Company, 575 p.

Reineck, H.-E., and Singh, I. B., 1980, Depositional sedimentary environments: with reference to terrigenous clastics, Springer-Verlag Berlin Heidelberg, 551 p.

Remeika, P., 1995, Basin tectonics, stratigraphy, and depositional environments of the western Salton Trough detachment, *in* Remeika, P., and Sturz, Anne, ed., Paleontology and Geology of the Western Salton Trough Detachment, Anza-

Borrego Desert State Park, California: San Diego Association of Geologists Field Trip Guidebook I: San Diego, California, p. 3-54.

Romero-Vadillo, E., Zaytsev, O., and Morales-Pérez, R., 2007, Tropical cyclone statistics in the northeastern Pacific: Atmósfera, v. 20, no. 2, p. 197-213.

Roskowski, J. A., Patchett, P. J., Spencer, J. E., Pearthree, P. A., Dettman, D. L., Faulds, J. E., and Reynolds, A. C., 2010, A late Miocene–early Pliocene chain of lakes fed by the Colorado River: Evidence from Sr, C, and O isotopes of the Bouse Formation and related units between Grand Canyon and the Gulf of California: Geological Society of America Bulletin, v. 122, no. 9-10, p. 1625-1636.

Schieber, J., 2016, Mud re-distribution in epicontinental basins–Exploring likely processes: Marine and Petroleum Geology, v. 71, p. 119-133.

Schieber, J., Southard, J., and Thaisen, K., 2007, Accretion of mudstone beds from migrating flocculle ripples: Science, v. 318, no. 5857, p. 1760-1763.

Schultz, L. W., 2008, Some climatological aspects of tropical cyclones in the eastern north Pacific: National Weather Digest, v. 32, no. 1.

Smith, G. R., and Patterson, W. P., 1994, Mio-Pliocene seasonality on the Snake River plain: comparison of faunal and oxygen isotopic evidence: Palaeogeography, Palaeoclimatology, Palaeoecology, v. 107, no. 3-4, p. 291-302.

Soyinka, O. A., and Slatt, R. M., 2008, Identification and micro-stratigraphy of hyperpycnites and turbidites in Cretaceous Lewis Shale, Wyoming: Sedimentology, v. 55, no. 5, p. 1117-1133.

Sparks, R. S. J., Bonnecaze, Roger T., Huppert, Herbert E., Lister, John R., Hallworth, Mark A., Mader, Heidy, and Phillips, Jeremy, 1993, Sediment-laden gravity currents with reversing buoyancy: Earth and Planetary Science Letters, v. 114, no. 2, p. 243-257.

Spencer, J. E., Patchett, P. J., Pearthree, P. A., House, P. K., Sarna-Wojcicki, A. M., Wan, E., Roskowski, J. A., and Faulds, J. E., 2013, Review and analysis of the age and origin of the Pliocene Bouse Formation, lower Colorado River Valley, southwestern USA: Geosphere, v. 9, no. 3, p. 444-459.

Stevenson, C. J., Jackson, C. A.-L., Hodgson, D. M., Hubbard, S. M., and Eggenhuisen, J. T., 2015, Deep-water sediment bypass: Journal of Sedimentary Research, v. 85, no. 9, p. 1058-1081.

Thomson, D. J., 1982, Spectrum estimation and harmonic analysis: Proceedings of the IEEE, v. 70, no. 9, p. 1055-1096.

Wang, H., Bi, N., Wang, Y., Saito, Y., and Yang, Z., 2010, Tide-modulated hyperpycnal flows off the Huanghe (Yellow River) mouth, China: Earth Surface Processes and Landforms, v. 35, no. 11, p. 1315-1329.

Wara, M. W., Ravelo, A. C., and Delaney, M. L., 2005, Permanent El Niño-like conditions during the Pliocene warm period: Science, v. 309, no. 5735, p. 758-761.

Wilson, R. D., and Schieber, J., 2014, Muddy prodeltaic hyperpycnites in the Lower Genesee Group of Central New York, USA: implications for mud transport in epicontinental seas: Journal of Sedimentary Research, v. 84, no. 10, p. 866-874.

-, 2015, Sedimentary facies and depositional environment of the Middle Devonian Geneseo Formation of New York, USA: Journal of Sedimentary Research, v. 85, no. 11, p. 1393-1415.

Winker, C. D., 1987, Neogene stratigraphy of the Fish Creek-Vallecito section, southern California: implications for early history of the northern Gulf of California and Colorado delta [Ph.D.]: University of Arizona, 494 p.

Winker, C. D., and Kidwell, S. M., 1996, Stratigraphy of a marine rift basin: Neogene of the Western Salton Trough, California, *in* Abbott, P. L., and Cooper, J. D., eds., Field conference guidebook and volume for the annual convention, San Diego California: Bakersfield, California, Pacific Section, AAPG, p. 295-336.

Zavala, C., Arcuri, M., Di Meglio, M., Diaz, H. G., and Contreras, C., 2011, A genetic facies tract for the analysis of sustained hyperpycnal flow deposits, *in* Slatt, R. M., and C. Zavala, ed., Sediment transfer from shelf to deep water—Revisiting the delivery system, Volume AAPG Studies in Geology 61, p. 31-51.

Zavala, C., Gamero, Helena, and Arcuri, Mariano, 2006, Lofting rhythmites: a diagnostic feature for the recognition of hyperpycnal deposits: Geological Society of America Abstracts with Programs, v. 38, no. 7, p. 541.

APPENDIX A

BED THICKNESS MEASUREMENTS: SECTION FC6-1

Deposits of the stratigraphically lower section FC6-1 (see F 4 for location of section) were categorized into four facies: sand-dominated (Sd, ~>75% sand); sand-rich (Sm, more sand than mud, ~50-75% sand); mud-rich (Ms, more mud than sand, ~25-50% sand); and mud-dominated (Md, ~<25% sand). Measurements of individual contiguous beds (total=458) are numbered from bottom up and grouped within the respective consecutive segments (from 1A to 1Q) in which they were measured.

Segment	Bed #	Facies	Thickness (+/-0.25 cm)
1A Top	24	md	1.5
	23	sd	4.5
	22	md	1.5
	21	sd	10.5
	20	md	3.0
	19	sm	8.5
	18	md	7.0
	17	ms	6.0
	16	md	3.0
	15	ms	4.0
	14	md	2.5
	13	sd	8.0
	12	md	2.0
	11	ms	6.0
	10	md	3.5
	9	ms	2.5
	8	sd	4.5
	7	md	2.5
	6	ms	4.0
	5	md	3.0
	4	sd	7.0
	3	md	3.0
	2	ms	5.0
1A	1	md	2.0

Segment	Bed #	Facies	Thickness (+/-0.25 cm)
1B Top	54	md	3.5
	53	ms	4.0
	52	md	5.0
	51	sd	6.0
	50	md	3.0
	49	ms	4.0
	48	md	2.5
	47	sd	6.0
	46	md	3.0
	45	sd	4.0
	44	md	3.0
	43	sd	5.0
	42	md	5.0
	41	sm	3.5
	40	md	3.0
	39	ms	3.5
	38	md	5.0
	37	sd	5.0
	36	md	3.5
	35	sd	12.0
	34	md	5.0
	33	sm	5.0
	32	md	6.0
	31	sd	5.0
	30	md	5.0
	29	ms	11.0
	28	md	1.5
	27	sd	10.0
	26	md	2.0
1B	25	sd	10.0

Segment	Bed #	Facies	Thickness (+/-0.25 cm)
1C Top	88	sm	4.0
	87	md	2.0
	86	sd	4.0
	85	md	2.0
	84	ms	5.0
	83	sd	7.5
	82	md	3.0
	81	sd	5.5
	80	md	4.0
	79	sm	11.0
	78	md	2.5
	77	sd	11.0
	76	md	1.5
	75	ms	5.5
	74	md	1.5
	73	sd	8.0
	72	md	2.0
	71	sd	8.0
	70	md	2.0
	69	sd	10.0
	68	md	3.5
	67	sd	4.0
	66	md	1.5
	65	sd	11.5
	64	md	1.0
	63	ms	4.0
	62	md	2.5
	61	sd	12.0
	60	md	2.0
	59	sm	2.5
	58	md	2.5
	57	sm	3.0
	56	sd	4.5
1C	55	ms	7.5

Segment	Bed #	Facies	Thickness (+/-0.25 cm)
1D Top	96	sm	8.0
	95	ms	8.5
	94	md	3.0
	93	sd	4.0
	92	md	2.5
	91	sm	4.5
	90	sd	6.0
1D	89	md	2.5

Segment	Bed #	Facies	Thickness (+/-0.25 cm)
1E Top	126	md	2.0
	125	sm	5.0
	124	md	5.0
	123	sm	5.0
	122	md	3.0
	121	ms	5.0
	120	md	3.0
	119	ms	3.0
	118	sd	4.0
	117	md	2.0
	116	sd	4.0
	115	md	3.0
	114	ms	18.0
	113	sm	6.0
	112	md	3.0
	111	ms	2.0
	110	md	3.0
	109	sd	6.0
	108	md	7.0
	107	ms	4.0
	106	md	2.0
	105	sm	5.0
	104	md	3.0
	103	ms	8.5
	102	md	5.5
	101	ms	5.0
	100	md	3.0
	99	sd	2.5
	98	md	2.0
1E	97	ms	11.0

Segment	Bed #	Facies	Thickness (+/-0.25 cm)
1F Top	167	sd	7.0
	166	md	5.0
	165	sd	3.5
	164	md	3.0
	163	sd	5.0
	162	md	3.5
	161	sm	1.5
	160	md	3.0
	159	ms	2.5
	158	md	3.0
	157	sm	1.5
	156	md	2.0
	155	sm	2.0
	154	md	3.5
	153	sm	4.0
	152	md	3.0
	151	sd	5.0
	150	md	2.0
	149	sd	4.5
	148	ms	6.0
	147	sd	11.0
	146	md	2.5
	145	sm	3.0
	144	md	5.5
	143	sm	2.0
	142	md	3.0
	141	sm	1.0
	140	md	3.0
	139	sm	1.0
	138	md	1.5
	137	ms	2.0
	136	md	9.0
	135	ms	6.0
	134	md	3.0
	133	sd	4.0
	132	md	3.0
	131	sm	1.5
	130	md	2.5
	129	sm	1.0
	128	md	2.0
1F	127	sd	4.0

Segment	Bed #	Facies	Thickness (+/-0.25 cm)
1H Top	221	md	5.0
	220	sm	4.5
	219	md	3.0
	218	sm	7.0
	217	md	3.5
	216	sd	5.0
	215	md	10.0
	214	sm	5.0
	213	md	3.0
	212	sm	6.0
	211	md	2.0
	210	sd	8.0
	209	md	6.0
	208	sd	2.5
	207	md	3.5
	206	sd	3.5
	205	md	2.0
	204	sd	1.5
	203	md	2.0
	202	sm	3.0
	201	md	2.0
	200	sm	2.5
	199	md	3.0
	198	sd	4.0
	197	md	4.0
	196	sd	8.0
	195	md	3.0
	194	sm	3.0
1H	193	sd	7.5

Segment	Bed #	Facies	Thickness (+/-0.25 cm)
1G Top	192	md	2.0
	191	sd	7.5
	190	md	3.5
	189	sd	4.5
	188	md	3.0
	187	sm	2.0
	186	md	4.0
	185	sd	6.0
	184	md	2.5
	183	sd	4.0
	182	md	2.5
	181	sd	6.0
	180	md	4.0
	179	sd	4.0
	178	md	3.0
	177	sd	9.0
	176	md	10.0
	175	sd	2.0
	174	md	3.0
	173	sm	2.5
	172	md	2.0
	171	sm	2.5
	170	md	4.0
	169	sd	8.0
1G	168	md	5.0

Segment	Bed #	Facies	Thickness (+/-0.25 cm)
1J Top	295	md	1.0
	294	ms	5.0
	293	md	1.5
	292	sm	2.0
	291	md	2.0
	290	sm	3.0
	289	md	3.0
	288	sm	2.5
	287	md	6.0
	286	ms	8.0
	285	md	3.0
	284	ms	2.0
	283	md	3.0
	282	ms	4.0
	281	md	2.5
	280	ms	3.0
	279	md	4.0
	278	ms	3.0
	277	md	3.0
	276	ms	3.0
	275	md	4.0
	274	ms	1.0
	273	md	3.0
	272	ms	2.0
	271	md	6.0
	270	ms	5.0
	269	md	9.5
	268	ms	2.5
	267	md	6.5
	266	ms	3.0
	265	md	6.5
	264	sm	3.0
	263	md	4.5
	262	sm	7.0
	261	md	3.0
	260	ms	8.0
	259	md	4.0
	258	ms	2.5
	257	md	3.0
1J	256	ms	6.0

Segment	Bed #	Facies	Thickness (+/-0.25 cm)
1I Top	255	md	5.0
	254	ms	10.5
	253	md	7.0
	252	sd	5.0
	251	md	7.0
	250	sd	1.0
	249	md	5.0
	248	sd	6.5
	247	md	4.0
	246	sd	6.0
	245	md	4.0
	244	sm	9.0
	243	md	8.0
	242	ms	1.0
	241	md	3.0
	240	sm	4.0
	239	md	4.0
	238	ms	3.0
	237	md	3.0
	236	sm	7.0
	235	md	12.0
	234	ms	10.0
	233	md	10.0
	232	sd	3.0
	231	md	4.0
	230	sd	4.0
	229	md	5.0
	228	sd	4.5
	227	md	3.5
	226	sd	5.0
	225	md	5.0
	224	sd	5.0
	223	md	3.0
1I	222	sd	6.0

Segment	Bed #	Facies	Thickness (+/-0.25 cm)
1K Top	316	ms	16.0
	315	sm	7.0
	314	md	3.0
	313	sm	5.5
	312	md	3.0
	311	sm	9.0
	310	md	3.0
	309	ms	10.0
	308	md	3.0
	307	ms	1.0
	306	md	5.0
	305	ms	1.0
	304	md	2.0
	303	ms	4.5
	302	md	5.0
	301	sd	6.5
	300	ms	6.0
	299	md	4.5
	298	ms	4.5
	297	md	3.5
1K	296	sm	2.5

Segment	Bed #	Facies	Thickness (+/-0.25 cm)
	357	sm	3.0
	356	md	5.0
	355	sm	5.0
	354	md	3.5
	353	sd	7.5
	352	ms	4.5
	351	md	6.5
	350	ms	9.0
	349	sd	7.5
	348	md	1.5
	347	ms	9.0
	346	md	3.5
	345	sd	13.0
	344	md	2.5
	343	sm	5.0
	342	md	5.0
	341	sm	4.0
	340	md	2.5
	339	sm	6.5
	338	md	2.0
	337	ms	4.5
	336	md	9.0
	335	ms	2.0
	334	md	4.5
	333	ms	2.5
	332	md	4.0
	331	ms	4.0
	330	md	7.0
	329	ms	3.5
	328	md	3.0
	327	ms	6.0
	326	md	6.0
	325	ms	5.5
	324	md	2.0
	323	ms	5.0
	322	md	3.0
	321	sm	1.5
	320	md	3.5
	319	sm	6.5
	318	md	3.0
1L	317	sd	7.5

Segment	Bed #	Facies	Thickness (+/-0.25 cm)
1L Top	370	md	5.0
	369	ms	1.0
	368	md	4.0
	367	ms	4.0
	366	md	5.5
	365	ms	3.0
	364	md	5.5
	363	ms	1.5
	362	md	4.0
	361	ms	2.5
	360	md	4.0
	359	ms	5.0
	358	md	5.0

Segment	Bed #	Facies	Thickness (+/-0.25 cm)
1M Top	392	md	1.0
	391	sd	13.0
	390	md	5.5
	389	sd	3.0
	388	md	13.0
	387	sd	9.0
	386	md	16.0
	385	sd	2.0
	384	md	3.0
	383	sd	9.0
	382	md	31.0
	381	sd	7.0
	380	md	4.5
	379	sd	4.0
	378	md	8.0
	377	sd	5.0
	376	md	10.5
	375	sd	4.0
	374	md	5.0
	373	sd	2.5
	372	md	3.5
1M	371	ms	3.0

Segment	Bed #	Facies	Thickness (+/-0.25 cm)
1N Top	420	sd	38.0
	419	md	1.0
	418	sd	22.0
	417	md	2.0
	416	sd	12.0
	415	md	1.0
	414	sd	5.5
	413	md	3.0
	412	sd	6.5
	411	md	1.0
	410	sd	6.0
	409	md	1.0
	408	sd	9.0
	407	md	4.5
	406	sd	10.5
	405	md	2.5
	404	sd	10.5
	403	md	4.5
	402	ms	7.5
	401	md	2.0
	400	sd	6.0
	399	md	2.0
	398	sd	23.0
	397	sm	11.0
	396	md	4.0
	395	sd	4.0
	394	md	2.5
1N	393	sm	5.0

Segment	Bed #	Facies	Thickness (+/-0.25 cm)
1O Top	443	md	1.5
	442	sd	13.0
	441	md	2.0
	440	sd	13.0
	439	md	2.0
	438	sd	11.0
	437	md	3.0
	436	sd	18.0
	435	md	1.0
	434	sd	12.5
	433	md	2.0
	432	sd	5.0
	431	md	3.5
	430	sd	7.0
	429	md	2.0
	428	sd	11.0
	427	md	2.5
	426	sm	8.0
	425	md	1.0
	424	sm	6.5
	423	md	1.0
	422	sd	12.0
1O	421	ms	5.0

Segment	Bed #	Facies	Thickness (+/-0.25 cm)
Top FC6-1: directly underlying 1st rhythmite of FC6-2	459	md	56.0
Obscured			~700
1Q Top	458	ms	280.0
	457	sd	5.0
	456	md	3.0
	455	sd	31.0
	454	md	1.5
	453	sd	10.5
	452	md	4.5
	451	sd	1.5
	450	ms	10.0
	449	md	7.5
	448	sm	19.0
1Q	447	md	2.0

Segment	Bed #	Facies	Thickness (+/-0.25 cm)
1P Top	446	sm	471.0
	445	md	3.0
1P	444	sd	14.0

APPENDIX B

BED THICKNESS MEASUREMENTS: SECTION FC6-2

Measurements of individual contiguous couplets (total=265) are numbered from bottom up and grouped within the respective consecutive segments (from Aa to AA) in which they were measured.

Segment	Couplet #	Thickness (+/- 0.25 cm) Coarse Bed	Fine Bed	Couplet (sum)
Aa Top	15	11.0	1.0	12.0
	14	11.0	2.0	13.0
	13	9.0	2.0	11.0
	12	8.0	2.0	10.0
	11	8.0	1.0	9.0
	10	10.0	2.0	12.0
	9	6.0	1.0	7.0
	8	10.5	3.0	13.5
	7	8.5	3.0	11.5
	6	8.0	2.0	10.0
	5	7.5	1.0	8.5
	4	7.5	1.0	8.5
	3	7.0	1.0	8.0
	2	7.0	3.0	10.0
Aa	1	5.5	1.0	6.5

Segment	Couplet #	Thickness (+/- 0.25 cm) Coarse Bed	Fine Bed	Couplet (sum)
A Top	23	14.0	2.1	16.1
	22	8.3	1.3	9.6
	21	11.0	1.2	12.2
	20	9.2	2.0	11.2
	19	16.0	1.0	17.0
	18	10.5	1.8	12.3
	17	9.0	2.5	11.5
A	16	3.0	0.8	3.8

Segment	Couplet #	Thickness (+/- 0.25 cm)		
		Coarse Bed	Fine Bed	Couplet (sum)
C Top	44	10.0	1.0	11.0
	43	9.0	1.0	10.0
	42	10.0	2.0	12.0
	41	7.5	2.0	9.5
	40	10.0	1.5	11.5
	39	14.0	3.0	17.0
	38	13.0	3.0	16.0
	37	10.0	5.0	15.0
C	36	9.5	4.5	14.0

Segment	Couplet #	Thickness (+/- 0.25 cm)		
		Coarse Bed	Fine Bed	Couplet (sum)
B Top	35	10.0	2.0	12.0
	34	17.0	1.0	18.0
	33	8.0	1.5	9.5
	32	5.5	1.0	6.5
	31	7.0	1.0	8.0
	30	7.0	1.5	8.5
	29	8.0	2.0	10.0
	28	8.0	1.5	9.5
	27	7.5	1.5	9.0
	26	6.5	1.5	8.0
	25	10.5	2.0	12.5
B	24	8.0	2.5	10.5

Segment	Couplet #	Thickness (+/- 0.25 cm)		
		Coarse Bed	Fine Bed	Couplet (sum)
F Top	56	14.0	2.0	16.0
F	55	14.0	3.0	17.0

Segment	Couplet #	Thickness (+/- 0.25 cm)		
		Coarse Bed	Fine Bed	Couplet (sum)
E Top	54	13.0	2.0	15.0
	53	13.0	2.5	15.5
	52	13.0	2.0	15.0
	51	10.0	2.5	12.5
	50	8.0	1.0	9.0
E	49	5.5	1.0	6.5

Segment	Couplet #	Thickness (+/- 0.25 cm)		
		Coarse Bed	Fine Bed	Couplet (sum)
D Top	48	8.0	4.0	12.0
	47	6.0	0.8	6.8
	46	7.5	1.0	8.5
D	45	10.0	3.0	13.0

Segment	Couplet #	Coarse Bed	Fine Bed	Couplet (sum)
		Thickness (+/- 0.25 cm)		
I Top	73	16.0	6.0	22.0
	72	14.0	4.0	18.0
	71	7.0	1.5	8.5
	70	18.0	4.0	22.0
I	69	13.0	2.0	15.0

Segment	Couplet #	Coarse Bed	Fine Bed	Couplet (sum)
		Thickness (+/- 0.25 cm)		
L Top	91	15.0	2.0	17.0
	90	9.0	2.0	11.0
	89	11.0	2.0	13.0
	88	10.5	3.0	13.5
	87	12.0	3.0	15.0
L	86	9.0	1.0	10.0

Segment	Couplet #	Coarse Bed	Fine Bed	Couplet (sum)
		Thickness (+/- 0.25 cm)		
H Top	68	9.5	3.0	12.5
	67	10.5	2.0	12.5
	66	8.0	2.5	10.5
	65	9.0	2.0	11.0
	64	9.0	2.5	11.5
	63	9.0	2.0	11.0
H	62	10.0	2.0	12.0

Segment	Couplet #	Coarse Bed	Fine Bed	Couplet (sum)
		Thickness (+/- 0.25 cm)		
K Top	85	12.0	2.0	14.0
	84	10.0	2.0	12.0
	83	12.0	1.0	13.0
	82	14.0	3.0	17.0
	81	11.0	2.0	13.0
	80	11.5	2.0	13.5
	79	14.0	5.0	19.0
	78	18.0	2.0	20.0
K	77	15.0	2.0	17.0

Segment	Couplet #	Coarse Bed	Fine Bed	Couplet (sum)
		Thickness (+/- 0.25 cm)		
G Top	61	12.0	2.0	14.0
	60	12.0	2.0	14.0
	59	16.0	3.0	19.0
	58	10.0	2.0	12.0
G	57	14.0	2.0	16.0

Segment	Couplet #	Coarse Bed	Fine Bed	Couplet (sum)
		Thickness (+/- 0.25 cm)		
J Top	76	13.0	3.5	16.5
	75	12.0	4.0	16.0
J	74	9.0	2.5	11.5

Thickness (+/- 0.25 cm)

Segment	Couplet #	Coarse Bed	Fine Bed	Couplet (sum)
O Top	113	13.0	3.0	16.0
	112	16.0	6.0	22.0
	111	14.0	2.5	16.5
	110	16.0	2.0	18.0
	109	8.0	2.0	10.0
	108	11.0	2.0	13.0
	107	11.0	2.5	13.5
	106	5.0	2.0	7.0
O	105	14.5	2.0	16.5

Thickness (+/- 0.25 cm)

Segment	Couplet #	Coarse Bed	Fine Bed	Couplet (sum)
Q Top	133	16.0	2.0	18.0
	132	17.0	2.0	19.0
	131	12.0	4.0	16.0
	130	10.0	2.0	12.0
	129	14.0	2.0	16.0
	128	15.0	1.5	16.5
	127	17.0	2.0	19.0
	126	18.0	2.0	20.0
	125	17.0	2.0	19.0
	124	19.0	2.0	21.0
Q	123	14.0	3.0	17.0

Thickness (+/- 0.25 cm)

Segment	Couplet #	Coarse Bed	Fine Bed	Couplet (sum)
N Top	104	12.0	2.0	14.0
	103	16.0	2.0	18.0
	102	9.0	2.0	11.0
	101	10.5	2.5	13.0
	100	14.5	1.0	15.5
	99	18.0	1.0	19.0
	98	11.0	1.5	12.5
N	97	16.0	2.0	18.0

Thickness (+/- 0.25 cm)

Segment	Couplet #	Coarse Bed	Fine Bed	Couplet (sum)
P Top	122	13.0	2.0	15.0
	121	9.0	2.0	11.0
	120	11.0	3.0	14.0
	119	11.0	2.5	13.5
	118	9.0	2.5	11.5
	117	9.0	3.0	12.0
	116	9.0	3.0	12.0
	115	15.0	2.5	17.5
P	114	11.0	2.0	13.0

Thickness (+/- 0.25 cm)

Segment	Couplet #	Coarse Bed	Fine Bed	Couplet (sum)
M Top	96	10.0	0.5	10.5
	95	14.0	2.5	16.5
	94	15.0	3.0	18.0
	93	13.0	2.0	15.0
M	92	13.0	3.0	16.0

Segment	Couplet #	Thickness (+/- 0.25 cm)		
		Coarse Bed	Fine Bed	Couplet (sum)
S Top	154	12.0	2.0	14.0
	153	13.0	1.0	14.0
	152	14.0	1.0	15.0
	151	7.0	1.0	8.0
	150	15.0	2.0	17.0
	149	13.0	1.0	14.0
	148	13.0	1.0	14.0
	147	11.0	1.0	12.0
S	146	12.0	1.0	13.0

Segment	Couplet #	Thickness (+/- 0.25 cm)		
		Coarse Bed	Fine Bed	Couplet (sum)
R Top	145	15.0	1.0	16.0
	144	9.0	1.0	10.0
	143	9.0	1.0	10.0
	142	14.0	1.0	15.0
	141	18.5	2.0	20.5
	140	12.0	3.0	15.0
	139	1.0	1.0	2.0
	138	12.0	2.0	14.0
	137	13.0	1.0	14.0
	136	16.0	1.0	17.0
	135	16.0	1.0	17.0
R	134	16.0	1.0	17.0

Segment	Couplet #	Thickness (+/- 0.25 cm)		
		Coarse Bed	Fine Bed	Couplet (sum)
U Top	174	9.0	3.0	12.0
	173	10.0	3.0	13.0
	172	9.0	3.0	12.0
	171	9.0	1.5	10.5
	170	11.0	1.0	12.0
	169	12.0	1.0	13.0
	168	12.0	1.0	13.0
	167	15.0	1.0	16.0
	166	14.0	1.0	15.0
	165	15.0	1.0	16.0
	164	22.0	1.0	23.0
	163	16.0	1.5	17.5
U	162	12.0	1.0	13.0

Segment	Couplet #	Thickness (+/- 0.25 cm)		
		Coarse Bed	Fine Bed	Couplet (sum)
T Top	161	13.0	2.0	15.0
	160	12.0	3.0	15.0
	159	10.5	2.5	13.0
	158	12.0	1.0	13.0
	157	9.0	1.0	10.0
	156	10.0	1.0	11.0
T	155	11.0	1.0	12.0

Segment	Couplet #	Thickness (+/- 0.25 cm) Coarse Bed	Fine Bed	Couplet (sum)
W Top	201	11.0	3.0	14.0
	200	14.0	2.0	16.0
	199	13.0	1.0	14.0
	198	10.0	2.0	12.0
	197	11.0	3.0	14.0
	196	8.0	2.0	10.0
	195	8.0	2.0	10.0
	194	8.0	2.0	10.0
	193	8.0	1.0	9.0
	192	10.0	1.0	11.0
	191	9.0	1.0	10.0
	190	10.0	3.0	13.0
	189	12.0	2.0	14.0
W	188	12.0	2.0	14.0

Segment	Couplet #	Thickness (+/- 0.25 cm) Coarse Bed	Fine Bed	Couplet (sum)
Y Top	227	8.0	2.0	10.0
	226	8.0	2.0	10.0
	225	8.0	2.0	10.0
	224	10.0	2.0	12.0
	223	10.0	1.0	11.0
	222	12.0	3.0	15.0
	221	12.0	2.0	14.0
	220	8.0	1.0	9.0
	219	11.0	1.0	12.0
	218	11.0	2.0	13.0
	217	9.0	2.0	11.0
	216	9.0	1.0	10.0
	215	10.0	2.0	12.0
	214	8.0	1.0	9.0
	213	10.0	2.0	12.0
	212	10.0	2.0	12.0
Y	211	10.0	1.0	11.0

Segment	Couplet #	Thickness (+/- 0.25 cm) Coarse Bed	Fine Bed	Couplet (sum)
V Top	187	14.0	1.5	15.5
	186	12.0	1.0	13.0
	185	12.0	1.0	13.0
	184	14.0	1.0	15.0
	183	12.0	1.0	13.0
	182	13.0	1.0	14.0
	181	15.0	2.0	17.0
	180	13.0	0.5	13.5
	179	13.0	2.0	15.0
	178	11.0	2.0	13.0
	177	10.0	3.0	13.0
	176	12.0	4.0	16.0
V	175	9.0	3.0	12.0

Segment	Couplet #	Thickness (+/- 0.25 cm) Coarse Bed	Fine Bed	Couplet (sum)
X Top	210	12.0	3.0	15.0
	209	7.0	1.0	8.0
	208	7.0	1.0	8.0
	207	9.0	3.0	12.0
	206	10.0	2.0	12.0
	205	11.0	2.0	13.0
	204	10.0	2.0	12.0
	203	11.0	2.0	13.0
X	202	12.0	2.0	14.0

Segment	Couplet #	Thickness (+/- 0.25 cm) Coarse Bed	Fine Bed	Couplet (sum)
AA Top	265	6.0	1.0	7.0
	264	7.0	1.0	8.0
	263	7.0	1.0	8.0
	262	7.0	2.0	9.0
	261	7.0	1.0	8.0
	260	6.0	1.0	7.0
	259	7.0	1.0	8.0
	258	6.0	1.0	7.0
	257	7.0	1.0	8.0
	256	7.0	2.0	9.0
	255	7.0	1.0	8.0
	254	8.0	1.0	9.0
	253	8.0	1.0	9.0
	252	8.0	1.0	9.0
	251	9.0	1.0	10.0
	250	9.0	1.0	10.0
	249	9.0	1.0	10.0
	248	7.0	1.0	8.0
	247	7.0	1.0	8.0
	246	7.0	1.0	8.0
	245	6.0	1.0	7.0
	244	9.0	1.0	10.0
AA	243	8.0	0.5	8.5

Segment	Couplet #	Thickness (+/- 0.25 cm) Coarse Bed	Fine Bed	Couplet (sum)
Z Top	242	9.0	0.5	9.5
	241	9.0	0.5	9.5
	240	10.0	1.0	11.0
	239	9.0	1.0	10.0
	238	10.0	1.0	11.0
	237	8.0	1.0	9.0
	236	10.0	1.0	11.0
	235	6.0	1.0	7.0
	234	5.0	1.0	6.0
	233	6.0	1.0	7.0
	232	6.0	1.0	7.0
	231	7.0	1.0	8.0
	230	6.0	1.0	7.0
	229	7.0	1.0	8.0
Z	228	9.0	1.0	10.0

SEDIMENTARY LOG: SECTION FC6-2, SEGMENTS A-U

N

M

L

K

clay | silt | fs | ms
sand

Q

P

O

clay | silt | fs | ms
sand

clay	silt	fs	ms
		sand	

clay	silt	fs	ms
		sand	
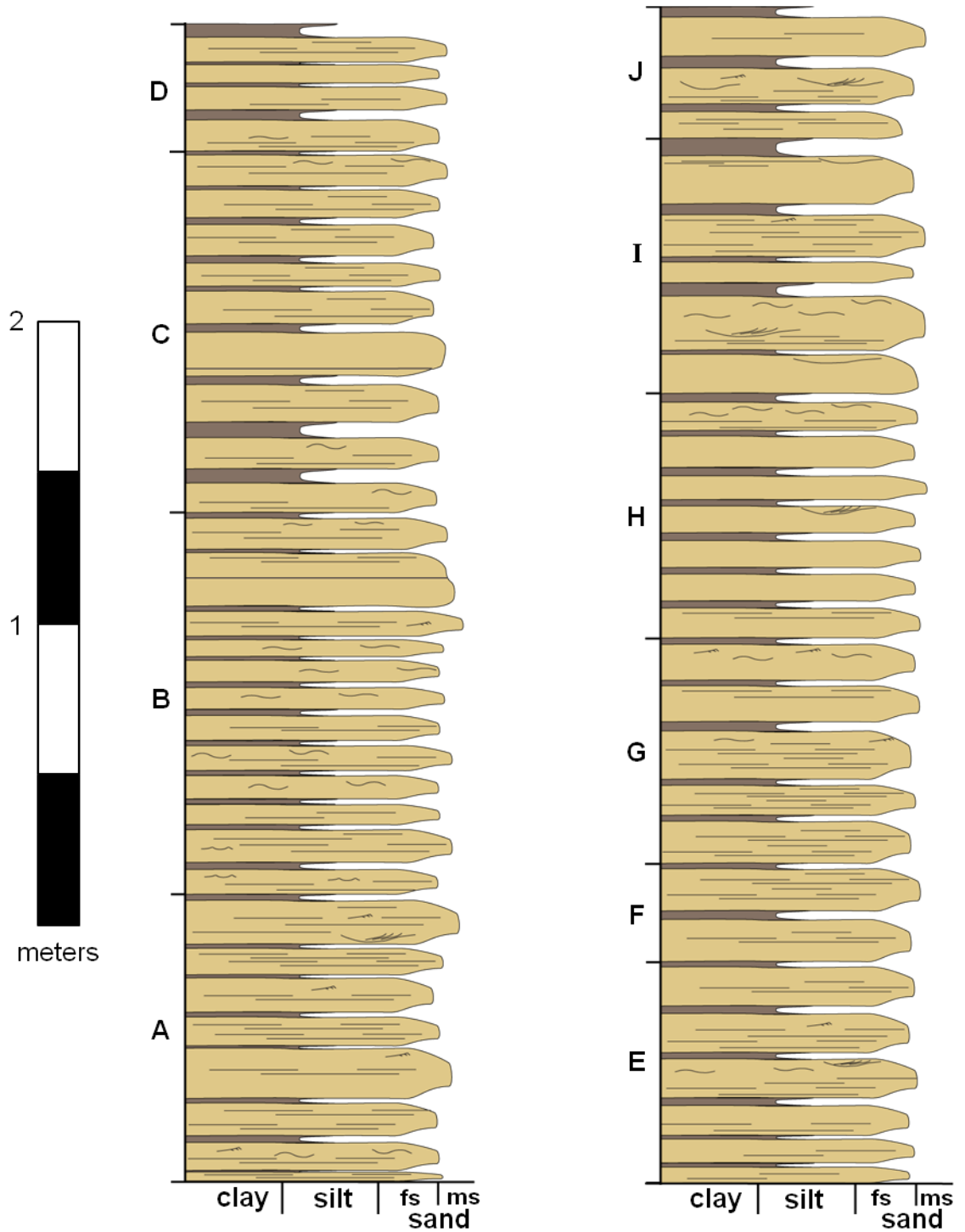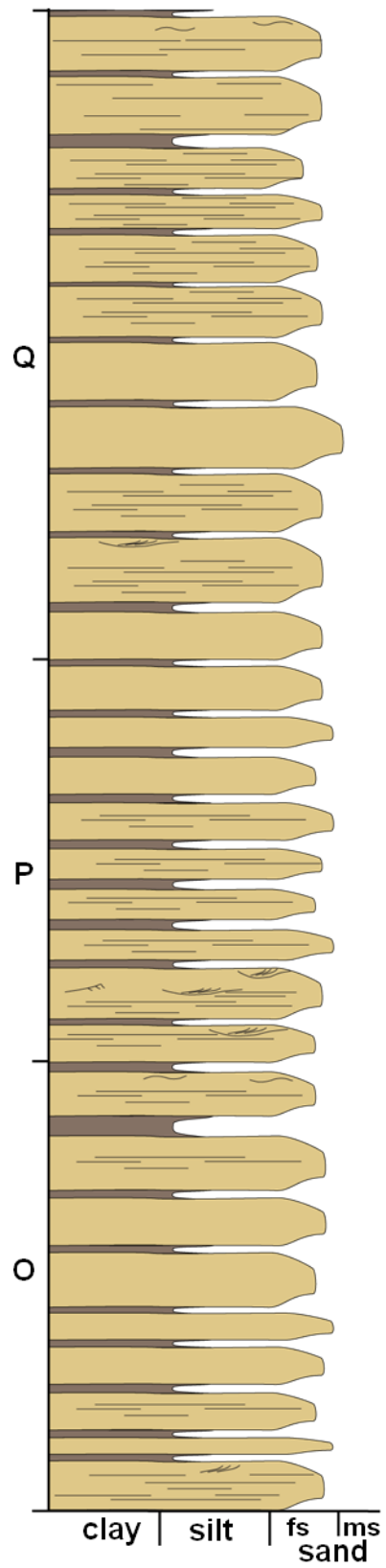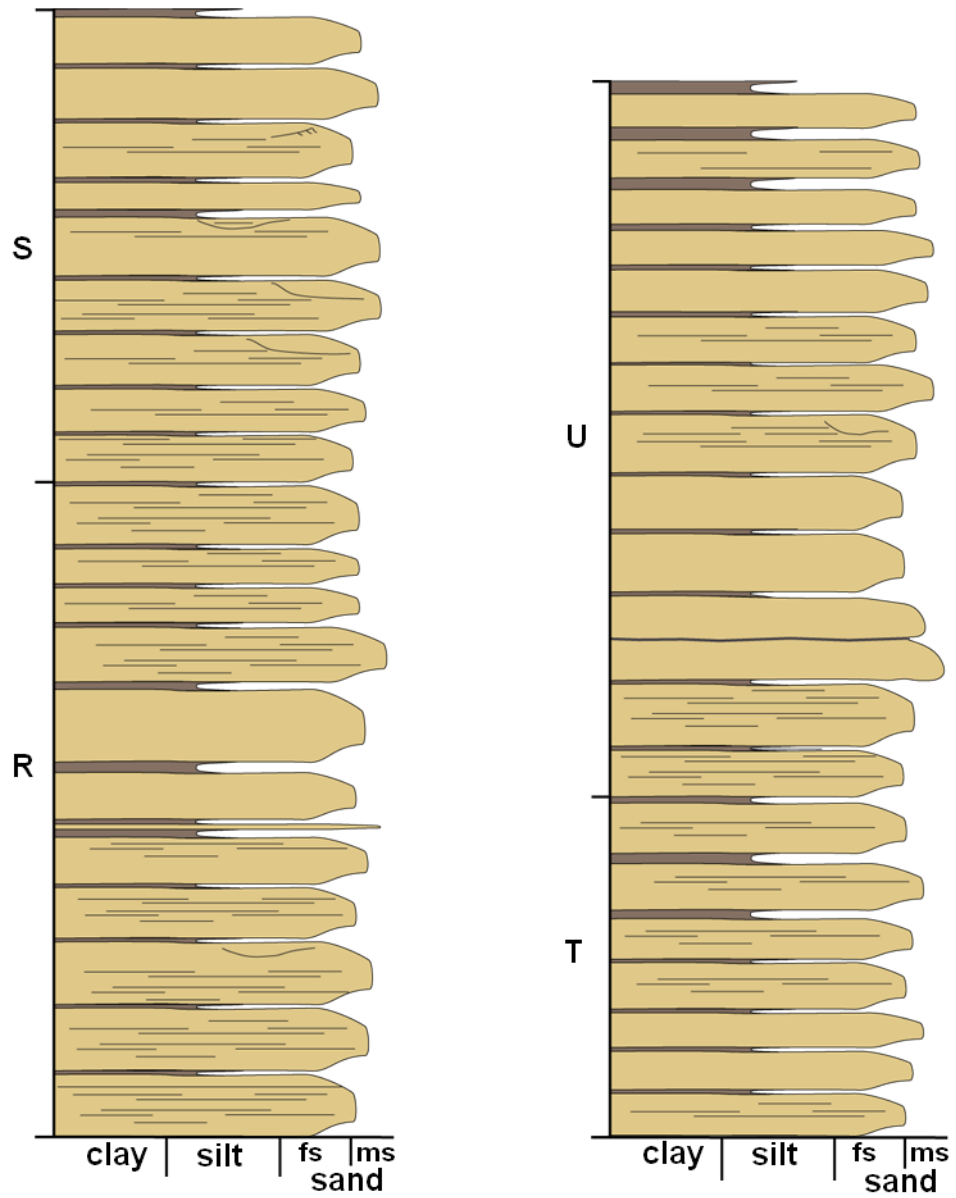
LEGEND

Wavy lamination	∼
Planar lamination	——
Ripple cross-laminae	⌐
Cross-lamination	⫽
Scour	⌣

APPENDIX D

BED THICKNESS MEASUREMENTS: SECTION FC6-3

Measurements of individual contiguous couplets (total=88) are numbered from bottom up and grouped within the respective consecutive segments (from 3A to 3E) in which they were measured. Couplet numbers are continued from the sequence started in Section FC6-2 (Appendix B).

Segment	Couplet #	Coarse Bed	Fine Bed	Couplet (sum)
Thickness (+/- 0.25 cm)				
3A Top	278	4.0	1.0	5.0
	277	5.0	1.0	6.0
	276	3.5	2.0	5.5
	275	6.0	1.0	7.0
	274	6.0	2.0	8.0
	273	6.0	2.0	8.0
	272	6.0	2.0	8.0
	271	6.0	2.0	8.0
	270	7.0	2.0	9.0
	269	4.0	3.0	7.0
	268	5.0	2.0	7.0
	267	4.0	4.0	8.0
3A	266	5.0	2.0	7.0

Segment	Couplet #	Coarse Bed	Fine Bed	Couplet (sum)
Thickness (+/- 0.25 cm)				
3B Top	295	5.0	1.0	6.0
	294	13.0	1.5	14.5
	293	5.0	0.5	5.5
	292	7.0	1.0	8.0
	291	7.0	1.0	8.0
	290	6.0	1.0	7.0
	289	6.0	1.0	7.0
	288	6.0	1.0	7.0
	287	6.0	1.0	7.0
	286	6.0	0.5	6.5
	285	6.0	1.0	7.0
	284	6.0	1.0	7.0
	283	5.0	1.0	6.0
	282	5.0	1.0	6.0
	281	5.0	1.0	6.0
	280	6.0	1.0	7.0
3B	279	5.0	1.0	6.0

Segment	Couplet #	Thickness (+/- 0.25 cm) Coarse Bed	Fine Bed	Couplet (sum)
3C Top	309	5.0	1.0	6.0
	308	6.0	1.0	7.0
	307	6.0	1.0	7.0
	306	5.0	1.0	6.0
	305	4.0	1.0	5.0
	304	7.0	1.0	8.0
	303	6.0	1.0	7.0
	302	7.0	2.0	9.0
	301	5.0	1.0	6.0
	300	6.0	1.0	7.0
	299	6.5	1.0	7.5
	298	6.0	1.0	7.0
	297	6.0	1.0	7.0
3C	296	5.0	1.0	6.0

Segment	Couplet #	Thickness (+/- 0.25 cm) Coarse Bed	Fine Bed	Couplet (sum)
3D Top	329	5.0	1.0	6.0
	328	5.0	1.0	6.0
	327	5.0	1.0	6.0
	326	5.0	1.0	6.0
	325	5.0	1.0	6.0
	324	6.0	1.0	7.0
	323	5.0	2.0	7.0
	322	4.0	2.0	6.0
	321	4.0	1.0	5.0
	320	5.0	1.0	6.0
	319	4.0	1.0	5.0
	318	5.0	2.0	7.0
	317	6.0	2.0	8.0
	316	7.0	3.0	10.0
	315	7.0	3.0	10.0
	314	5.0	2.0	7.0
	313	5.0	1.0	6.0
	312	4.0	2.0	6.0
	311	5.0	2.0	7.0
3D	310	7.0	2.0	9.0

Segment	Couplet #	Thickness (+/- 0.25 cm)		
		Coarse Bed	Fine Bed	Couplet (sum)
3E Top	353	4.0	0.5	4.5
	352	5.0	0.5	5.5
	351	5.0	0.5	5.5
	350	6.0	0.5	6.5
	349	4.0	0.5	4.5
	348	4.0	0.5	4.5
	347	9.0	0.5	9.5
	346	7.0	0.5	7.5
	345	8.0	0.5	8.5
	344	7.0	0.5	7.5
	343	7.0	0.5	7.5
	342	8.0	0.5	8.5
	341	7.0	0.5	7.5
	340	8.0	1.0	9.0
	339	8.0	1.0	9.0
	338	4.0	0.5	4.5
	337	6.0	1.0	7.0
	336	7.0	1.0	8.0
	335	5.0	1.0	6.0
	334	5.0	1.0	6.0
	333	5.0	1.0	6.0
	332	5.0	1.0	6.0
	331	4.0	1.0	5.0
3E	330	4.0	1.0	5.0

APPENDIX E

GRAIN SIZE ANALYSIS DATA

Shown are grain size analysis data of 3 sets of 3 contiguous couplets (C2-4, M1-3, T5-7) from primary section FC6-2 presented in stratigraphic order from base to top of each set of contiguous couplets. Samples to the left (L) and right (R) of couplets M1-3 are also shown. (volume %; µm-microns)

Sample	Mud (%) < 63 µm	Sand (%) 63-500 µm	Mean (µm)	Sample	Mud (%) < 63 µm	Sand (%) 63-500 µm	Mean (µm)
C4-8	94.2	5.8	14.5	M3-8	88.8	11.2	21.7
C4-7	52.1	47.9	62.0	M3-7	67.4	32.6	44.8
C4-6	62.1	37.9	51.7	M3-6	51.6	48.4	62.4
C4-5	60.5	39.5	52.6	M3-5	60.8	39.2	51.2
C4-4	65.3	34.7	49.2	M3-4	56.4	43.6	55.6
C4-3	70.2	29.8	41.8	M3-3	64.7	35.3	47.0
C4-2	82.5	17.5	28.6	M3-2	62.7	37.3	48.7
C4-1	80.1	19.9	30.3	M3-1	77.2	22.8	33.4
C3-8	89.4	10.6	20.2	M2-8	88.1	11.9	21.3
C3-7	89.6	10.4	20.0	M2-7	92.1	7.9	17.3
C3-6	71.5	28.5	39.3	M2-6	52.9	47.1	60.0
C3-5	61.5	38.5	50.9	M2-5	52.4	47.6	60.1
C3-4	64.4	35.6	48.6	M2-4	53.2	46.8	60.9
C3-3	64.1	35.9	48.1	M2-3	64.0	36.0	48.9
C3-2	68.4	31.6	43.6	M2-2	66.0	34.0	45.6
C3-1	71.3	28.7	39.6	M2-1	70.3	29.7	41.0
C2-8	86.3	13.7	23.6	M1-8	84.9	15.1	25.5
C2-7	83.3	16.7	27.1	M1-7	94.2	5.8	14.3
C2-6	60.8	39.2	52.0	M1-6	81.7	18.3	28.6
C2-5	49.8	50.2	64.9	M1-5	55.9	44.1	57.3
C2-4	50.5	49.5	67.1	M1-4	63.7	36.3	50.4
C2-3	65.2	34.8	45.7	M1-3	70.6	29.4	41.5
C2-2	69.6	30.4	42.7	M1-2	67.3	32.7	44.0
C2-1	86.9	13.1	26.2	M1-1	79.6	20.4	31.9

Sample	Mud (%) < 63 μm	Sand (%) 63-500 μm	Mean (μm)
T7-8	90.2	9.8	19.4
T7-7	85.5	14.5	26.3
T7-6	64.5	35.5	47.7
T7-5	54.6	45.4	59.3
T7-4	64.4	35.6	50.7
T7-3	59.9	40.1	53.6
T7-2	63.2	36.8	49.4
T7-1	87.7	12.3	23.6
T6-8	97.5	2.5	10.8
T6-7	66.1	33.9	44.7
T6-6	57.9	42.1	54.9
T6-5	45.9	54.1	69.6
T6-4	45.0	55.0	70.8
T6-3	63.7	36.3	50.0
T6-2	60.4	39.6	53.4
T6-1	66.9	33.1	45.8
T5-8	90.4	9.6	18.6
T5-7	69.4	30.6	43.7
T5-6	53.8	46.2	61.9
T5-5	54.0	46.0	59.9
T5-4	62.4	37.6	51.6
T5-3	63.1	36.9	51.8
T5-2	63.0	37.0	51.0
T5-1	69.1	30.9	54.6

Couplet M3	Coarse bed		Fine bed	
Sample #	M3-CL	M3-CR	M3-FL	M3-FR
Mud (%) < 63 μm	60.7	47.7	94.2	96.0
Sand (%) 63-500 μm	39.3	52.3	5.8	4.0

Couplet M2	Coarse bed		Fine bed	
Sample #	M2-CL	M2-CR	M2-FL	M2-FR
Mud (%) < 63 μm	53.6	66.7	93.1	87.8
Sand (%) 63-500 μm	46.4	33.3	6.9	12.2

Couplet M1	Coarse bed		Fine bed	
Sample #	M1-CL	M1-CR	M1-FL	M1-FR
Mud (%) < 63 μm	46.0	56.9	93.5	94.1
Sand (%) 63-500 μm	54.0	43.1	6.5	5.9

APPENDIX F

X-RAY DIFFRACTION ANALYSIS DATA

Shown are XRD analysis data of 3 sets of 3 contiguous couplets (C2-4, M1-3, T5-7) presented in stratigraphic order from base to top of each set of contiguous couplets. Samples to the left (L) and right (R) of couplets M1-3 are also shown. (weight %)

	Sample	Quartz (%)	Potassium Feldspar (%)	Plagioclase (%)	Clay & Micas (%)	Calcite (%)	Dolomite (%)	Gypsum (%)
Top	C4-8	39.7	13.6	12.2	22.3	7.9	2.8	1.6
	C4-7	50.8	12.2	13.7	13.8	4.0	1.7	3.7
	C4-6	51.0	14.6	15.5	7.7	6.7	1.6	3.0
	C4-5	53.9	12.1	12.7	7.4	9.3	1.4	3.2
	C4-4	54.6	11.9	14.0	10.7	4.7	2.0	2.1
	C4-3	50.3	12.4	13.4	13.4	6.6	2.4	1.5
	C4-2	51.0	11.5	13.8	12.3	7.2	2.1	2.1
	C4-1	47.4	14.8	13.2	14.3	5.9	1.7	2.8
	C3-8	39.6	11.9	13.8	20.7	8.6	1.7	3.7
	C3-7	40.4	13.1	12.7	20.1	8.6	2.0	3.2
	C3-6	48.8	12.8	14.7	10.8	6.9	2.0	4.1
	C3-5	51.4	13.9	14.7	9.6	6.5	1.7	2.2
	C3-4	50.7	13.8	14.7	9.9	6.6	1.7	2.7
	C3-3	53.2	12.0	15.5	9.1	6.7	2.1	1.7
	C3-2	53.2	12.2	13.5	9.9	6.6	2.3	2.3
	C3-1	50.1	14.6	16.9	9.0	5.6	1.3	2.5
	C2-8	41.2	14.1	13.7	19.4	8.1	1.6	1.9
	C2-7	47.5	12.8	14.4	14.4	6.2	2.1	2.6
	C2-6	48.2	14.8	13.6	10.6	7.1	1.6	4.1
	C2-5	54.3	12.5	14.8	8.7	5.7	1.0	3.0
	C2-4	55.9	11.7	14.8	7.0	7.5	1.2	1.9
	C2-3	53.2	13.3	13.8	10.7	6.0	1.9	1.0
	C2-2	50.0	13.2	14.6	9.2	7.5	1.7	3.7
Base	C2-1	49.1	11.6	13.7	13.8	6.2	3.1	2.5

	Sample	Quartz (%)	Potassium Feldspar (%)	Plagioclase (%)	Clay & Micas (%)	Calcite (%)	Dolomite (%)	Gypsum (%)
Top	**M3-8**	37.7	13.1	11.6	23.4	8.8	3.8	1.6
	M3-7	46.1	13.6	14.0	12.3	9.3	1.6	3.2
	M3-6	52.4	13.0	14.1	10.6	7.1	1.4	1.4
	M3-5	54.3	11.3	14.9	10.3	5.7	1.8	1.7
	M3-4	52.4	12.7	14.2	7.4	6.4	2.0	4.9
	M3-3	52.0	13.4	13.2	9.7	6.0	1.9	3.8
	M3-2	51.6	12.5	14.9	9.0	5.7	1.7	4.5
	M3-1	47.1	13.3	13.7	14.2	7.0	2.5	2.2
	M2-8	47.9	10.0	9.7	19.8	8.3	1.5	2.8
	M2-7	45.6	12.2	11.8	20.0	6.8	2.0	1.6
	M2-6	49.1	14.9	14.6	11.1	5.6	1.0	3.8
	M2-5	52.1	11.4	15.4	8.7	7.3	1.6	3.5
	M2-4	53.5	15.9	15.9	6.2	4.0	2.1	2.4
	M2-3	50.9	15.4	12.7	11.3	6.3	1.6	1.8
	M2-2	48.7	13.1	13.2	12.1	8.3	1.5	3.1
	M2-1	43.7	12.4	13.0	19.3	7.6	1.3	2.7
	M1-8	40.0	12.6	11.7	21.4	9.4	2.5	2.3
	M1-7	43.0	13.5	11.1	20.8	7.3	2.9	1.3
	M1-6	46.4	13.3	13.0	13.2	8.5	1.6	4.1
	M1-5	52.5	15.8	16.3	7.3	3.5	2.6	2.1
	M1-4	54.8	11.4	13.1	9.8	6.8	0.9	3.4
	M1-3	53.8	12.3	12.8	10.6	5.6	2.6	2.2
	M1-2	53.2	13.3	13.4	10.2	5.9	2.3	1.7
Base	**M1-1**	50.8	11.5	13.1	13.5	6.4	2.7	1.9

	Sample	Quartz (%)	Potassium Feldspar (%)	Plagioclase (%)	Clay & Micas (%)	Calcite (%)	Dolomite (%)	Gypsum (%)
Top	T7-8	37.3	13.1	12.7	21.7	7.9	3.3	4.1
	T7-7	46.2	11.9	12.4	17.2	6.7	3.1	2.5
	T7-6	50.3	13.5	14.5	10.0	6.9	1.9	2.8
	T7-5	56.8	12.8	13.7	8.4	4.8	1.6	1.9
	T7-4	54.5	12.7	13.9	9.3	5.4	1.1	3.1
	T7-3	53.1	12.4	12.2	12.5	5.1	1.5	3.2
	T7-2	52.1	13.6	15.5	8.2	6.1	1.9	2.6
	T7-1	44.5	13.8	14.2	14.2	8.2	1.9	3.3
	T6-8	38.1	12.9	13.3	22.3	7.2	3.6	2.7
	T6-7	43.9	14.8	14.2	17.6	5.3	2.6	1.5
	T6-6	50.5	12.2	15.0	13.0	5.5	2.1	1.8
	T6-5	52.6	12.7	15.3	8.3	4.5	1.8	4.8
	T6-4	54.2	11.9	13.9	8.7	4.9	1.8	4.6
	T6-3	52.1	13.3	14.0	9.5	5.8	2.0	3.4
	T6-2	50.4	14.2	14.7	10.7	5.7	2.4	1.8
	T6-1	48.9	13.9	15.0	9.9	7.6	2.1	2.6
	T5-8	32.1	14.8	14.8	25.1	6.6	2.9	3.8
	T5-7	50.5	13.8	13.8	12.2	4.5	2.0	3.2
	T5-6	51.7	13.7	14.7	10.6	4.9	1.7	2.6
	T5-5	54.5	12.1	15.1	8.7	4.9	2.4	2.4
	T5-4	53.9	12.3	13.1	11.6	4.9	1.4	2.8
	T5-3	52.9	12.4	13.4	10.9	4.7	2.2	3.5
	T5-2	50.9	13.2	13.6	11.7	5.1	2.2	3.2
Base	T5-1	44.0	12.5	16.1	14.3	6.5	0.7	5.9

Couplet M3	Coarse bed		Fine bed	
Sample #	M3-CL	M3-CR	M3-FL	M3-FR
Quartz (%)	51.5	51.3	42.9	36.4
Potassium Feldspar (%)	11.2	12.0	12.9	11.4
Plagioclase (%)	14.2	14.0	13.6	11.4
Clay & Micas (%)	11.7	12.0	17.1	25.5
Calcite (%)	5.0	6.6	6.7	10.4
Dolomite (%)	2.4	2.0	2.5	2.9
Gypsum (%)	4.0	2.1	4.4	2.0

Couplet M2	Coarse bed		Fine bed	
Sample #	M2-CL	M2-CR	M2-FL	M2-FR
Quartz (%)	53.7	54.9	42.1	40.6
Potassium Feldspar (%)	13.2	11.7	13.7	12.4
Plagioclase (%)	14.6	12.7	12.5	12.7
Clay & Micas (%)	10.6	11.9	18.5	21.2
Calcite (%)	4.6	6.6	7.8	9.8
Dolomite (%)	1.6	1.4	2.8	2.1
Gypsum (%)	1.7	0.9	2.7	1.3

Couplet M1	Coarse bed		Fine bed	
Sample #	M1-CL	M1-CR	M1-FL	M1-FR
Quartz (%)	51.2	52.2	41.2	38.5
Potassium Feldspar (%)	12.7	12.8	12.7	13.3
Plagioclase (%)	13.9	13.1	12.9	14.3
Clay & Micas (%)	12.7	10.3	20.2	21.3
Calcite (%)	6.0	8.4	8.1	7.2
Dolomite (%)	1.9	1.6	2.9	3.6
Gypsum (%)	1.7	1.6	1.9	1.8

APPENDIX G

IMAGE ANALYSIS

Grayscale Photomosaics: Section FC6-2, Segments A-U

After photo acquisition and image correction (see main text), 21 contiguous

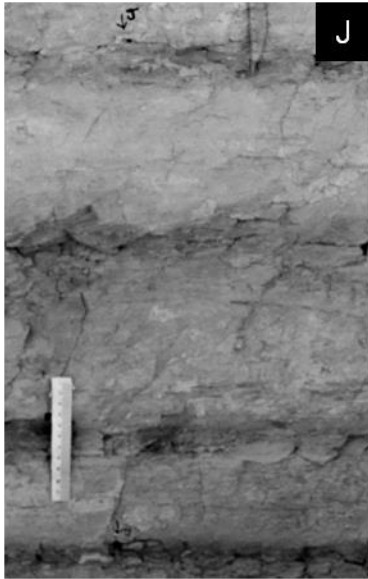segments from section FC6-2 were used for time series analysis (F G1).
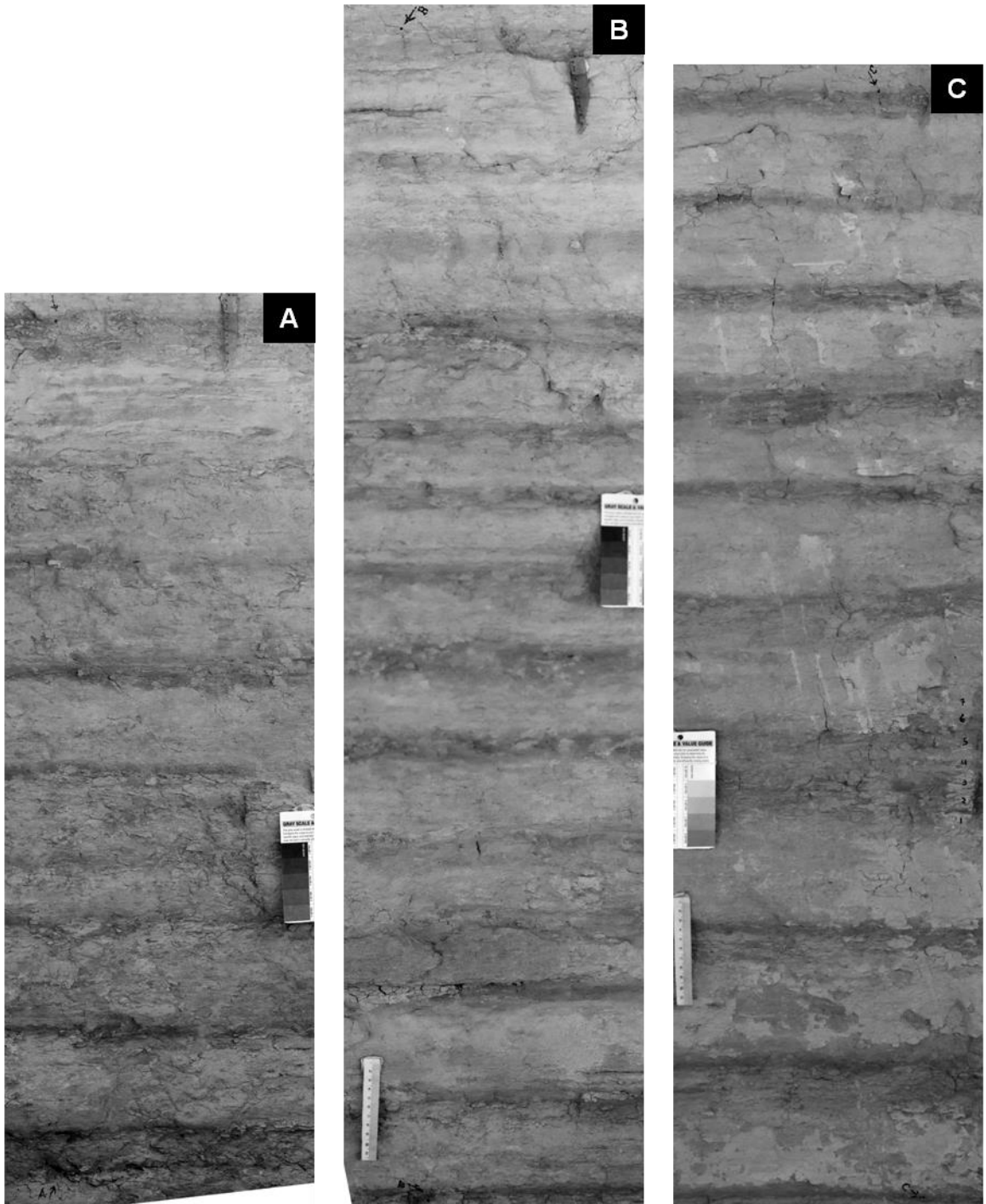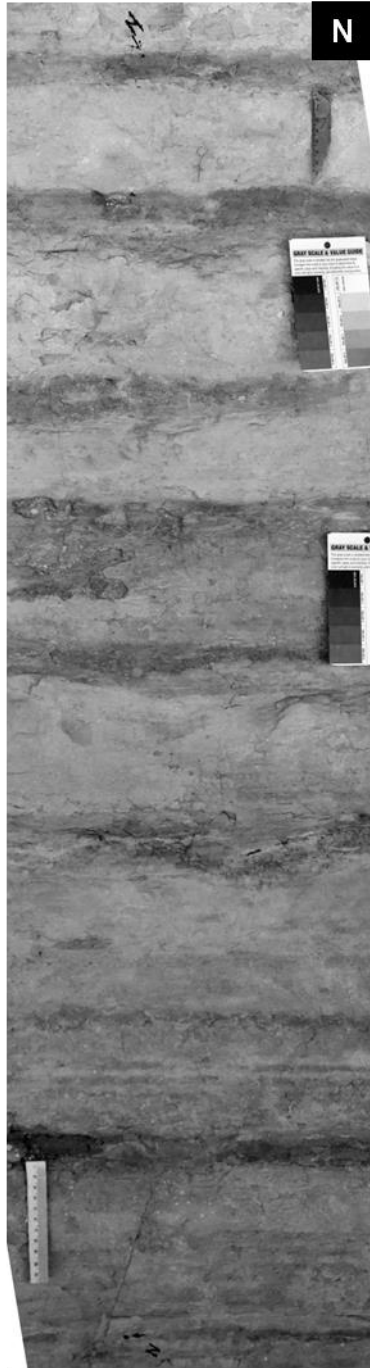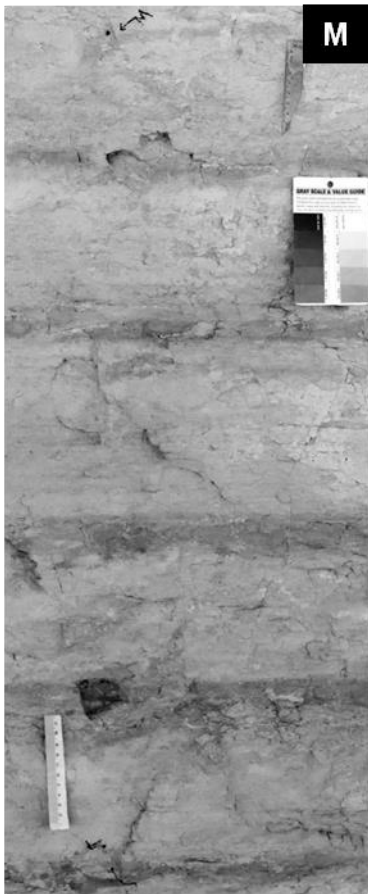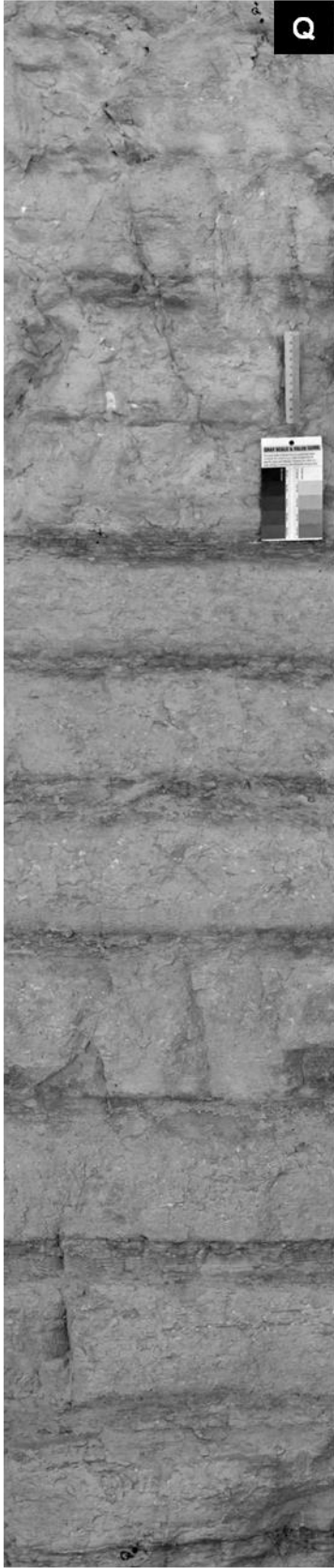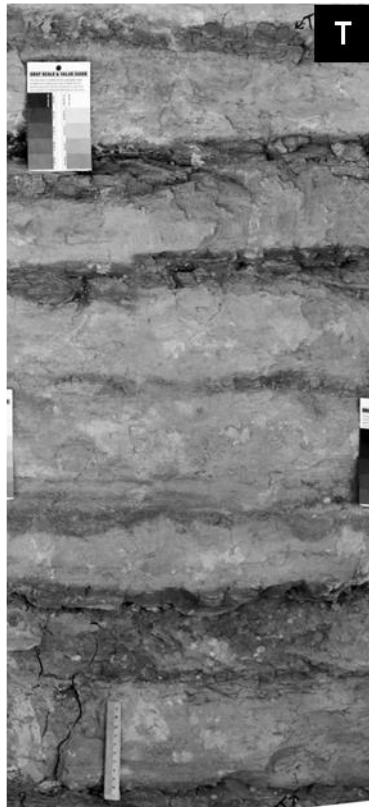
Figure G1. Photomosaics of individual contiguous segments of section FC6-2, presented in stratigraphic order from bottom (segment A) to top (segment U) of analyzed interval, after grayscale conversion.
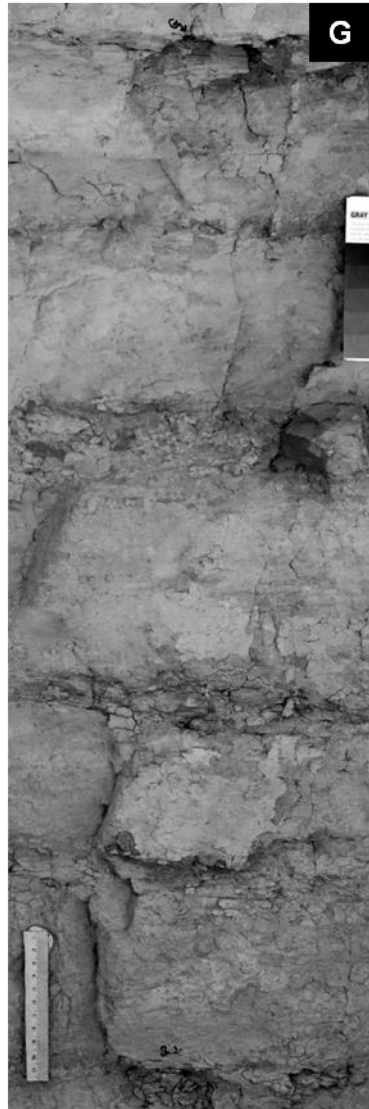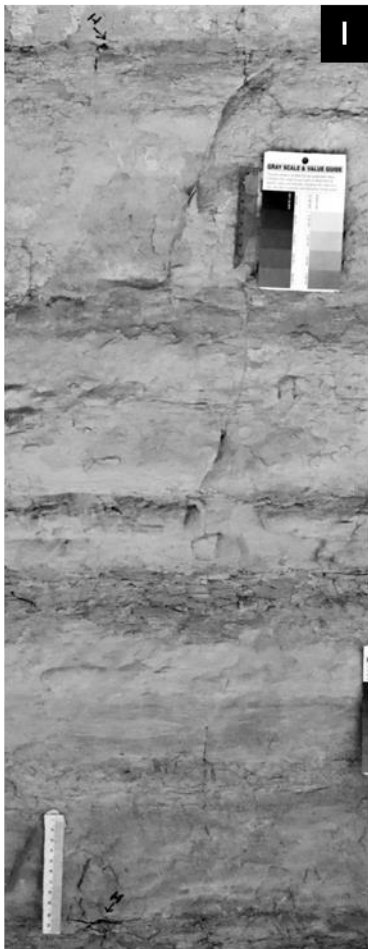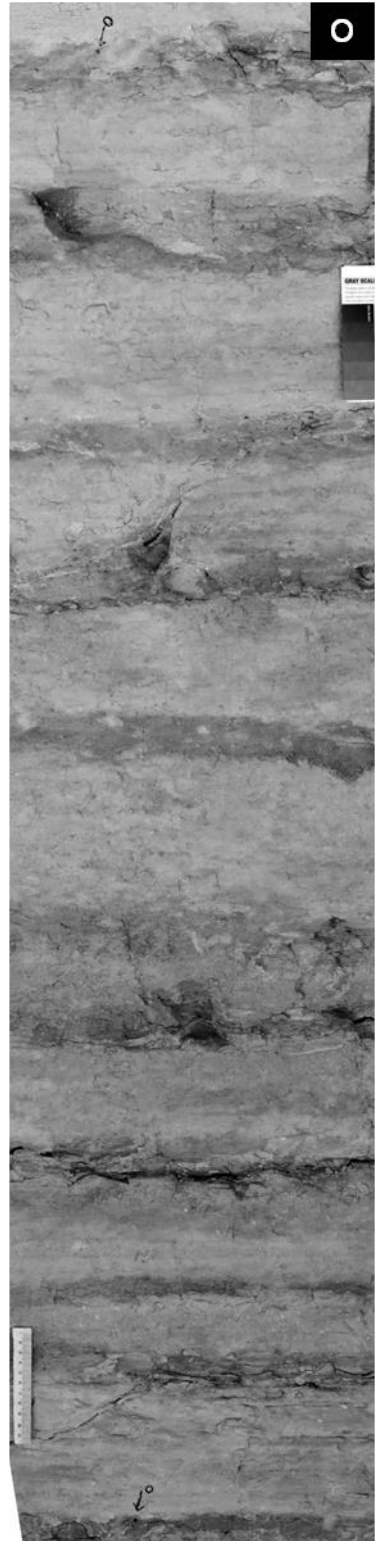
Composite Grayscale Intensity Log: Segments A-U

Image brightness (grayscale) values along parallel, linear transects normal to stratification were extracted and stacked to minimize noise (reflecting localized shading due to irregular relief and discontinuous cracks of the photographed surface) using image-analysis software (IGOR Pro, WaveMetrics, Inc.). Grayscale intensity logs for each segment were obtained by averaging pixel values over a fixed horizontal width of the image per vertical pixel increments (F G2). The composite log was obtained by juxtaposing contiguous segments (F G3), and spectral analysis techniques (fast Fourier transform and Thomson multitaper) were applied to the digitally extracted transects to ascertain if dominant spectral peaks in grayscale variation were present (Grippo et al., 2004; Larkins, 2009; Meyers et al., 2001; Thomson, 1982).
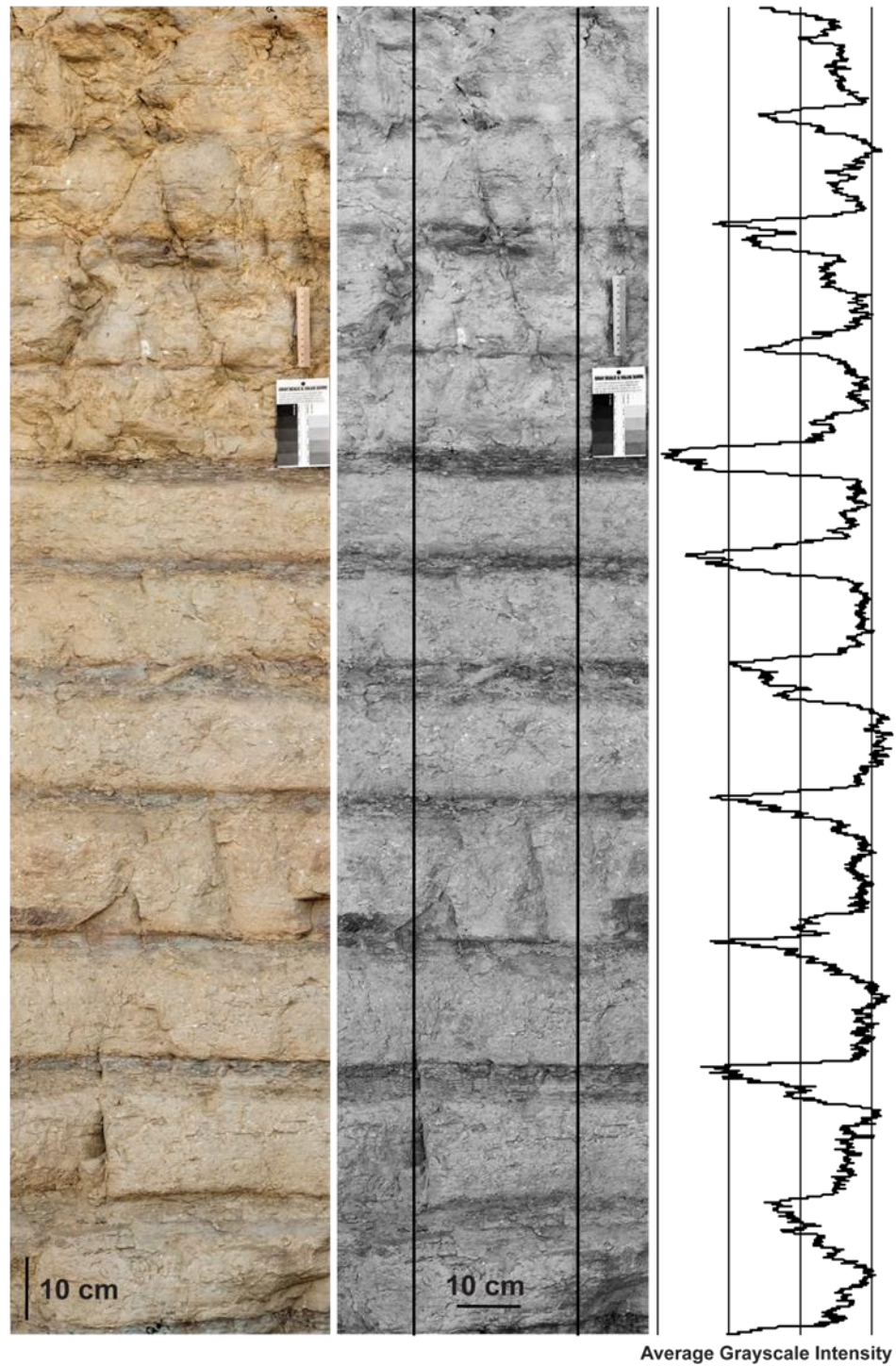
Figure G2. Procedure used to extract the grayscale variation signal from representative segment (Q). (Left) Photo acquisition of a segment; (Middle) Grayscale conversion; (Right) Log of average grayscale intensity obtained by averaging pixel values over a fixed horizontal width of the image in grayscale (rectangle in Middle) per vertical pixel increments. Photomosaics (converted to grayscale) for all segments shown in F G1; the composite grayscale intensity log, obtained by juxtaposing contiguous segments, shown in F G3.
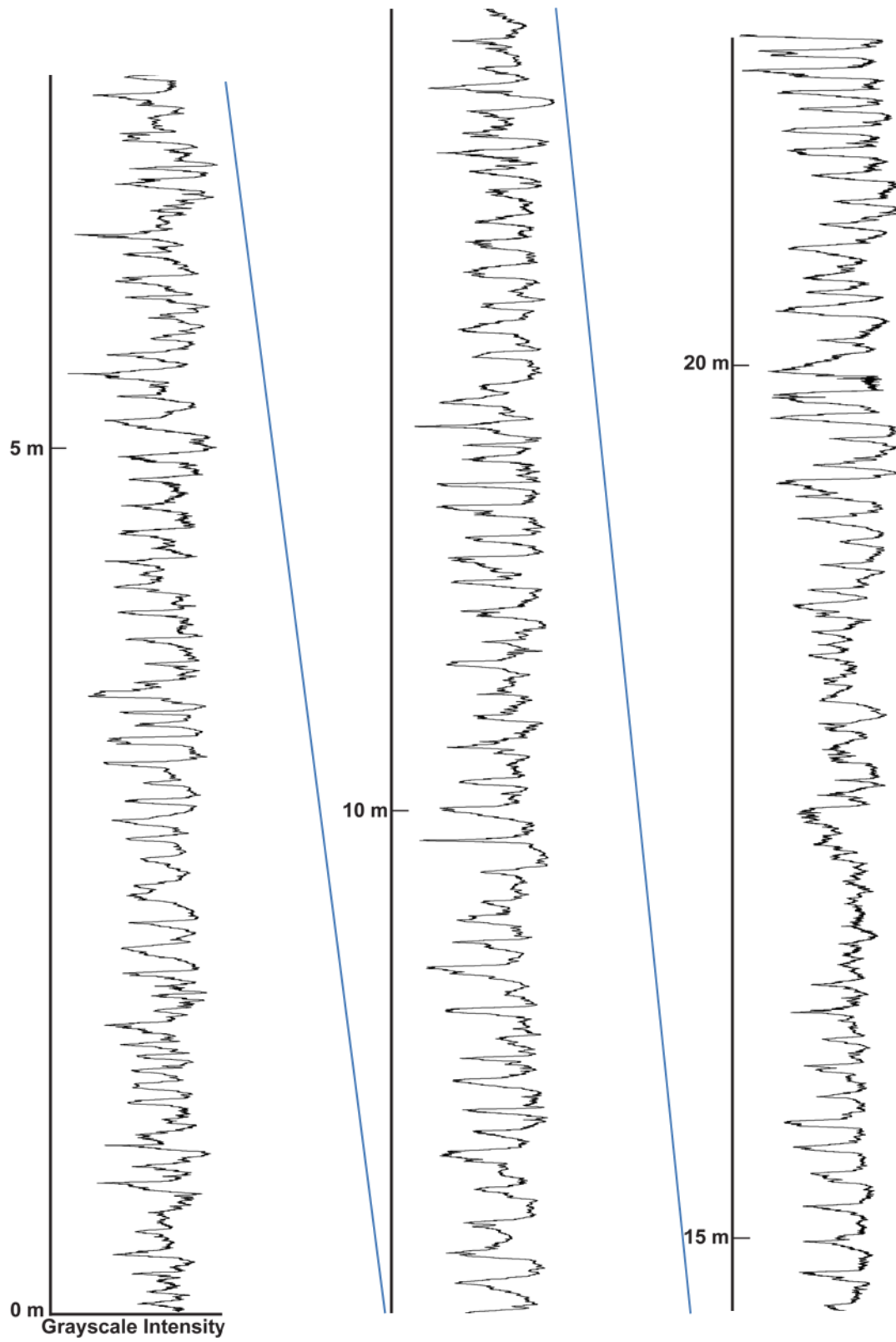
Figure G3. Composite grayscale intensity log of Segments A-U, Section FC6-2.